Reactive Transport Modelling of Diffusion in Low Permeable Media – MIN3P-THCm Simulations of EBS TF-C Compacted Bentonite Diffusion Experiments

NWMO TR-2014-23 **December 2014**

Mingliang Xie[1], Pejman Rasouli[1], K. Ulrich Mayer[1] and Kerry T. B. MacQuarrie[2]

[1]Department of Earth, Ocean and Atmospheric Sciences, University of British Columbia
[2]Department of Civil Engineering, University of New Brunswick

nwmo
NUCLEAR WASTE MANAGEMENT ORGANIZATION
SOCIÉTÉ DE GESTION DES DÉCHETS NUCLÉAIRES

Nuclear Waste Management Organization
22 St. Clair Avenue East, 6th Floor
Toronto, Ontario
M4T 2S3
Canada

Tel: 416-934-9814
Web: www.nwmo.ca

Reactive Transport Modelling of Diffusion in Low Permeable Media – MIN3P-THCm Simulations of EBS TF-C Compacted Bentonite Diffusion Experiments

NWMO TR-2014-23

December 2014

Mingliang Xie[1], Pejman Rasouli[1], K. Ulrich Mayer[1] and Kerry T. B. MacQuarrie[2]
[1]Department of Earth, Ocean and Atmospheric Sciences, University of British Columbia
[2]Department of Civil Engineering, University of New Brunswick

Document History

Title:	Reactive Transport Modelling of Diffusion in Low Permeable Media – MIN3P-THCm Simulations of EBS TF-C Compacted Bentonite Diffusion Experiments		
Report Number:	NWMO TR-2014-23		
Revision:	R000	Date:	December 2014
[1]Department of Earth, Ocean and Atmospheric Sciences, University of British Columbia [2]Department of Civil Engineering, University of New Brunswick			
Authored by:	Mingliang Xie[1], Pejman Rasouli[1]		
Verified by:	Kerry T. B. MacQuarrie[2]		
Approved by:	K. Ulrich Mayer[1]		
Nuclear Waste Management Organization			
Reviewed by:	Tammy Yang, Monique Hobbs		
Accepted by:	Mark Jensen		

ABSTRACT

Title: **Reactive Transport Modelling of Diffusion in Low Permeable Media – MIN3P-THCm Simulations of EBS TF-C Compacted Bentonite Diffusion Experiments**
Report No.: **NWMO TR-2014-23**
Author(s): Mingliang Xie[1], Pejman Rasouli[1], K. Ulrich Mayer[1] and Kerry T. B. MacQuarrie[2]
Company: [1]Department of Earth, Ocean and Atmospheric Sciences, University of British Columbia
[2]Department of Civil Engineering, University of New Brunswick
Date: December 2014

Abstract
Diffusion dominated reactive transport is an important process in engineered barrier systems for the long-term safety analysis of deep geological repositories for used nuclear fuel waste. In the framework of EBS TF-C (the Äspö Task Force on Engineered Barrier Systems – Chemistry working program), four sets of benchmarks were initiated based on systematic laboratory experiments. Benchmark I consists of a set of laboratory through-diffusion experiments to investigate the salt diffusion properties, without ion exchange, in purified homo-ionic Na- or Ca-montmorillonite. Benchmark II includes three diffusion experiments with increasing complexity by considering diffusion, kinetic mineral dissolution and ion exchange. Benchmark III includes a set of Na/Ca and Ca/Na ion exchange experiments using compacted (initially) homo-ionic Na- and Ca-montmorillonite at different dry densities. Benchmark IV is based on the flow-through experiment on a bentonite core obtained from an in-situ experiment. To simulate the benchmarks, a semi-empirical multicomponent diffusion (MCD) model has been implemented in the reactive transport code MIN3P-THCm, which enables the code to simulate the diffusion of a mixture of ions through porous media by taking the species-dependent diffusion coefficients and electrostatic interactions in the solution into consideration.

MIN3P-THCm including the MCD model together with the parameter estimation software PEST provides a method for the estimation of both porosity and tortuosity parameters from diffusion experiments. Numerical analyses of the through-diffusion experiments in compacted Na- and Ca-montmorillonite (Benchmark I) showed very good agreement to the experimental results. The simulations also reveal that with an increase of ionic strength of the solution, the diffusion parameters (i.e., the effective diffusion coefficient D_e, the effective porosity ϕ_e, and the effective tortuosity τ_e) generally increase as well. Numerical simulation results of the Benchmark II case also agree well with the experimental results. Model calibration showed that simulation results are sensitive to variations in the thickness of the top and bottom bentonite sample layers. Simulations of the Benchmark III cases generally overestimated Ca^{2+} concentrations in comparison to experimental data while simulated Na^+ concentration show good agreement to the observations. This result can be explained either by uncertainties associated with the experimental data as a result of inaccuracies in the ion concentrations which were measured indirectly, or alternatively, the ion exchange mechanism may be different than simulated (e.g. ion exchange of complexed species such as $CaCl^+$ (Sposito et al. 1983)). Simulated results obtained with MIN3P-THCm for the most complex Benchmark IV cases show very good agreement to results obtained with the reactive transport code CrunchFlow. The simulation results for the three scenarios that were simulated with MIN3p-THCm showed that experimental data are better reproduced when more geochemical processes are considered, indicating that the key to successful simulation lies in correctly identifying the controlling processes.

TABLE OF CONTENTS

Page

ABSTRACT iii

1. INTRODUCTION 1

2. OBJECTIVES AND SCOPE 1

3. MODEL FORMULATION AND DEVELOPMENT 2

3.1 GOVERNING EQUATIONS FOR REACTIVE TRANSPORT AND MCD MODEL DEVELOPMENT 2
3.1.1 Multicomponent Diffusion 2
3.1.2 Nernst-Planck Equation for Multicomponent Systems 2
3.1.3 Electroneutrality of the Solution 2
3.1.4 Implementation 4
3.2 PARAMETER ESTIMATION METHOD 4

4. OVERVIEW OF EBS TF-C BENCHMARKS 4

5. BENCHMARK I: THROUGH-DIFFUSION 5

5.1 DESCRIPTION OF EXPERIMENT 5
5.2 MODEL SETUP AND MATERIAL PROPERTIES 7
5.3 RESULTS FOR EXPERIMENTS USING NA-MONTMORILLONITE 8
5.3.1 B1.1a: 0.1 mol L^{-1} NaCl Source Solution 8
5.3.2 B1.1b: 0.4 mol L^{-1} NaCl Source Solution 10
5.3.3 B1.1c: 1.0 mol L^{-1} NaCl Source Solution 12
5.4 RESULTS FOR EXPERIMENTS USING CA-MONTMORILLONITE 13
5.4.1 B1.2a: 0.025 mol L^{-1} $CaCl_2$ Source Solution 13
5.4.2 B1.2b: 0.1 mol L^{-1} $CaCl_2$ Source Solution 14
5.4.3 B1.2c: 0.4 mol L^{-1} $CaCl_2$ Source Solution 16
5.5 SUMMARY AND DISCUSSION 17

6. BENCHMARK II: MINERAL DISSOLUTION AND DIFFUSION 20

6.1 CASE B2.1: THROUGH-DIFFUSION OF $CASO_4$ IN CA-MONTMORILLONITE 21
6.1.1 Description of Experiment 21
6.1.2 Model Setup and Material Properties 21
6.1.3 Simulation Results 22
6.2 CASE B2.2A: GYPSUM DISSOLUTION AND DIFFUSION IN CA-MONTMORILLONITE 23
6.2.1 Description of Experiment 23
6.2.2 Model Setup and Material Properties 23
6.2.3 Simulation Results 25
6.2.3.1 Diffusion parameter estimation 25
6.2.3.2 Simulation of the experiment 27
6.3 CASE B2.2B: GYPSUM DISSOLUTION, DIFFUSION AND ION EXCHANGE IN NA-MONTMORILLONITE 28
6.3.1 Description of Experiment 28

6.3.2 Model Setup and Material Properties 29
6.3.3 Simulation Results 29
6.4 SUMMARY AND DISCUSSION 32

7. BENCHMARK III: ION EXCHANGE 33

7.1 DESCRIPTION OF EXPERIMENT 33
7.2 ANALYSIS OF EXPERIMENTAL DATA 36
7.3 MODEL SETUP AND MONTMORILLONITE MATERIAL PROPERTIES 40
7.4 SIMULATION RESULTS FOR EXPERIMENTS ON NA-MONTMORILLONITE 41
7.4.1 Case B3.1 41
7.4.2 Case B3.2 43
7.4.3 Case B3.3 45
7.5 SIMULATION RESULTS FOR EXPERIMENTS ON CA-MONTMORILLONITE 47
7.5.1 Case B3.4 47
7.5.2 Case B3.5 49
7.5.3 Case B3.6 51
7.6 DISCUSSION 52

8. BENCHMARK IV: REACTIVE TRANSPORT IN BENTONITE 53

8.1 DESCRIPTION OF EXPERIMENT 54
8.2 MODEL SETUP AND MATERIAL PROPERTIES 54
8.3 BENCHMARK SCENARIOS 57
8.4 SIMULATION RESULTS 58

9. CONCLUSIONS AND OUTLOOK 64

ACKNOWLEDGEMENTS 65

REFERENCES 66

LIST OF TABLES

Page

Table 1: Source Solution Concentrations Used for the Na-montmorillonite and Ca-montmorillonite Through-Diffusion Experiments 6
Table 2: Dimensions and Physical Parameters of the Test Samples for Benchmark I (Birgersson et al. 2009) 8
Table 3: Free Aqueous Diffusion Coefficients (D_0) of Relevant Species (Lide 1994) 8
Table 4: Experimental and Simulated Results for Accumulated NaCl Mass in the Target Reservoir for Case B1.1a 9
Table 5: Experimental and Simulated Results for Accumulated NaCl Mass for Case B1.1b 11
Table 6: Experimental and Simulated Results for the Accumulated NaCl Mass for Case B1.1c 13
Table 7: Experimental and Simulated Results of the Accumulated $CaCl_2$ Mass for Case B1.2a 14
Table 8: Experimental and Simulated Results of Accumulated $CaCl_2$ Mass for Case B1.2b 15
Table 9: Experimental and Simulated Results of the Accumulated $CaCl_2$ for Case B1.2c 17
Table 10: Summary of Estimated/Simulated Diffusion Parameters Based on the Through-Diffusion Experiments Using Na-Montmorillonite 17
Table 11: Summary of Estimated/Simulated Diffusion Parameters Based on the Through-Diffusion Experiments Using Ca-montmorillonite 18
Table 12: Summary of Estimated/Simulated Diffusion Parameters for the Experiments Using Na-montmorillonite (Birgersson, Unpublished Data) Based on the Donnan Equilibrium Approach (Birgersson 2009) 18
Table 13: Summary of Estimated/Simulated Diffusion Parameters for the Experiments Using Ca-montmorillonite (Birgersson, Unpublished Data) Based on the Donnan Equilibrium Approach (Birgersson 2009) 19
Table 14: Summary of Estimated/Simulated Diffusion Parameters for Benchmark I Experiments Using Na-Montmorillonite Based on the Analytical Approach by Holton (2013) 19
Table 15: Summary of Estimated/Simulated Diffusion Parameters for Benchmark I Experiments Using Ca-Montmorillonite Based on the Analytical Approach by Holton (2013) 20
Table 16: Benchmark II Mineral Dissolution and Migration Experiments 21
Table 17: Dimensions and Soil Properties of Test Samples for Benchmark II (Birgersson et al. 2009; Birgersson 2011) 21
Table 18: Experimental Data and Simulated Results for the Accumulated Ca^{2+} Mass in the Target Reservoir for Case B2.1 23
Table 19: Experimental Data and Simulated Results for the Average of the Accumulated Ca^{2+} Mass in the Top and Bottom Reservoirs for Case B2.2a 26
Table 20: Experimental Data and Simulated Results for the Accumulated $CaSO_4$ and Na_2SO_4 Mass in [mol] for Case B2.2b 30
Table 21: Summary of Calibrated Diffusion Parameters for Benchmark II 32
Table 22: Experimental Cases, Montmorillonite Sample Properties and the Design Amount of Added Cations in the Reservoir (Based on Birgersson 2011) 34
Table 23: Mass Balance Calculations for Modified Composition: Mass Balance Calculations for Na^+ for Experiments with Na-montmorillonite (Birgersson 2011) 37

Table 24: Mass Balance Calculations for Ca^{2+} for Experiments with Na-montmorillonite after Modifications Based on Suggestions by the Research Team in Charge of the Experimental Work 38
Table 25: Mass Balance Calculations for Na^{+} for Experiments on Ca-montmorillonite 39
Table 26: Mass Balance Calculations for Ca^{2+} for Experiments with Ca-montmorillonite 39
Table 27: Measured Selectivity Coefficients (Kc) for Ca/Na According to the Gaines-Thomas Convention (Karnland et al. 2011) 41
Table 28: Estimated Diffusion Parameters in Na-Montmorillonite for Case B3.1 42
Table 29: Estimated Diffusion Parameters in Na-Montmorillonite for Case B3.2 45
Table 30: Estimated Diffusion Parameters in Na-Montmorillonite for Case B3.3 47
Table 31: Estimated Diffusion Parameters in Ca-Montmorillonite for Case B3.4 (Benchmark III) 49
Table 32: Estimated Diffusion Parameters in Ca-Montmorillonite for Case B3.5 (Benchmark III) 50
Table 33: Estimated Diffusion Parameters in Ca-Montmorillonite for Benchmark III Case B3.6 52
Table 34: Components (i.e., Primary Species), Secondary Species, Gases and Minerals Used in the Benchmark IV Simulations 55
Table 35: Composition of the Infiltrating Fluid (Left-Hand Reactive Transport Boundary Condition) and the Initial Porewater Conditions (Fernández et al. 2011) 56
Table 36: Mineralogy and Kinetic Parameters Based on Alt-Epping et al. (2014) 56
Table 37: Selectivity Coefficients for Ion Exchange Reactions (from Bradbury and Baeyens 2003) 57

LIST OF FIGURES

Page

Figure 1: Schematic Diagram of the Through-Diffusion Experimental Setup (from Birgersson et al. 2009) 6
Figure 2: Depiction of the One-Dimensional Model for the B1.1a Through-Diffusion Experiment (Left), and the Experimental Results Obtained for the Accumulated NaCl Mass and the Swelling Pressure (Right) 7
Figure 3: Comparison of MIN3P-THCm Results (Lines) and Experimental Data (Symbols) for Accumulated NaCl Mass in the Target Reservoir for Case B1.1a 10
Figure 4: Comparison of MIN3P-THCm Results (Line) and Experimental Data (Symbols) for Accumulated NaCl Mass in the Target Reservoir for Case B1.1b 11
Figure 5: Comparison of MIN3P-THCm Results (Line) and Experimental Data (Symbols) for Accumulated NaCl Mass in the Target Reservoir for Case B1.1c 12
Figure 6: Comparison of Simulated MIN3P-THCm Result (Line) and Experimental Data (Symbols) for Accumulated $CaCl_2$ Mass in the Target Reservoir for Case B1.2a 14
Figure 7: Comparison of MIN3P-THCm Result (Line) and Experimental Data (Symbols) for Accumulated $CaCl_2$ Mass in the Target Reservoir for Case B1.2b 15
Figure 8: Comparison of MIN3P-THCm Result (Line) and Experimental Data (Symbols) for Accumulated $CaCl_2$ Mass in the Target Reservoir for Case B1.2c 16
Figure 9: Concept for Benchmark II Simulations: Gypsum Dissolution and $CaSO_4$ Diffusion 20
Figure 10: Comparison of Simulated Results and Experimental Data for Accumulated Ca^{2+} Mass in the Target Reservoir for Case B2.1 22
Figure 11: Comparison of Simulated and Experimental Average of the Accumulated $CaSO_4$ Mass in the Top and Bottom Reservoirs, Blue Line With Symbols – Experimental

Data, Red Line – Simulated Results Using The Calibrated Effective Porosity and Tortuosity from B2.1, Black Dashed Line – Simulated Results using MIN3P-THCm and Parameter Optimization using PEST, Symbols Depict Actual Experimental Data in Top and Bottom Reservoirs 25
Figure 12: Comparison of Experimental and Simulated Accumulated Ca^{2+} Mass in the Top (Red) and Bottom (Blue) Reservoirs for Case B2.2a (in the Legend, d Refers to the Thickness of the Montmorillonite Layer). To Reproduce the Different Rates of Mass Accumulation in the Top and Bottom Reservoirs during the Experiments, It Was Assumed that the Two Montmorillonite Layers Have Different Thicknesses . 28
Figure 13: Comparison of Simulated and Experimental Accumulated Na_2SO_4 Mass (Left) and $CaSO_4$ Mass (Right) in the Top and Bottom Reservoirs 31
Figure 14: Numerical Simulation Results at 40.6 Days: Left – Profiles of Aqueous Ca^{2+} (Red) and Na^+ (Blue) Concentration and Gypsum Volume Fraction (Black); Right – Equivalent Fractions of Ion-exchanged Species Reported as Percentages 31
Figure 15: Schematic Design of the Experimental Setup for Benchmark III (Birgersson et al. 2009) 34
Figure 16: Experimental Concentrations of Ca^{2+} and Na^+ in the Reservoir Calculated from Solution Potentials Measured by Ion Selective Electrodes for Benchmark III Case B3.1, Case B3.2, Case B3.3 and the Reference Solution (Based on Birgersson et al. 2009 and Birgersson 2011 with Modifications Described in Table 24) (the vertical Red Dashed Lines Depict the Time When the Experimental Phases Change)..... 35
Figure 17: Experimental Concentrations of Ca^{2+} and Na^+ in the Reservoir Calculated from Solution Potentials Measured by Ion Selective Electrodes for Benchmark III Case B3.4, Case B3.5, Case B3.6 and the Reference Solution (Based on Birgersson et al. 2009 and Birgersson 2011 with Modifications Described in Table 24) (the vertical Red Dashed Lines Depict the Time When the Experiment Phase Changes)..... 36
Figure 18: Model Setup for the Ion Exchange Experiments 40
Figure 19: Simulated Concentrations of Sorbed Na-X (Red Lines) and Ca-X_2 (Blue Lines) at the Beginning (Dashed Lines) and the End (Solid Lines) of Phase I (Left) and Phase III (Right) for Benchmark III Case B3.1 41
Figure 20: Comparison of Simulated and Experimental Concentrations for Ca^{2+} (Left) and Na^+ (Right) in the Reservoir Solution for Benchmark III Experiment B3.1..... 42
Figure 21: Simulated Concentrations of Sorbed Na-X (red lines) and Ca-X_2 (blue lines) at the Beginning (Dashed Lines) and the End (Solid Lines) of Phase I (left) and Phase III (Right) (Benchmark III Case 3.2) 44
Figure 22: Comparison of Simulated and Experimental Concentrations for Ca^{2+} (Left) and Na^+ (Right) in the Reservoir Solution for Benchmark III Experiment B3.2..... 45
Figure 23: Comparison of Simulated and Experimental Concentrations for Ca^{2+} (Left) and Na^+ (Right) in the Reservoir Solution for Experiment B3.3 (Benchmark III) 46
Figure 24: Simulated Concentrations of Sorbed Na-X (Red Lines) and Ca-X_2 (Blue Lines) at the Beginning (Dashed Lines) and the End (Solid Lines) of Phase I (Left) and Phase II (Right) (Benchmark III Case B3.3)..... 46
Figure 25: Simulated Concentrations of Sorbed Na-X (Red Lines) and Ca-X_2 (Blue Lines) at the Beginning (Dashed Lines) and the End (Solid Lines) of Phase I (Left) and Phase III (Right) (Benchmark III Case B3.4)..... 48
Figure 26: Comparison of Simulated and Experimental Concentrations for Ca^{2+} (Left) and Na^+ (Right) in the Reservoir Solution for Experiment B3.4 (Benchmark III) 48

Figure 27: Simulated Concentrations of Sorbed Na-X (Red Lines) and Ca-X_2 (Blue Lines) at the Beginning (Dashed Lines) and the End (Solid Lines) of Phase I (left) and Phase III (Right) (Benchmark III Case B3.5) 50
Figure 28: Comparison of Simulated and Experimental Concentrations for Ca^{2+} (Left) and Na^{+} (Right) in the Reservoir Solution for Benchmark III Experiment B3.5 50
Figure 29: Simulated Concentrations of Sorbed Na-X (Red Lines) and Ca-X_2 (Blue Lines) at the Beginning (Dashed Lines) and the End (Solid Lines) of Phase I (Left) and Phase III (Right) (Benchmark III Case B3.6) 51
Figure 30: Comparison of Simulated and Experimental Concentrations for Ca^{2+} (Left) and Na^{+} (Right) in the Reservoir Solution for Benchmark III Experiment B3.6 52
Figure 31: Comparison of Simulated and Experimental Concentrations for Ca^{2+} (Left) and Na^{+} (Right) in the Reservoir Solution for Benchmark III Experiment B3.1 Phase I (Including Filters) 53
Figure 32: 1D Conceptual Model Setup for Multicomponent Reactive Transport Experiment in Bentonite 54
Figure 33: Scenario 1a: Time Series of the Simulated Effluent Composition and Measured Concentrations – Including Transport Only, Single Diffusion Coefficient (min3p Stands for MIN3P-THCm, CF Stands for CrunchFlow) 58
Figure 34: Scenario 1b: Time Series of the Simulated Effluent Concentrations and Measured Concentrations– Including Transport Only, Species-Dependent Diffusion Coefficients (min3p Stands for MIN3P-THCm, CF Stands for CrunchFlow) 59
Figure 35: Scenario 2a: Time Series of the Simulated Effluent Composition and Measured Concentrations – Including Transport and Mineral Reactions, Single Diffusion Coefficient (min3p Stands for MIN3P-THCm, CF Stands for CrunchFlow) 60
Figure 36: Scenario 2b: Time Series of the Simulated Effluent Composition and Measured Concentrations – Including Transport and Mineral Reactions, Species-Dependent Diffusion Coefficients (min3p Stands for MIN3P-THCm, CF Stands for CrunchFlow) 60
Figure 37: Scenario 3a: Time Series of the Simulated Effluent Composition and Measured Concentrations – Including Transport, Mineral Reactions and Ion Exchange, Single Diffusion Coefficient (min3p Stands for MIN3P-THCm, CF Stands for CrunchFlow) 61
Figure 38: Scenario 3b: Time Series of the Simulated Effluent Composition and Measured Concentrations – Including Transport, Mineral Reactions and Ion Exchange, Species-Dependent Diffusion Coefficient (min3p Stands for MIN3P-THCm, CF Stands for CrunchFlow) 61
Figure 39: Effluent Composition Percent Differences between Simulation Option a (Single Diffusion Coefficient) and b (Species-dependent Diffusion Coefficients) for Scenarios 1, 2 and 3 Modelled by MIN3P-THCm 63

1. INTRODUCTION

Reactive transport modelling is one approach for assessing long-term geochemical stability in geological formations and engineered barrier systems relevant to deep geologic repositories (DGR) for used nuclear fuel. For example, the reactive transport code MIN3P has previously been used to evaluate redox stability in crystalline rocks of the Canadian Shield (Spiessl et al. 2008) and to simulate flow and reactive transport in a hypothetical sedimentary basin subjected to a glaciation/deglaciation cycle (Bea et al. 2011).

Recent work with MIN3P-THCm, an enhanced version of MIN3P, has included participation in the Äspö Task Force on Engineered Barrier Systems - Chemistry (EBS TF-C) working program, providing an opportunity to compare MIN3P-THCm simulation results with data from laboratory diffusion experiments and the simulation results obtained by other international modelling groups. This report summarizes the simulation of laboratory experiments conducted using water-saturated compacted montmorillonite samples.

2. OBJECTIVES AND SCOPE

The current work focuses on the numerical simulation of reactive transport in diffusion dominated porous media, with three main objectives:

1) Enhancement and verification of the MIN3P-THCm code for application to reactive transport simulations in low permeability, diffusion-dominated, clayey material such as bentonite (e.g. multicomponent diffusion, anion exclusion, surface/interlayer diffusion);
2) Application of the enhanced model to the compacted montmorillonite diffusion experiments conducted within the framework of the Äspö Task Force on Engineered Barriers - Chemistry (EBS TF-C) working program; and
3) Comparison of results obtained using MIN3P-THCm with results from other reactive transport codes, where available.

To address the first objective, several MIN3P-THCm code enhancements have been made, including:

- Addition of a multicomponent diffusion (MCD) model to account for species-dependent diffusion coefficients and electrochemical migration;
- Transport parameter estimation using PEST (Doherty 2010) in combination with MIN3P-THCm; and
- Multisite ion exchange (MIE) model.

The existing capabilities of MIN3P-THCm were verified and re-tested after each of the code modifications. In addition, the new capabilities (i.e., MCD and MIE) of MIN3P-THCm were verified and tested in relation to similar models cited in the literature.

3. MODEL FORMULATION AND DEVELOPMENT

3.1 GOVERNING EQUATIONS FOR REACTIVE TRANSPORT AND MCD MODEL DEVELOPMENT

3.1.1 Multicomponent Diffusion

Species-dependent diffusion is necessary to describe the behaviour of a system in which diffusive transport is the dominant mass transport process. Ions have different charges and mobilities, and if only concentration gradients are considered when simulating transport, a charge imbalance will develop in the electrolyte, which is not physically possible. Therefore, additional transport phenomena are required to avoid charge imbalances. The electrical field that drives electromigration counteracts the charge imbalance. As a result, multicomponent diffusion is controlled by gradients of chemical and electrical potentials. To adequately describe multicomponent transport in diffusion-dominated systems, a formulation is required that includes species-dependent diffusion coefficients and an electrochemical migration term (Appelo and Wersin 2007; Appelo et al. 2010). The Nernst-Planck equation describes those systems (Lasaga 1979, 1998; McDuff and Ellis 1979; Benyaakov 1981; Van Cappellen and Gaillard 1996).

The most important feature that distinguishes electrolyte systems from non-electrolyte systems is the electric coupling of the ionic fluxes (Helfferich 1962; Newman 1973). In electrolyte systems, the electric interaction of ion-ion, ion-solvent and ion-interfaces induces an electric field. The treatment of electrolytic diffusion follows naturally from the generalized treatment of diffusion (Taylor and Krishna 1993).

3.1.2 Nernst-Planck Equation for Multicomponent Systems

The movement of interacting species is described by the extended Nernst-Planck equation; the flux of an arbitrary species *j* is (Newman 1973):

$$\mathbf{J}_j = -\tau_e \phi_e \left[D_{0j} \left(\nabla C_j + \frac{C_j F}{RT} z_j \nabla \psi \right) \right] \qquad \textbf{(3-1)}$$

where D_{0j} is the free diffusion coefficient [$m^2\ s^{-1}$], C_j is the concentration [mol L^{-1} H_2O], F is the Faraday constant [96485 C mol^{-1}], R is the gas constant [8.341 J K^{-1} mol^{-1}], ϕ_e is the effective porosity [-], τ_e is the effective tortuosity [-], T is the absolute temperature [K], z_j is the charge number [-], and ψ is the electric potential [V or J C^{-1}]. Equation (3-1) holds in ideal systems, for all mobile species. It describes the movement of ions in a solution with or without electrodes (Helfferich 1962; Bard and Faulkner 1980; Bagotsky 2006). In a multicomponent system, the set of Nernst-Planck equations, one for each species, must be solved under the appropriate conditions.

3.1.3 Electroneutrality of the Solution

Electroneutrality of the bulk solution is an essential condition when the system is in electrical steady state. In a linear mass flow system, $\mathbf{J}_j$ (mol s^{-1} m^{-2}) is equal to $\mathbf{i}/z_jF$. Assuming there is no externally induced current (**i)** (null current assumption), the flux for component j can be written as follows:

$$\mathbf{J}_j = -\left[\begin{array}{l} \tau_e \phi_e (D^c_{0,j} \nabla C^c_j + \sum_i^{N_x} D^x_{0,i} \nu^x_{ij} \nabla C^x_i) - \\ \qquad T^{\varepsilon}_j \dfrac{\sum_l^{N_c} z_l (\tau_e \phi_e D^c_{0,k} \nabla C^c_l + \sum_i^{N_x} \nu^x_{li} \tau_e \phi_e D^x_{0,i} \nabla C^x_i)}{\sum_k^{N_c} z_k T^{\varepsilon}_k} \end{array} \right] \qquad \textbf{(3-2)}$$

The general mass continuity equation in fully saturated porous media can be written as:

$$\frac{\partial(\phi_e T^a_j)}{\partial t} + \frac{\partial T^s_j}{\partial t} + \mathbf{J}_j = Q^{a,a}_j + Q^{a,m}_j + Q^{a,ext}_j \qquad j = 1, N_c \qquad \textbf{(3-3)}$$

where:

T^a_j total aqueous component concentration of the j^{th} component in [M L^{-3} H_2O]

$$T^a_j = C^c_j + \sum_{i=1}^{N_x} \nu^x_{ij} C^x_i$$

T^s_j total concentration [M L^{-3} porous medium] of the j^{th} aqueous component on the exchanger;

J_j total flux of the j^{th} component [M L^{-3} T^{-1}];

$Q^{a,a}_j$ internal source and sink terms from intra-aqueous kinetic reactions [M L^{-3} T^{-1}];

$Q^{a,m}_j$ source-sink term due to mineral dissolution/precipitation reactions [M L^{-3} T^{-1}];

$Q^{a,ext}_j$ external source and sink term [M L^{-3} T^{-1}];

C^c_j concentrations of the components as species in solution [M L^{-3} H_2O];

C^x_i concentrations of complexed species in solution [M L^{-3} H_2O];

ν^x_{ij} stoichiometric coefficients of the j^{th} component in the complexed species;

$D^c_{0,j}$ free diffusion coefficient of the j^{th} component as species in solution [L^2 T^{-1}];

$D^x_{0,i}$ free diffusion coefficient of the i^{th} complexed species in solution [L^2 T^{-1}];

N_c the number of aqueous components; and

N_x the number of aqueous complexes.

The variable T^{ε}_j Equation (3-2) is defined as (Giambalvo et al. 2002):

$$T^{\varepsilon}_j = \tau_e \phi_e D^c_{0,j} z_j C^c_j + \sum_{i=1}^{N_x} \tau_e \phi_e D^x_{0,i} \nu^x_{ij} C^x_i$$

3.1.4 Implementation

The governing equations are implemented using a finite volume technique for spatial discretization and implicit time weighting for the temporal discretization. The reactive transport equations are solved using the global implicit approach, employing Newton's method for linearization (Mayer 1999; Mayer et al. 2002; Mayer 2010; Mayer and MacQuarrie 2010). The verification for multicomponent diffusion was conducted by making comparisons with the results from the CrunchFlow code (Steefel 2008), as described in Benchmark IV (Section 8).

3.2 PARAMETER ESTIMATION METHOD

The parameters determining the diffusive flux in porous media are porosity ϕ_e and tortuosity τ_e. As shown above, ϕ_e appears in the storage term that controls the rate of change of mass storage (equation 3.3), while both parameters (i.e., ϕ_e and τ_e) influence the diffusive mass flux (equation 3.2). Therefore, two parameters have to be determined by fitting the model to the results from diffusion experiments (e.g. through-diffusion experiments). The efficient determination of these parameters can be carried out using a parameter estimation tool such as PEST (Parameter ESTimation; Doherty 2010). PEST is an internationally recognized, software package for model-independent non-linear parameter estimation and predictive uncertainty analysis (Doherty 2010). In the current project, PEST is combined with MIN3P-THCm to automatically estimate ϕ_e and τ_e for the EBS TF-C experiments. PEST is linked to MIN3P-THCm in such a way that it successively runs MIN3P-THCm simulations until the differences between the simulation results and the experimental results are minimized (in a least squares sense). PEST uses a quasi-Newton method (namely, the Levenberg-Marquardt procedure) to determine the parameter adjustment direction to estimate a new set of parameters ϕ_e and τ_e by comparing model results after each MIN3P-THCm calculation to a set of observations. A new MIN3P-THCm calculation is then initiated. This process is repeated as many times as necessary until the discrepancy between the observed and simulated result is minimized within a specified tolerance.

4. OVERVIEW OF EBS TF-C BENCHMARKS

There are four benchmarks defined within the framework of the EBS TF-C project. All benchmarks are based on laboratory diffusion experiments on compacted bentonite or purified montmorillonite undertaken by Clay Technology AB (Sweden) or the University of Bern (Switzerland) (Birgersson 2011), including:

- Benchmark I – Through-diffusion in compacted montmorillonite (Clay Technology AB)
- Benchmark II – Mineral dissolution and migration through compacted montmorillonite (Clay Technology AB)
- Benchmark III – Ion exchange in compacted montmorillonite (Clay Technology AB)
- Benchmark IV – Reactive transport in compacted bentonite (University of Bern)

It is important to note that the ionic concentrations for Benchmark I – III experiments were calculated based on indirect measurements. The measured parameters include the electrical conductivity (σ), which is relevant for Benchmark I and II; and the voltage of an ion selectivity electrode (U), which was used for Benchmark II and III. The calibration of the relationships between ionic concentrations of each component to the measured electrical conductivity or the

voltage of an ion selectivity electrode (ISE) was undertaken using reference solutions. These reference solutions included ion(s) to be tested for given initial concentrations and were modified over a range of concentrations by adding specified amounts of salts (e.g. NaCl, $CaCl_2$). Concentration ranges were set to match the same concentration levels as expected in the benchmark experiments (Birgersson et al. 2009; Birgersson 2011 data files). To minimize temperature effects, reference solutions were kept at the same temperatures as the test solutions. The advantage of these methods is that solution sampling is avoided and therefore, the reservoir volume remains constant. The disadvantage is that dynamic concentration changes of both Na^+ and Ca^{2+} cannot be captured by the reference solutions.

For determination of the ionic concentration, it was assumed that electrical conductivity (σ) of a solution was a function of concentration (c) and temperature (T) according to the following equation:

$$\boldsymbol{\sigma = A * T + B * c + C * c * T + D} \qquad \textbf{(4-1)}$$

in which A, B, C and D are fitting parameters that were determined through a series of batch solutions with given concentrations of components and the corresponding measured electrical conductivities according to Birgersson (2011).

The assumption that the ion selectivity voltage (U) is a function of ionic concentration was applied for the transformation of the measured voltage to ionic concentration according to the equation:

$$\boldsymbol{c = E * exp(F * U)} \qquad \textbf{(4-2)}$$

where E and F are fitting parameters. Details can be found in the benchmark description and corresponding data files (Birgersson 2011).

The chemical analyses methods for Benchmark IV were: ion chromatography (IC) for major cations and anions, and the isotope ratio mass spectrometry (IRMS) for the isotopic ratio of HTO (Fernández et al. 2011).

The objectives of simulating these experiments are to: 1) compare the results obtained with MIN3P-THCm to the experimental data and also to results obtained by other groups using different codes (e.g. CrunchFlow, PHREEQC), where available; 2) develop an understanding of the reasons for any differences observed; and 3) identify requirements for further code development.

5. BENCHMARK I: THROUGH-DIFFUSION

Benchmark I consists of a set of laboratory through-diffusion experiments of salts through purified homo-ionic montmorillonite (Birgersson 2011). The aim of the experiments was to investigate the salt diffusion properties, without ion exchange, in Na- or Ca-montmorillonite.

5.1 DESCRIPTION OF EXPERIMENT

The through-diffusion experimental setup is depicted schematically in Figure 1. The sample (powder of Na- or Ca-montmorillonite) was placed in cylindrical steel test cells with a 35 mm inner diameter and was compacted to a thickness of 5.35 mm (Na-montmorillonite) or 7.5 mm

(Ca-montmorillonite). The sample was then saturated with distilled water and the swelling pressure was continuously measured. The sample was assumed to be fully saturated when the swelling pressure reached a constant value. Details of the experimental setup and procedure can be found in Birgersson et al. (2009), Birgersson (2011) and Karnland et al. (2006).

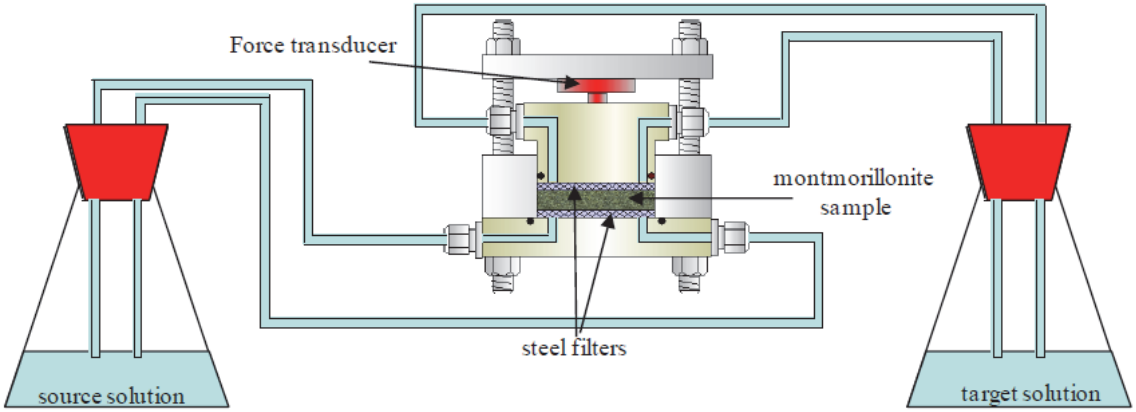

Figure 1: Schematic Diagram of the Through-Diffusion Experimental Setup (from Birgersson et al. 2009)

For the diffusion experiments using Na-montmorillonite, a large volume (250 ml) of NaCl solution was placed in the source reservoir connected to one side of the sample, so that the source solution concentration drop is negligible during the course of the diffusion test. Three experiments were run at a different NaCl concentration (Table 1). The other side of the sample was connected to a flask containing 100 ml of de-ionized water, which acted as the target solution (Figure 1). Both the source solution and the target solution were continuously circulated through the filters that were located on either side of the sample (Figure 1). Similar experiments were undertaken for Ca-montmorillonite, using 250 ml $CaCl_2$ solution with three different concentrations as the source solution. For cases with highly concentrated source solutions, the target solution was regularly changed to maintain low ion concentrations in the target reservoir. In total, six diffusion experiments were conducted with different types of montmorillonite and source salt concentrations (Table 1). Because the cation (Na^+ or Ca^{2+}) in the source reservoir solution was the same as the adsorbed cation present in the corresponding Na- or Ca-montmorillonite, ion exchange is expected to be negligible in these through-diffusion experiments.

Table 1: Source Solution Concentrations Used for the Na-montmorillonite and Ca-montmorillonite Through-Diffusion Experiments

Experiment No.	Na-Montmorillonite	Experiment No.	Ca-Montmorillonite
B1.1a	0.1 M NaCl	B1.2a	0.025 M $CaCl_2$
B1.1b	0.4 M NaCl	B1.2b	0.1 M $CaCl_2$
B1.1c	1.0 M NaCl	B1.2c	0.4 M $CaCl_2$

5.2 MODEL SETUP AND MATERIAL PROPERTIES

The size and soil physical parameters of the Na- and Ca-montmorillonite samples are listed in Table 2. Based on the experimental setup discussed above, one-dimensional (1D) models were adopted to simulate the through-diffusion experiments. As an example, the 1D model for case B1.1a (Table 1) is shown schematically in Figure 2. In the model, the thickness of the Na-montmorillonite sample is 5.35 mm, while both the source and target reservoirs are represented with a model cell thickness of 1 mm. To account for the actual volume of the reservoirs, porosities (representing the reservoir capacities) of 259.8 and 103.9 were applied to the source and target reservoir cells, respectively. These reservoir capacities were calculated considering the diameter of the sample is 35mm and the model reservoir thickness is 1 mm. The tortuosity values of the reservoir cells were set to 100.0 to mimic complete turbulent mixing within these cells due to circulation of the source and target solutions in the experiment (see Figure 1). The steel filters present on either side of the samples were not included in the model discretization due to the lack of detailed information such as the thickness, porosity and diffusion parameters of the filters.

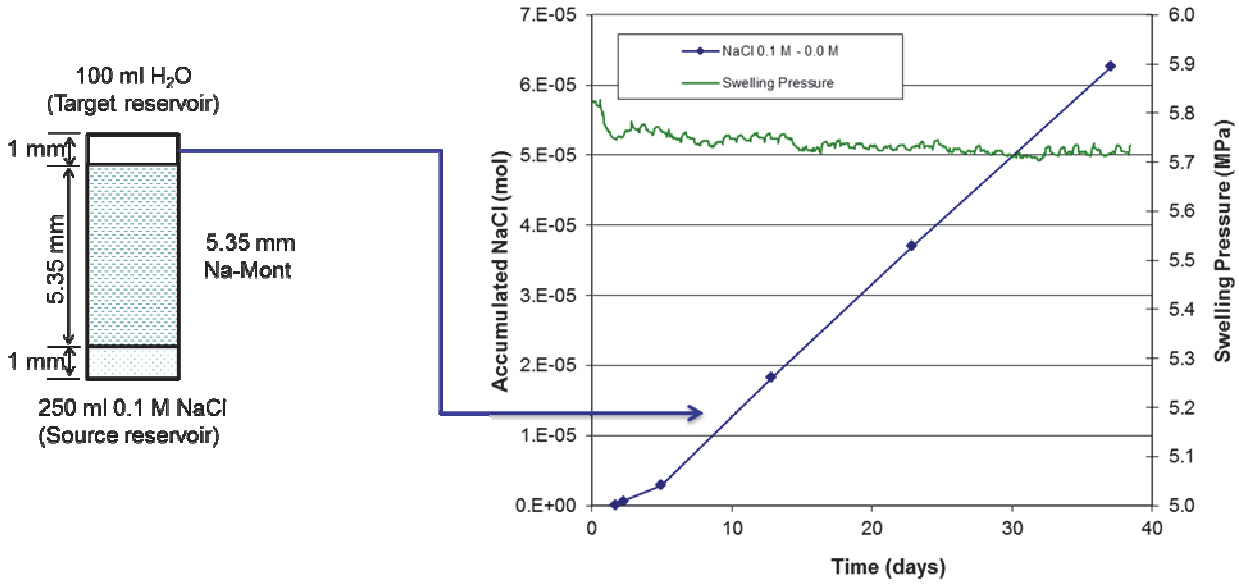

Figure 2: Depiction of the One-Dimensional Model for the B1.1a Through-Diffusion Experiment (Left), and the Experimental Results Obtained for the Accumulated NaCl Mass and the Swelling Pressure (Right)

The 1D model was discretized into 91 cells and includes two components (Na^+ & Cl^- for Na-montmorillonite cases, or Ca^{2+} & Cl^- for Ca-montmorillonite cases). Automatic time stepping (with a maximum timestep of 1.0 day) was applied. No flow boundaries were set for both ends of the model. The multicomponent diffusion module (MCD) as described in section 3.1 was applied for all simulations. The free aqueous solution diffusion coefficients (D_0) for the relevant species are listed in Table 3 (Lide 1994) and are fixed parameters in the calculations.

Table 2: Dimensions and Physical Parameters of the Test Samples for Benchmark I (Birgersson et al. 2009)

Parameters	Na-montmorillonite	Ca-montmorillonite
Thickness	5.35 mm *)	7.8 mm
Diameter	35 mm	35 mm
Water-to-solid mass ratio, w	0.35	0.41
Dry density (calculated from w)	1.40 g cm^{-3}	1.30 g cm^{-3}
Dry density (calculated from geometry and mass)	- *)	1.31 g cm^{-3}
Porosity (calculated from w)	0.49	0.53

*) The thickness of this sample was not measured explicitly. This value was obtained by setting the dry density calculated from volume and (dry) mass equal to that calculated from water-to-solid mass ratio.

Table 3: Free Aqueous Diffusion Coefficients (D_0) of Relevant Species (Lide 1994)

Species	D_0 [x$10^{-9}m^2$ s^{-1}]	Species	D_0 [x$10^{-9}m^2$ s^{-1}]
Ca^{2+}	0.792	SO_4^{2-}	1.065
Na^{+}	1.334	CO_3^{2-}	0.923
K^{+}	1.957	Cl^{-}	2.032
Mg^{2+}	0.706	HCO_3^{-}	1.18
H^{+}	9.311	$SiO_{2,aq}$	1.00
Al^{3+}	0.514	Tracer	1.87

5.3 RESULTS FOR EXPERIMENTS USING NA-MONTMORILLONITE

5.3.1 B1.1a: 0.1 mol L^{-1} NaCl Source Solution

The simulation approach taken in this work was to first assign values for the free-solution diffusion coefficients for Na^+ and Cl^- (Table 3) and then to estimate the effective porosity and tortuosity by inverse modelling using MIN3P-THCm and the PEST software. Two approaches were taken: a) both the effective porosity and tortuosity were adjusted as matching parameters, and b) only the tortuosity was adjusted, while porosity was considered a fixed parameter. For the cases in which only the tortuosity was adjusted, a total porosity value (0.49) based on previous modelling results presented at EBS TF-C workshops (Birgersson 2009; de Soto et al. 2011) was used.

A summary of the results of both simulation approaches is given in Table 4 and Figure 3. When both the effective porosity and tortuosity are adjusted, the best estimates for these parameters are 0.0762 and 0.00975, respectively. The effective diffusion coefficients (D_e) of Na^+ and Cl^- are thus calculated to be 9.91×10^{-13} m^2 s^{-1} and 1.51×10^{-12} m^2 s^{-1}, respectively. The comparison of the simulated results for accumulated NaCl mass in the target reservoir with the observed data shows that by adjusting only the tortuosity, a correlation coefficient of 0.981 is obtained, while essentially perfect agreement is obtained if both the effective porosity and tortuosity are adjusted (Table 4 and Figure 3).

Table 4: Experimental and Simulated Results for Accumulated NaCl Mass in the Target Reservoir for Case B1.1a

		Tortuosity and effective porosity adjusted		Tortuosity only adjusted	
Time	**Measured accumulated NaCl mass**	**Simulated accumulated NaCl mass**	**Residual**	**Simulated accumulated NaCl mass**	**Residual**
[day]	**[mol]**	**[mol]**	**[mol]**	**[mol]**	**[mol]**
1.70	7.16×10^{-8}	2.32×10^{-7}	-1.60×10^{-7}	2.77×10^{-10}	7.13×10^{-8}
2.24	6.54×10^{-7}	5.47×10^{-7}	1.07×10^{-7}	2.47×10^{-9}	6.51×10^{-7}
4.94	2.93×10^{-6}	3.84×10^{-6}	-9.10×10^{-7}	3.13×10^{-7}	2.62×10^{-6}
12.82	1.82×10^{-5}	1.78×10^{-5}	4.73×10^{-7}	8.32×10^{-6}	9.92×10^{-6}
22.87	3.70×10^{-5}	3.65×10^{-5}	5.16×10^{-7}	3.01×10^{-5}	6.95×10^{-6}
37.07	6.26×10^{-5}	6.30×10^{-5}	-3.95×10^{-7}	6.87×10^{-5}	-6.10×10^{-6}
Correlation coefficient		1.000		0.981	
Estimated parameters		**Value**	**95% confidence limits**	**Value**	**95% confidence limits**
Effective porosity		7.62×10^{-2}	5.51×10^{-2} to 9.72×10^{-2}	-[(1)]	
Tortuosity		9.75×10^{-3}	7.54×10^{-3} to 1.18×10^{-2}	2.44×10^{-3}	2.13×10^{-3} to 2.76×10^{-3}
Fixed parameter					
Porosity		-		0.49[(2)]	
Calculated parameters					
D_e for Na^+ in [m^2 s^{-1}]		9.91×10^{-13}		1.60×10^{-12}	
D_e for Cl^- in [m^2 s^{-1}]		1.51×10^{-12}		2.43×10^{-12}	

(1) porosity was defined as a fixed parameter
(2) representing total porosity

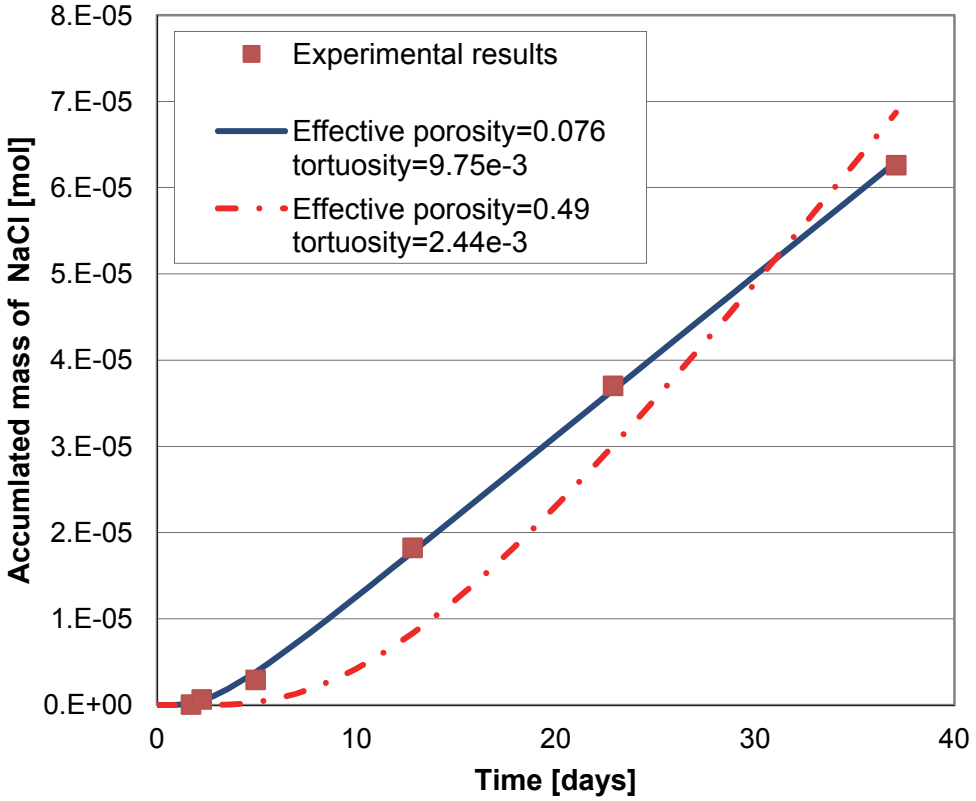

Figure 3: Comparison of MIN3P-THCm Results (Lines) and Experimental Data (Symbols) for Accumulated NaCl Mass in the Target Reservoir for Case B1.1a

5.3.2 B1.1b: 0.4 mol L^{-1} NaCl Source Solution

Based on the simulated results for the B1.1a case, the same simulation approach, in which both the effective porosity and tortuosity were adjusted, was taken for B1.1b. The simulated results for B1.1b are summarized in Figure 4 and Table 5. In comparison to the values obtained for B1.1a, both the tortuosity and effective porosity are higher, as might be expected based on the electrical double layer theory (Wersin et al. 2004; Kozaki et al. 2008), caused by the increase in ionic strength of the source solution.

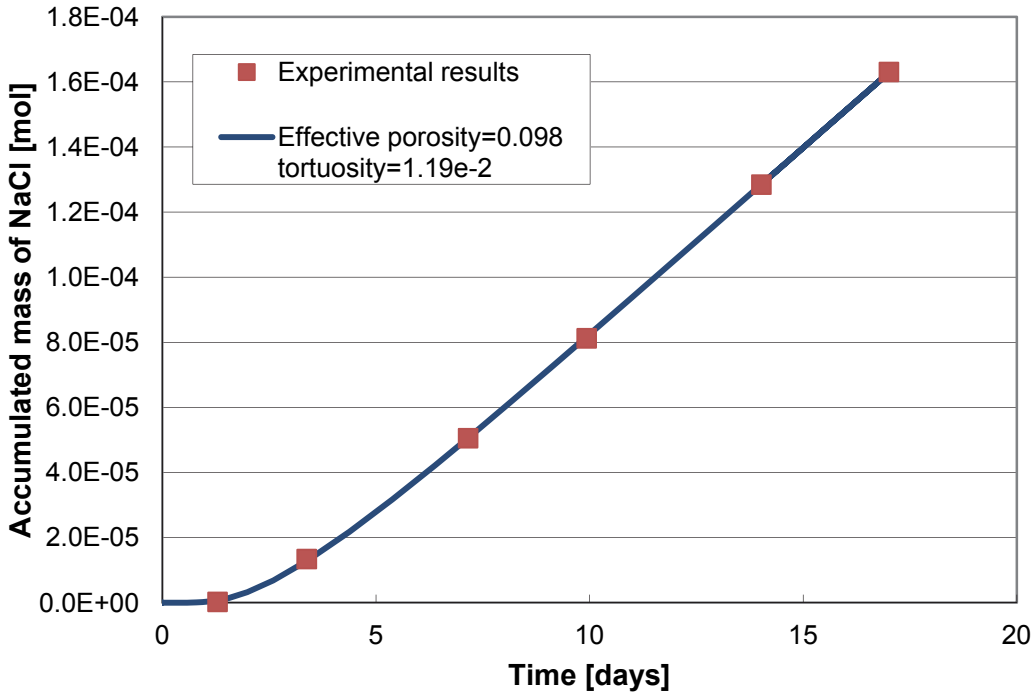

Figure 4: Comparison of MIN3P-THCm Results (Line) and Experimental Data (Symbols) for Accumulated NaCl Mass in the Target Reservoir for Case B1.1b

Table 5: Experimental and Simulated Results for Accumulated NaCl Mass for Case B1.1b

Time	Accumulated NaCl mass in the target reservoir		
	Measured	Simulated	Residual
[day]	[mol]	[mol]	[mol]
1.29	2.49×10^{-7}	7.01×10^{-7}	-4.52×10^{-7}
3.38	1.34×10^{-5}	1.28×10^{-5}	6.66×10^{-7}
7.16	5.06×10^{-5}	5.06×10^{-5}	-5.36×10^{-8}
9.93	8.12×10^{-5}	8.17×10^{-5}	-4.31×10^{-7}
14.02	1.29×10^{-4}	1.29×10^{-4}	-2.05×10^{-8}
17.01	1.63×10^{-4}	1.63×10^{-4}	2.00×10^{-7}
Correlation coefficient		1.000	
Estimated parameters		**Value**	**95% confidence limits**
Effective porosity		9.78×10^{-2}	0.0903 – 0.105
Tortuosity		1.19×10^{-2}	1.11×10^{-2} – 1.26×10^{-2}
Calculated parameters			
D_e for Na^+ in [m^2 s^{-1}]		1.55×10^{-12}	
D_e for Cl^- in [m^2 s^{-1}]		2.35×10^{-12}	

5.3.3 B1.1c: 1.0 mol L^{-1} NaCl Source Solution

For the B1.1c case, the tortuosity and effective porosity were obtained using the same approach as discussed above. The simulated results for this experiment are summarized in Figure 5 and Table 6. Simulated results for the accumulated NaCl mass in the target reservoir show excellent agreement to the experimental data and predict a further increase in effective porosity, consistent with the electric double layer theory.

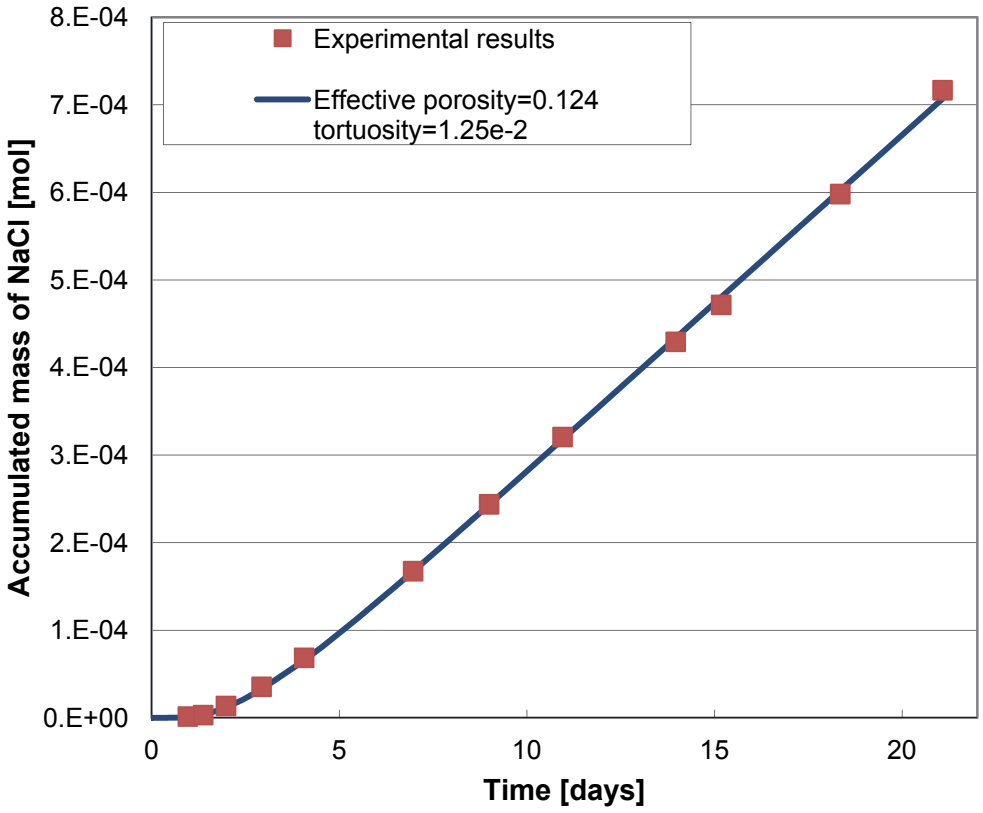

Figure 5: Comparison of MIN3P-THCm Results (Line) and Experimental Data (Symbols) for Accumulated NaCl Mass in the Target Reservoir for Case B1.1c

Table 6: Experimental and Simulated Results for the Accumulated NaCl Mass for Case B1.1c

Time	Accumulated NaCl mass in the target reservoir		
	Measured	Simulated	Residual
[day]	[mol]	[mol]	[mol]
0.97	$1.44x10^{-6}$	$8.32x10^{-7}$	$6.06x10^{-7}$
1.38	$3.16x10^{-6}$	$3.56x10^{-6}$	$-4.02x10^{-7}$
1.98	$1.36x10^{-5}$	$1.16x10^{-5}$	$1.98x10^{-6}$
2.93	$3.54x10^{-5}$	$3.25x10^{-5}$	$2.93x10^{-6}$
4.06	$6.85x10^{-5}$	$6.55x10^{-5}$	$2.95x10^{-6}$
6.97	$1.68x10^{-4}$	$1.67x10^{-4}$	$3.07x10^{-7}$
8.99	$2.44x10^{-4}$	$2.43x10^{-4}$	$7.90x10^{-7}$
10.95	$3.21x10^{-4}$	$3.18x10^{-4}$	$2.77x10^{-6}$
13.96	$4.30x10^{-4}$	$4.34x10^{-4}$	$-4.06x10^{-6}$
15.18	$4.72x10^{-4}$	$4.80x10^{-4}$	$-8.88x10^{-6}$
18.35	$5.98x10^{-4}$	$6.02x10^{-4}$	$-4.11x10^{-6}$
21.07	$7.17x10^{-4}$	$7.07x10^{-4}$	$1.01x10^{-5}$
Correlation coefficient		1.000	
Estimated parameters		**Value**	**95% confidence limits**
Effective porosity		$1.24x10^{-1}$	$1.10x10^{-1} – 1.38x10^{-1}$
Tortuosity		$1.25x10^{-2}$	$1.13x10^{-2} – 1.37x10^{-2}$
Calculated parameters			
D_e for Na^+ in [m^2 s^{-1}]		$2.07x10^{-12}$	
D_e for Cl^- in [m^2 s^{-1}]		$3.15x10^{-12}$	

5.4 RESULTS FOR EXPERIMENTS USING CA-MONTMORILLONITE

The numerical simulations were conducted using the MCD model of MIN3P-THCm and PEST to estimate both tortuosity and effective porosity for three through-diffusion experiments using Ca-montmorillonite with different $CaCl_2$ concentration in the source solutions (Table 1).

5.4.1 B1.2a: 0.025 mol L^{-1} $CaCl_2$ Source Solution

The experimental and simulated results from this experiment are summarized in Figure 6 and Table 7. The simulated results for the accumulated $CaCl_2$ mass in the reservoir show excellent agreement to the experimental data. The estimated effective porosity and tortuosity are 0.178 and 0.054, respectively. The effective diffusion coefficients (D_e) for Ca^{2+} and Cl^- are thus calculated to be $7.61x10^{-12}$ m^2 s^{-1} and 1.95 $x10^{-11}$ m^2 s^{-1}, respectively.

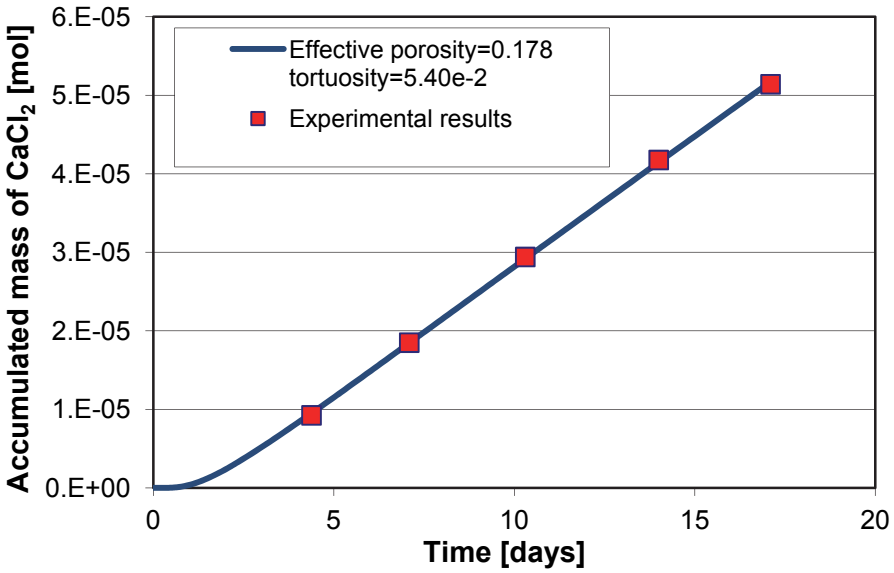

Figure 6: Comparison of Simulated MIN3P-THCm Result (Line) and Experimental Data (Symbols) for Accumulated $CaCl_2$ Mass in the Target Reservoir for Case B1.2a

Table 7: Experimental and Simulated Results of the Accumulated $CaCl_2$ Mass for Case B1.2a

Time	Accumulated $CaCl_2$ mass in the target reservoir		
	Measured	Simulated	Residual
[day]	[mol]	[mol]	[mol]
4.38	$9.24x10^{-6}$	$9.51x10^{-6}$	$-2.66x10^{-7}$
7.09	$1.85x10^{-5}$	1.8510^{-5}	$3.77x10^{-8}$
10.30	$2.94x10^{-5}$	$2.92x10^{-5}$	$2.27x10^{-7}$
14.00	$4.18x10^{-5}$	$4.15x10^{-5}$	$2.75x10^{-7}$
17.10	$5.14x10^{-5}$	$5.17x10^{-5}$	$-3.16x10^{-7}$
Correlation coefficient		1.000	
Estimated parameters		**Value**	**95% confidence limits**
Effective porosity		0.178	0.135 – 0.221
Tortuosity		$5.40x10^{-2}$	$4.28x10^{-2}$ – $6.52x10^{-2}$
Calculated parameters			
D_e for Ca^{2+} in [m^2 s^{-1}]		$7.61x10^{-12}$	
D_e for Cl^- in [m^2 s^{-1}]		$1.95x10^{-11}$	

5.4.2 B1.2b: 0.1 mol L^{-1} $CaCl_2$ Source Solution

The experimental and simulated results for this experiment are summarized in Figure 7 and Table 8. Similar to previous simulations, this benchmark set shows very good agreement between experimental and simulated results for accumulated $CaCl_2$ mass in the target reservoir. The estimated effective porosity and tortuosity are 0.201 and 0.061 respectively. The effective

diffusion coefficients (D_e) of Ca^{2+} and Cl^- are calculated to be $9.65x10^{-12}$ m^2 s^{-1} and $2.47x10^{-11}m^2s^{-1}$ respectively.

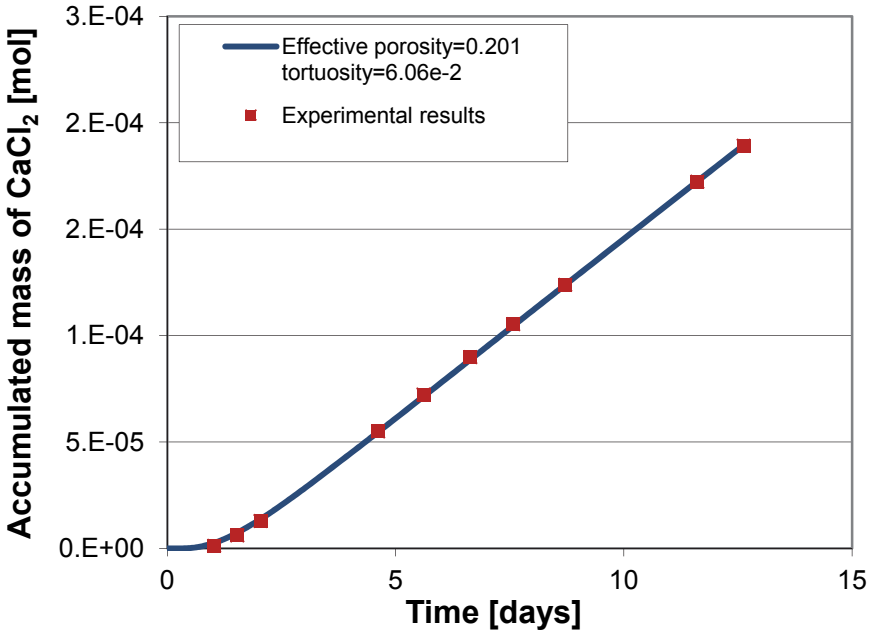

Figure 7: Comparison of MIN3P-THCm Result (Line) and Experimental Data (Symbols) for Accumulated $CaCl_2$ Mass in the Target Reservoir for Case B1.2b

Table 8: Experimental and Simulated Results of Accumulated $CaCl_2$ Mass for Case B1.2b

Time	Accumulated $CaCl_2$ mass in the target reservoir		
	Measured	Simulated	Residual
[day]	[mol]	[mol]	[mol]
1.03	$1.24x10^{-6}$	$2.66x10^{-6}$	$-1.42x10^{-6}$
1.53	$6.11x10^{-6}$	$7.30x10^{-6}$	$-1.19x10^{-6}$
2.04	$1.29x10^{-5}$	$1.37x10^{-5}$	$-8.38x10^{-7}$
4.62	$5.50x10^{-5}$	$5.47x10^{-5}$	$2.63x10^{-7}$
5.61	$7.23x10^{-5}$	$7.14x10^{-5}$	$9.17x10^{-7}$
6.64	$8.99x10^{-5}$	$8.88x10^{-5}$	$1.12x10^{-6}$
7.58	$1.05x10^{-4}$	$1.05x10^{-4}$	$3.19x10^{-7}$
8.72	$1.24x10^{-4}$	$1.24x10^{-4}$	$5.03x10^{-8}$
11.61	$1.72x10^{-4}$	$1.73x10^{-4}$	$-5.83x10^{-7}$
12.62	$1.89x10^{-4}$	$1.90x10^{-4}$	$-5.04x10^{-7}$
Correlation coefficient		1.000	
Estimated parameters		**Value**	**95% confidence limits**
Effective porosity		0.201	0.183 – 0.219
Tortuosity		$6.06x10^{-2}$	$5.60x10^{-2}$ – $6.53x10^{-2}$
Calculated parameters			
D_e for Ca^{2+} in [m^2 s^{-1}]		$9.65x10^{-12}$	
D_e for Cl^- in [m^2 s^{-1}]		$2.47x10^{-11}$	

5.4.3 B1.2c: 0.4 mol L^{-1} $CaCl_2$ Source Solution

The experimental and simulated results are summarized in Figure 8 and Table 9. The simulated results for accumulated $CaCl_2$ mass in the target reservoir are in excellent agreement with the observed data. The estimated effective porosity and tortuosity are 0.196 and 0.066, respectively. The effective diffusion coefficients (D_e) of Ca^{2+} and Cl^- are calculated to be 1.02×10^{-11} m^2 s^{-1} and 2.62×10^{-11} m^2 s^{-1} respectively. Simulations predict an increase in effective diffusion coefficients in comparison to the lower ionic strength source reservoir solutions, as might be expected based on the electrical double layer theory for an increase of the ionic strength of the source solution (Wersin et al. 2004; Kozaki et al. 2008).

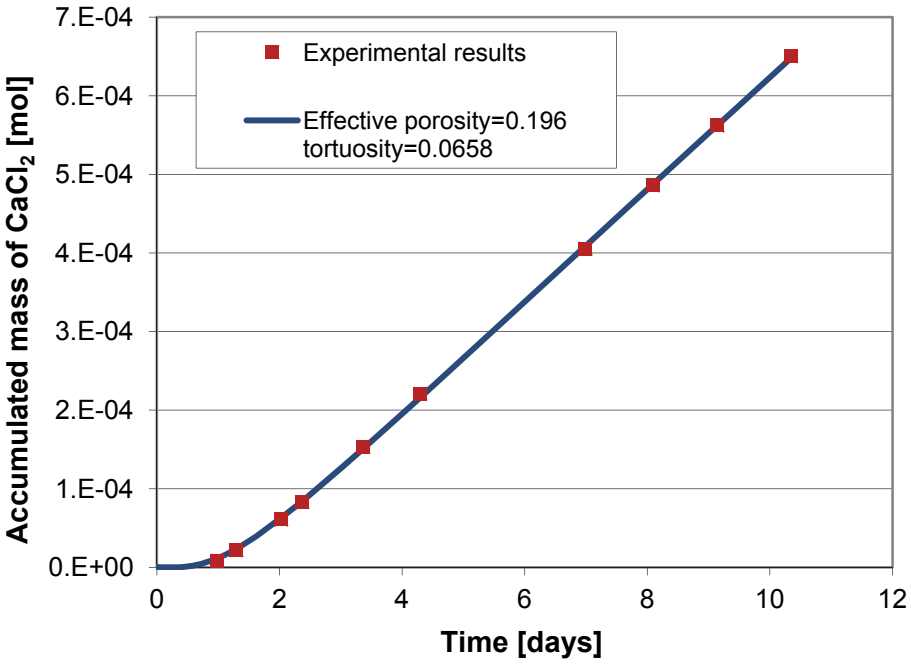

Figure 8: Comparison of MIN3P-THCm Result (Line) and Experimental Data (Symbols) for Accumulated $CaCl_2$ Mass in the Target Reservoir for Case B1.2c

Table 9: Experimental and Simulated Results of the Accumulated $CaCl_2$ for Case B1.2c

Time	Accumulated $CaCl_2$ mass in the target reservoir		
	Measured	Simulated	Residual
[day]	[mol]	[mol]	[mol]
0.98	$8.36x10^{-6}$	$1.14x10^{-5}$	$-3.07x10^{-6}$
1.29	$2.18x10^{-5}$	$2.33x10^{-5}$	$-1.48x10^{-6}$
2.03	$6.10x10^{-5}$	$6.29x10^{-5}$	$-1.87x10^{-6}$
2.37	$8.32x10^{-5}$	$8.42x10^{-5}$	$-9.96x10^{-7}$
3.37	$1.53x10^{-4}$	$1.51x10^{-4}$	$2.12x10^{-6}$
4.29	$2.21x10^{-4}$	$2.16x10^{-4}$	$5.05x10^{-6}$
6.99	$4.05x10^{-4}$	$4.09x10^{-4}$	$-3.59x10^{-6}$
8.09	$4.86x10^{-4}$	$4.88x10^{-4}$	$-1.55x10^{-6}$
9.14	$5.62x10^{-4}$	$5.62x10^{-4}$	$-4.03x10^{-7}$
10.35	$6.50x10^{-4}$	$6.48x10^{-4}$	$2.02x10^{-6}$
Correlation coefficient		1.000	
Estimated parameters		**Value**	**95% confidence limits**
Effective porosity		0.196	0.182 – 0.210
Tortuosity		$6.58x10^{-2}$	$6.20x10^{-2}$ – $6.97x10^{-2}$
Calculated parameters			
D_e for Ca^{2+} in [m^2 s^{-1}]		$1.02x10^{-11}$	
D_e for Cl^- in [m^2 s^{-1}]		$2.62x10^{-11}$	

5.5 SUMMARY AND DISCUSSION

Based on the simulation results for Benchmark I presented above, the calibrated effective diffusion coefficients for Na^+, Ca^{2+} and Cl^- increase with increasing ionic strength of the source solutions (from 0.1 to 1.0 M for NaCl source solutions, Table 10, and from 0.075 to 1.2 M for $CaCl_2$ source solutions, Table 11). This can be explained by a decrease in the thickness of the diffuse double layer, which is associated with the surface of the negatively charged clay minerals (Yeung 1992; Xie et al. 2004).

Table 10: Summary of Estimated/Simulated Diffusion Parameters Based on the Through-Diffusion Experiments Using Na-Montmorillonite

Parameter	Unit	B1.1a	B1.1b	B1.1c
Ionic strength	[mol L^{-1}]	0.1	0.4	1.0
Effective porosity	[-]	0.0762	0.0978	0.1240
Tortuosity	[-]	$9.75x10^{-3}$	$1.19x10^{-2}$	$1.25x10^{-2}$
D_e for Na^+	[m^2 s^{-1}]	$9.91x10^{-13}$	$1.55x10^{-12}$	$2.07x10^{-12}$
D_e for Cl^-	[m^2 s^{-1}]	$1.51x10^{-12}$	$2.35x10^{-12}$	$3.15x10^{-12}$

Table 11: Summary of Estimated/Simulated Diffusion Parameters Based on the Through-Diffusion Experiments Using Ca-montmorillonite

Parameter	Unit	B1.2a	B1.2b	B1.2c
Ionic strength	[mol L^{-1}]	0.075	0.300	1.200
Effective porosity	[-]	0.178	0.201	0.196
Tortuosity	[-]	5.40×10^{-2}	6.06×10^{-2}	6.58×10^{-2}
D_e for Ca^{2+}	[m^2 s^{-1}]	7.61×10^{-12}	9.65×10^{-12}	1.02×10^{-11}
D_e for Cl^-	[m^2 s^{-1}]	1.95×10^{-11}	2.47×10^{-11}	2.62×10^{-11}

Direct comparison of the simulation results obtained with MIN3P-THCm to results from other codes that are based on a similar formulation to MIN3P-THCm is not possible at the present time due to a lack of alternative results. However, Birgersson (2009) presented an alternative solution method based on the Donnan equilibrium approach (Birgersson and Karnland 2009). According to this approach, compacted bentonite acts as a semi-permeable membrane and prevents anions and - due to electrostatic coupling effects - also cations from entering the bentonite. Therefore, a concentration jump exists at the interface between the reservoir and the bentonite. For example, if the Na^+ concentration in the reservoir adjacent to the compacted bentonite is 1.0 M (B1.1c), the "actual" concentration (C_0 or inlet concentration) in bentonite near the reservoir is assumed to be lower due to the membrane effect, i.e. 0.29 mol L^{-1} (Table 12). In this approach, the actual porewater diffusion coefficient D_c is defined as:

$$\frac{\partial c(x,t)}{\partial t} = D_c \frac{\partial^2 c(x,t)}{\partial x^2} \qquad \textbf{(5-1)}$$

in which c(x,t) is the concentration, t is time, and x is distance. The optimized C_0 and D_c values are listed in Table 12 (for through-diffusion experiments in Na-montmorillonite) and Table 13 (for through-diffusion experiments in Ca-montmorillonite).

Table 12: Summary of Estimated/Simulated Diffusion Parameters for the Experiments Using Na-montmorillonite (Birgersson, Unpublished Data) Based on the Donnan Equilibrium Approach (Birgersson 2009)

Parameter	Unit	B1.1a	B1.1b	B1.1c
Ionic strength	[mol L^{-1}]	0.1	0.4	1.0
C_0	[mol L^{-1}]	0.014	0.086	0.29
D_c for Na^+	[m^2 s^{-1}]	1.60×10^{-11}	1.60×10^{-11}	1.60×10^{-11}

Table 13: Summary of Estimated/Simulated Diffusion Parameters for the Experiments Using Ca-montmorillonite (Birgersson, Unpublished Data) Based on the Donnan Equilibrium Approach (Birgersson 2009)

Parameter	Unit	B1.2a	B1.2b	B1.2c
Ionic strength	[mol L^{-1}]	0.075	0.3	1.2
C_0	[mol L^{-1}]	0.007	0.036	0.16
D_c for Ca^{2+}	[m^2 s^{-1}]	$8.30x10^{-11}$	$8.30x10^{-11}$	$8.30x10^{-11}$

In this approach, the actual porewater diffusion coefficient D_c depends only on the type of bentonite and does not vary with the ionic strength of the porewater solution. Differences in migration are attributed to the variation of the porewater solution concentrations (C_0) at the inlet boundary owing to the Donnan equilibrium effect. Numerical simulation using PHREEQC and CrunchFlow were undertaken using an adjusted C_0 instead of the measured concentration in the reservoir. These simulations did not make use of the MCD capabilities of PHREEQC and Crunchflow and used the inlet concentrations C_o and D_c as the main model calibration parameters. Using this approach, a good fit was also obtained with the experimental data (Birgersson, unpublished data). In a follow-up study, additional simulations were conducted using D_c as the only calibration parameter, while C_o values were calculated based on the Donnan equilibrium approach (Birgersson, unpublished data). These simulations were also able to capture the trend of experimental observations, but the quality of the fit to the experimental data was not as favorable as for the earlier results obtained by Birgersson (unpublished data) or the simulations presented here.

Holton (2013) presented modelling results using an analytical solution for salt diffusion in Na- and Ca-montmorillonite. This approach uses a single diffusion coefficient for all species and does not account for MCD effects. The simulated effective porosity and intrinsic diffusion coefficients (D_i) are listed in Table 14 and Table 15. Effective porosity values are very close to the estimated values by MIN3P-THCm. The intrinsic diffusion coefficient (D_i) as defined by Holton (2013) is equivalent to the effective diffusion coefficient (D_e), as defined in this study. The D_i values are also very similar to those obtained by MIN3P-THCm if the D_e values for Na^+ and Cl^- are averaged, which is close to the actual effective diffusion coefficient for a double ionic system (e.g. Na^+ and Cl^-) implicitly considering the multicomponent diffusion effect (compare Table 10 and Table 14, Table 11 and Table 15).

Table 14: Summary of Estimated/Simulated Diffusion Parameters for Benchmark I Experiments Using Na-Montmorillonite Based on the Analytical Approach by Holton (2013)

Parameter	Unit	B1.1a	B1.1b	B1.1c
Ionic strength	[mol L^{-1}]	0.1	0.4	1.0
Effective porosity	[-]	0.059	0.087	0.095
D_i for NaCl	[m^2 s^{-1}]	$1.14x10^{-12}$	$1.85x10^{-12}$	$2.31x10^{-12}$

Table 15: Summary of Estimated/Simulated Diffusion Parameters for Benchmark I Experiments Using Ca-Montmorillonite Based on the Analytical Approach by Holton (2013)

Parameter	Unit	B1.2a	B1.2b	B1.2c
Ionic strength	[mol L^{-1}]	0.075	0.300	1.200
Effective porosity	[-]	0.21	0.21	0.19
D_i for $CaCl_2$	[m^2 s^{-1}]	$1.25x10^{-11}$	$1.54x10^{-11}$	$1.68x10^{-11}$

6. BENCHMARK II: MINERAL DISSOLUTION AND DIFFUSION

Benchmark II includes two types of diffusion experiments with increasing complexity. Benchmark B2.1 focuses on through-diffusion, B2.2a includes diffusion and mineral dissolution, and Benchmark B2.2b considers diffusion, mineral dissolution, ion exchange. The first benchmark of this task is a through-diffusion experiment in Ca-montmorillonite, similar to Benchmark I (Figure 1), but using a source solution in equilibrium with gypsum. The second benchmark deals with gypsum dissolution and diffusion (Figure 9) (Birgersson et al. 2009; Birgersson 2011). The former serves as a pure diffusion experiment to obtain the effective diffusion parameters for $CaSO_4$(aq) transport through compacted Ca-montmorillonite. The latter investigates the diffusion processes in a more complex geochemical environment. For the second set of experiments, two cases are considered, one with Ca montmorillonite, and another with Na-montmorillonite. In the latter case, cation exchange between Na^+ and Ca^{2+} must also be considered. A summary of the three cases and the related processes is provided in Table 16. The sample sizes and properties are listed in Table 17.

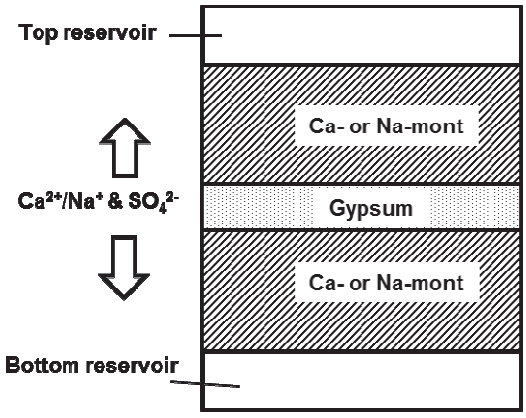

Figure 9: Concept for Benchmark II Simulations: Gypsum Dissolution and $CaSO_4$ Diffusion

Table 16: Benchmark II Mineral Dissolution and Migration Experiments

Case	B2.1	B2.2a	B2.2b
Soil type (initial)	Ca-Montmorillonite	Ca-Montmorillonite	Na-Montmorillonite
Description	$CaSO_4$ solution diffusion	Gypsum dissolution	Gypsum dissolution
Related processes			
Diffusion	√	√	√
Mineral dissolution		√	√
Cation exchange			√

Table 17: Dimensions and Soil Properties of Test Samples for Benchmark II (Birgersson et al. 2009; Birgersson 2011)

Parameters	Unit	B2.1	B2.2a	B2.2b
Montmorillonite thickness*)	[mm]	5	5	5
Diameter	[mm]	35	35	35
Water-to-solid mass ratio, w	[-]	0.35	0.38	0.32
Dry density (calculated from w)	[g cm^{-3}]	1.40	1.34	1.46
Porosity (from w)	[-]	0.49	0.51	0.47

*) These are nominal thicknesses; in the case of B2.2a and B2.2b, the sample thickness on either side of the gypsum layer was approximately equal

6.1 CASE B2.1: THROUGH-DIFFUSION OF $CASO_4$ IN CA-MONTMORILLONITE

6.1.1 Description of Experiment

The through-diffusion experiment was conducted in the same manner as described in Section 5.1. The Ca-montmorillonite sample was emplaced in a stainless steel cell, compacted (see Table 17 for dry density) and then saturated with de-ionized water. A flask containing a $CaSO_4$ solution saturated with respect to gypsum was connected to one side of the sample. Electrical conductivity, ion selectivity voltage, and temperature were regularly measured in the target solution. The measured results based on electrical conductivity were selected for comparison with the simulated results because data measured by this method showed fewer fluctuations than data obtained with the ion selective electrode method (Birgersson et al. 2009; Birgersson 2011).

6.1.2 Model Setup and Material Properties

A 1D model including the Ca-montmorillonite sample and both the source and target reservoirs was set up for the simulation. A MIN3P-THCm batch reaction calculation was conducted to calculate the chemical composition of the saturated $CaSO_4$ solution at 25°C, which is used as the initial chemical composition in the source reservoir.

The model setup and numerical method for the 1D through-diffusion experiment are the same as described in section 5.2 (Figure 2), except the thickness of the compacted bentonite is now 5.0 mm. The 1D model was discretized into 58 control volumes. No-flow boundary conditions were applied at both boundaries.

6.1.3 Simulation Results

The numerical analysis results of the through-diffusion experiment using MIN3P-THCm and PEST for optimizing the effective porosity and tortuosity are shown in Figure 10 and Table 18. The simulated results of the accumulated Ca^{2+} mass in the target reservoir agree very well with the experimental data (Figure 10) when the effective porosity is 0.052 and tortuosity is 0.104 (Table 18). The large confidence intervals for effective porosity and tortuosity are due to the interdependency of these parameters for the experimental conditions considered, which are dominated by quasi-steady state conditions (i.e. an increase of porosity can be compensated by a decrease in tortuosity and vice versa). The derived effective diffusion coefficients (D_e) for Ca^{2+} and SO_4^{2-} are 4.29×10^{-12} m^2 s^{-1} and 5.77×10^{-12} m^2 s^{-1}, respectively.

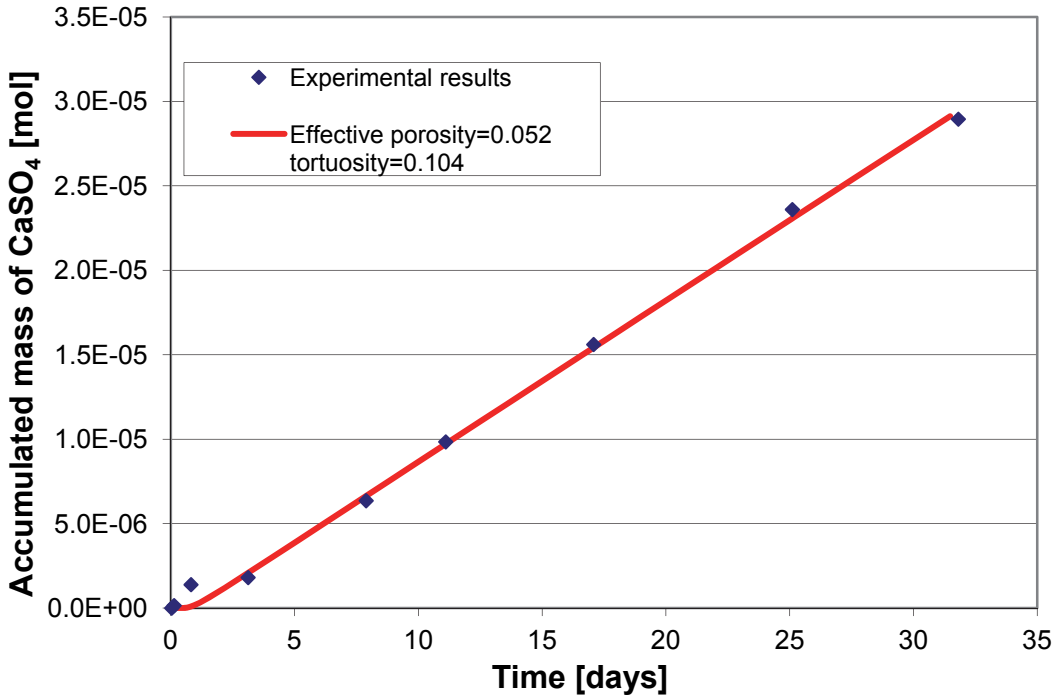

Figure 10: Comparison of Simulated Results and Experimental Data for Accumulated Ca^{2+} Mass in the Target Reservoir for Case B2.1

Table 18: Experimental Data and Simulated Results for the Accumulated Ca^{2+} Mass in the Target Reservoir for Case B2.1

Time	Accumulated Ca^{2+} mass in the target reservoir		
	Measured	Simulated	Residual
[day]	[mol]	[mol]	[mol]
0.13	$1.49x10^{-7}$	1.45×10^{-11}	1.49×10^{-7}
0.82	$1.39x10^{-6}$	1.33×10^{-7}	1.26×10^{-6}
3.12	$1.81x10^{-6}$	2.18×10^{-6}	-3.69×10^{-7}
7.89	$6.36x10^{-6}$	6.72×10^{-6}	-3.57×10^{-7}
11.10	$9.84x10^{-6}$	9.78×10^{-6}	6.58×10^{-8}
17.08	$1.56x10^{-5}$	1.55×10^{-5}	1.56×10^{-7}
25.10	$2.36x10^{-5}$	2.31×10^{-5}	5.46×10^{-7}
31.81	$2.90x10^{-5}$	2.94×10^{-5}	-4.35×10^{-7}
Correlation coefficient		0.999	
Estimated parameters		**Value**	**95% confidence limits**
Effective porosity		0.0520	0.0214 – 0.126
Tortuosity		0.104	0.0445 – 0.244
Calculated parameters			
D_e for Ca^{2+} in [m^2 s^{-1}]		$4.29x10^{-12}$	
D_e for SO_4^{2-} in [m^2 s^{-1}]		$5.77x10^{-12}$	

6.2 CASE B2.2A: GYPSUM DISSOLUTION AND DIFFUSION IN CA-MONTMORILLONITE

6.2.1 Description of Experiment

The concept of this experiment is schematically described in Figure 9. Two compacted homo-ionic Ca-montmorillonite samples, with a thickness of approximately 2.5 mm each, were placed in stainless steel cells and fully saturated with de-ionized water. The swelling pressure was measured to track the saturation of the samples. After saturation, the samples were dismantled and re-packed by placing a thin layer (<0.5 mm in thickness) of gypsum powder between them. The entire sample was then placed into a diffusion cell (Birgersson et al. 2009; Birgersson 2011), and connected to the top and bottom reservoirs with a volume of 100 mL of de-ionized water each connected to a circulation system. Electrical conductivities in the top and bottom reservoir solutions were regularly measured. Reference solutions with known concentrations of Ca^{2+} and SO_4^{2-} were used for the calibration and calculation of the concentrations of Ca^{2+} and SO_4^{2-} in the top and bottom reservoirs (Birgersson 2011).

6.2.2 Model Setup and Material Properties

A 1D model including three different material groups (i.e. reservoirs, montmorillonite and gypsum powder) in five layers was set up (Figure 9). The center of the model contains the layer of gypsum powder with an assumed thickness of 0.5 mm. Above and below the gypsum layer, Ca-montmorillonite with a thickness of 2.5 mm (unless specified otherwise) are emplaced. The top and bottom target reservoirs with a volume of 100 ml de-ionized water are in contact with

the montmorillonite layers, which were represented by cells with a thickness of 1 mm in the 1D model. To account for the actual volume of both reservoirs, a porosity (reservoir capacity) of 103.9 was specified for both reservoirs. The filters between reservoir and montmorillonite are not considered in the simulation owing to the lack of detailed information (e.g. thickness, porosity, tortuosity and diffusion coefficient). Equilibrium conditions were assumed for the gypsum dissolution-precipitation reaction in the gypsum layer. Gypsum exists only in the gypsum layer with an assumed volume fraction of 0.40 m^3 m^{-3}. This is a conservative estimate and the simulation result is insensitive to this parameter, because excess gypsum is present at the end of the simulations. This assumption is reasonable because the accumulated $CaSO_4$ remains increasing at the same rate (see Figure 12), indicating a constant flux of dissolved $CaSO_4$ originating from gypsum dissolution was occurring until the end of the experiment.

The dissolution of gypsum is described as a kinetic surface-controlled reaction based on the rate expression:

$$\boldsymbol{R_i^m = -k_i^m \left[1 - \left(\frac{IAP_i^m}{K_i^m}\right)\right]} \qquad \textbf{(6-1)}$$

where $\mathrm{R_i^m}$ is the reaction rate, $\mathrm{IAP_i^m}$ is the ion activity product, $\mathrm{K_i^m}$ is the equilibrium constant and $\mathrm{k_i^m}$ is the effective rate constant [mol L^{-1} s^{-1}]. The effective rate constants $\mathrm{k_i^m}$ for the mineral included in all benchmarks may vary as a function of mineral abundance at each time step. A two-third power relationship of the form:

$$\mathbf{k_i^{m,t} = -k_i^{m,0}\left(\frac{\varphi_i^t}{\varphi_i^0}\right)^{2/3}} \qquad \textbf{(6-2)}$$

is used to update the effective rate constant (Lichtner 1996). In this relationship, $\mathrm{k_i^{m,t}}$ and φ_i^t define the current effective rate constant and the current mineral volume fraction, respectively; while $\mathrm{k_i^{m,0}}$ and φ_i^0 define the initial effective rate constant and initial mineral volume fraction, respectively. The parameter $\mathbf{k_i^m}$ can be calculated according to:

$$\mathbf{k_i^m = k_s^m S} \qquad \textbf{(6-3)}$$

In which $\mathbf{k_s^m}$ is the surface-area normalized rate constant [mol m^{-2} s^{-1}], and **S** stands for the bulk surface area [m^2 (L bulk)$^{-1}$].

As no measured data for the gypsum powder used in the experiment was available, literature data was adopted. Colombani (2008) suggested $\mathbf{k_s^m}$ = 7.0x10^{-5} [mol m^{-2} s^{-1}] for gypsum powder. Assuming a surface area *S* of 0.7 m^2 g^{-1} (Hirao et al. 2012) and a bulk density of 1400 g L^{-1} for gypsum powder, $\mathbf{k_i^m}$ is calculated to be 6.86x10^{-2} mol L^{-1} s^{-1}; This value was used for the simulations of B2.2a and B2.2b benchmark experiments.

The simulations were undertaken in the following steps:

1) Direct simulation of diffusion using MIN3P-THCm was undertaken by applying the calibrated diffusion parameters obtained in the through-diffusion experiment B2.1. The diffusion parameters and the thicknesses of the top and bottom bentonite layers (i.e. 2.5 mm) were assumed to be the same. Owing to the symmetric experimental setup, the measured concentrations of Ca^{2+} and SO_4^{2-} in the top and bottom reservoirs should be the same at any given time. The accumulated mass of $CaSO_4$ curves in both reservoirs theoretically should be identical, which was not the case, however, in the experimental

results. Therefore, an averaged value of the measured accumulated mass of $CaSO_4$ was used for the comparison to the simulated results.

2) Optimization of the diffusion parameters (effective porosity and tortuosity) using MIN3P-THCm and PEST was conducted to provide the best fit to the average of the accumulated $CaSO_4$ in the top and bottom reservoir solutions. The optimization was based on the following assumptions: i) the Ca-montmorillonite samples comprising the top and bottom layers are characterized by the same diffusion parameters; ii) transport is diffusion-dominated (i.e. no advection) and conservative (no ion exchange reactions in the bentonite); iii) dissolution of gypsum occurred only in the center part of the domain; and iv) the thicknesses of the top and bottom bentonite layers were identical at 2.5 mm.

3) In order to explain the differences between the measured $CaSO_4$ accumulated mass in the top and bottom reservoirs, the thickness of the top and bottom bentonite layers were adjusted within the experimental tolerances to optimize the fit of the simulated results to the measured data.

6.2.3 Simulation Results

6.2.3.1 Diffusion parameter estimation

The comparison of simulated and averaged experimental results for the accumulated $CaSO_4$ mass in the top and bottom reservoirs is shown in Figure 11 and Table 19.

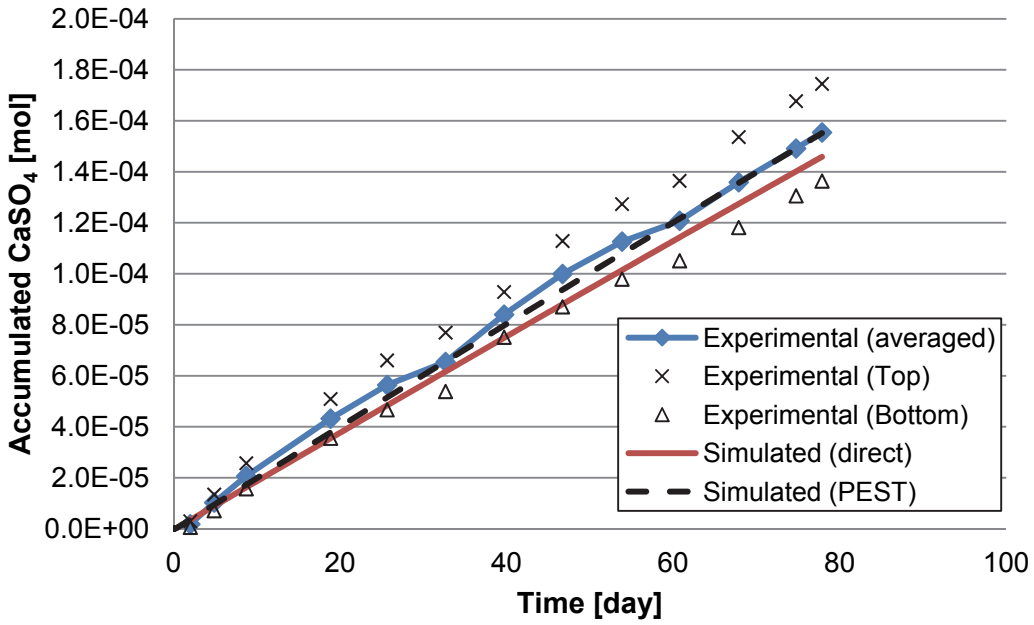

Figure 11: Comparison of Simulated and Experimental Average of the Accumulated $CaSO_4$ Mass in the Top and Bottom Reservoirs, Blue Line With Symbols – Experimental Data, Red Line – Simulated Results Using The Calibrated Effective Porosity and Tortuosity from B2.1, Black Dashed Line – Simulated Results using MIN3P-THCm and Parameter Optimization using PEST, Symbols Depict Actual Experimental Data in Top and Bottom Reservoirs

Table 19: Experimental Data and Simulated Results for the Average of the Accumulated Ca^{2+} Mass in the Top and Bottom Reservoirs for Case B2.2a

Time [day]	Experimental [mol][1]			Simulated [mol]	
	Top	Bottom	Averaged	Averaged	Residual[1]
0.00	-2.06×10^{-5}	-	-2.06×10^{-5}		
0.05	-6.90×10^{-6}	-5.23×10^{-6}	-6.07×10^{-6}		
0.63	-4.50×10^{-6}	-3.76×10^{-6}	-4.13×10^{-6}		
2.00	2.95×10^{-6}	5.70×10^{-7}	1.76×10^{-6}	3.57×10^{-6}	-1.81×10^{-6}
4.87	1.34×10^{-5}	7.10×10^{-6}	1.03×10^{-5}	9.41×10^{-6}	8.61×10^{-7}
8.72	2.57×10^{-5}	1.57×10^{-5}	2.07×10^{-5}	1.72×10^{-5}	3.46×10^{-6}
18.85	5.09×10^{-5}	3.55×10^{-5}	4.32×10^{-5}	3.77×10^{-5}	5.41×10^{-6}
25.64	6.60×10^{-5}	4.66×10^{-5}	5.63×10^{-5}	5.14×10^{-5}	4.87×10^{-6}
32.66	7.69×10^{-5}	5.38×10^{-5}	6.54×10^{-5}	6.56×10^{-5}	-2.15×10^{-7}
39.69	9.28×10^{-5}	7.51×10^{-5}	8.40×10^{-5}	7.97×10^{-5}	2.96×10^{-6}
46.70	1.13×10^{-4}	8.70×10^{-5}	9.99×10^{-5}	9.52×10^{-5}	4.27×10^{-6}
53.85	1.27×10^{-4}	9.79×10^{-5}	1.13×10^{-4}	1.08×10^{-4}	4.68×10^{-6}
60.76	1.36×10^{-4}	1.05×10^{-4}	1.21×10^{-4}	1.22×10^{-4}	-8.37×10^{-7}
67.86	1.54×10^{-4}	1.18×10^{-4}	1.36×10^{-4}	1.36×10^{-4}	-2.93×10^{-7}
74.75	1.68×10^{-4}	1.31×10^{-4}	1.49×10^{-4}	1.49×10^{-4}	-6.01×10^{-8}
77.87	1.74×10^{-4}	1.36×10^{-4}	1.55×10^{-4}	1.55×10^{-4}	-2.66×10^{-7}
Correlation coefficient				0.999	
Estimated parameters				**Value**	**95% confidence limits**
Effective porosity				0.062	$7.96\times10^{-3} – 4.82\times10^{-1}$
Tortuosity				0.093	$1.20\times10^{-2} – 0.72$
Calculated parameters					
D_e for Ca^{2+} in [m^2 s^{-1}]				$4.57x10^{-12}$	
D_e for SO_4^{2-} in [m^2 s^{-1}]				$6.14x10^{-12}$	

[1] The negative concentration values are calculated based on a calibrated function of concentration and the measured electrical conductivity. Negative values are excluded from the simulations.

Figure 11 shows that the simulation using diffusion coefficients directly from the through-diffusion experiment leads to slightly lower accumulated $CaSO_4$ mass than the experimental data. The reason for the difference lies in the slightly lower dry bulk density of 1.34 kg m^{-3} for B2.2a (experimental data listed in Table 17) instead of 1.40 kg m^{-3} for the B2.1 bentonite sample.

With the aid of PEST and MIN3P-THCm, the diffusion parameters for the benchmark B2.2a can be optimized (Table 19). The effective diffusion coefficient of Ca^{2+} is $4.57x10^{-12}$ m^2 s^{-1}, slightly higher than the previously calibrated value ($4.29x10^{-12}$ m^2 s^{-1}) in benchmark 2.1 (see Table 18). Using these optimized diffusion coefficients, better agreement between the simulated and experimental results is achieved (Figure 11). However, the actual experimental results show

different accumulated $CaSO_4$ in the top and bottom reservoirs (Figure 12). Therefore, further improvements to the conceptual model are needed to account for the observed discrepancies.

6.2.3.2 Simulation of the experiment

For the previous simulations, it was assumed that the top and bottom montmorillonite layer thicknesses were equal (i.e., 2.5 mm); however, this assumption produced a symmetric model that generated identical accumulated $CaSO_4$ mass results for the top and bottom reservoirs. The experimental results showed that the accumulated amount of $CaSO_4$ in the reservoir adjacent to the upper montmorillonite layer was higher by approximately 20% than that in the reservoir adjacent to the bottom layer. To reproduce the differences observed in mass accumulation it was hypothesized that the thicknesses of the two montmorillonite layers differed slightly. By changing the thickness to 2.3 mm for the top layer and 2.7 mm for the bottom layer, the simulation results shown in Figure 12 were obtained. The comparison of the experimental and simulated results for Ca^{2+} in the reservoirs showed very good agreement for the top and bottom reservoirs. But the difference of the thickness of the top and bottom bentonite layers is 0.4 mm (8% deviation to the designed thickness), which is relatively high. Therefore, there might be additional factors causing the difference in measured concentrations in both reservoir solutions, for example, diffusion parameters may differ between layers resulting from the disturbance during the sandwiching and re-compression process (Birgersson et al. 2009). Similar to Benchmark 2.1, the large confidence intervals for effective porosity and tortuosity are due to the interdependency of these parameters under quasi-steady state conditions.

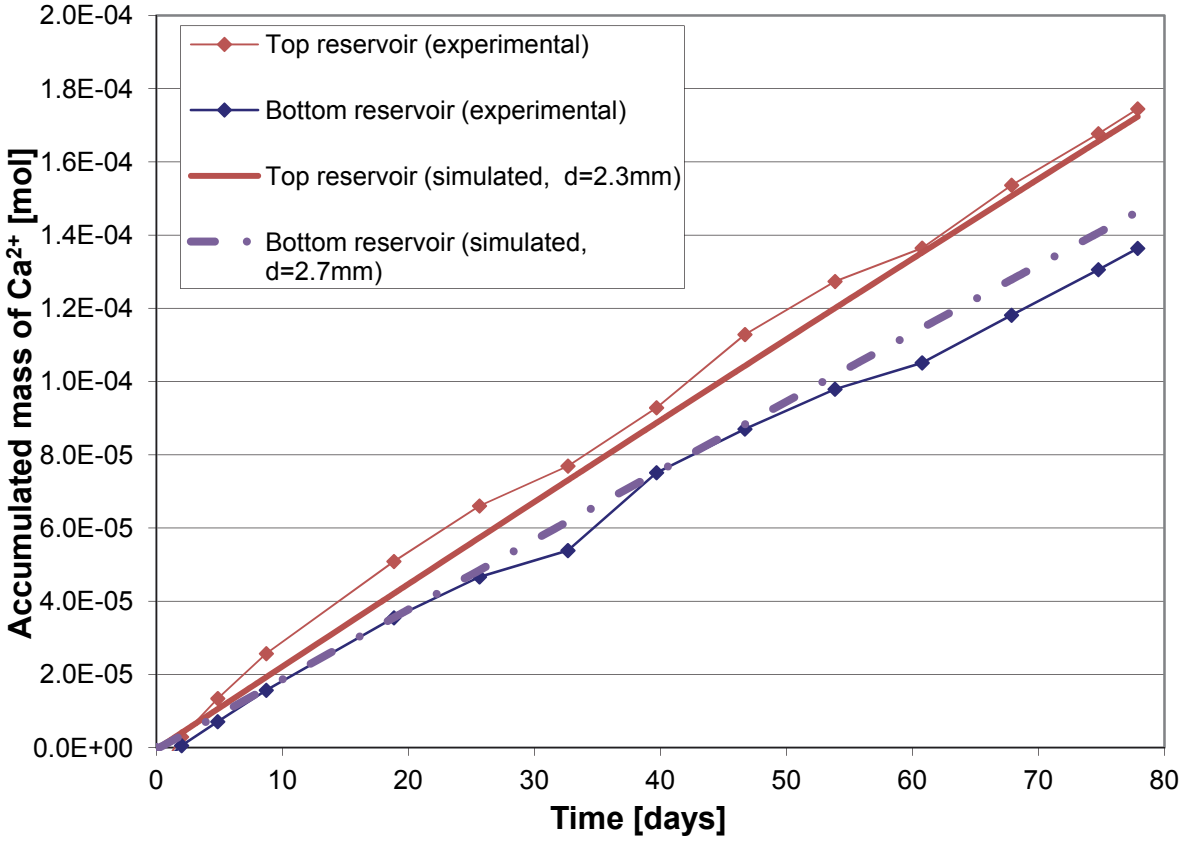

Figure 12: Comparison of Experimental and Simulated Accumulated Ca^{2+} Mass in the Top (Red) and Bottom (Blue) Reservoirs for Case B2.2a (in the Legend, d Refers to the Thickness of the Montmorillonite Layer). To Reproduce the Different Rates of Mass Accumulation in the Top and Bottom Reservoirs during the Experiments, It Was Assumed that the Two Montmorillonite Layers Have Different Thicknesses

6.3 CASE B2.2B: GYPSUM DISSOLUTION, DIFFUSION AND ION EXCHANGE IN NA-MONTMORILLONITE

6.3.1 Description of Experiment

The procedure for this experiment was the same as for experiment B2.2a (Section 6.2). The only difference is the use of Na-montmorillonite instead of Ca-montmorillonite, which results in ion exchange during Ca^{2+} diffusion through the Na-montmorillonite. The Na^{+} that is initially adsorbed on the montmorillonite is partially replaced by Ca^{2+} and enters into the porewater solution, which results in an increase of the local Na^{+} concentration. Consequently, both Na^{+} and Ca^{2+} diffuse towards the top and bottom reservoirs.

6.3.2 Model Setup and Material Properties

Similar to the simulation of Case B2.2a as described in section 6.2.2 and depicted in Figure 9, a 1D numerical analysis of reactive transport processes was undertaken, but with the additional consideration of ion exchange (Appelo 2005):

$$Ca^{2+} + 2\ Na\text{-}X \leftrightarrow Ca\text{-}X_2 + 2\ Na^{+} \quad \log K = 0.7959 \qquad \textbf{(6-4)}$$

According to this equation, the absorption of 1 mol Ca^{2+} results in 2 mol Na^{+} in the porewater.

Numerical analysis was undertaken with MIN3P-THCm and PEST, and the effective porosity and tortuosity were adjusted based on the observed concentration evolution of Ca^{2+} and Na^{+} in the top and bottom reservoirs. In the simulation, the surface-controlled kinetic reaction of gypsum (see section 6.2.2), ion exchange, and multicomponent diffusion processes are considered. The cation exchange capacity (CEC) of the Na-bentonite of 92 meq $(100\ g\ soil)^{-1}$ (Birgersson et al. 2009) is used. The free aqueous diffusion coefficients of all components are as listed in Table 3.

6.3.3 Simulation Results

A comparison of the numerical results and the experimental observations is shown in Table 20 and Figure 13. The estimated effective porosity is 0.089, and the effective tortuosity is 0.055 (Table 20). Large confidence limits are again due to the interdependency of these parameters under quasi-steady state conditions. There is a slight difference between the measured rate of $CaSO_4$ and Na_2SO_4 mass accumulation in the top and bottom reservoirs. The accumulated Na_2SO_4 mass can be reasonably reproduced by changing the thickness of the montmorillonite layers to 2.55 mm (top) and 2.45 mm (bottom) (Figure 13 left). However, the comparison of simulated and experimental $CaSO_4$ mass (Figure 13 right) does not agree as well, especially in the bottom reservoir.

Simulated spatial Ca^{2+} and Na^{+} concentration distributions across the Na-montmorillonite sample and the gypsum mineral volume fraction at the end of the experiment (40.6 days) are shown in Figure 14. Gypsum, which is located in the middle of the sample, dissolves. Dissolved Ca^{2+} diffuses away from the gypsum layer through the Na-montmorillonite and is attenuated by ion exchange with Na^{+} (Figure 14 right). This causes the concentration of Na^{+} to be much higher than that of Ca^{2+} (Figure 14 left), especially in the top and bottom reservoirs (see also experimental results shown in Figure 13).

Table 20: Experimental Data and Simulated Results for the Accumulated $CaSO_4$ and Na_2SO_4 Mass in [mol] for Case B2.2b

Time [day]	Accumulated $CaSO_4$ at top reservoir			Accumulated Na_2SO_4 at top reservoir		
	Experimental	Simulated	Residual	Experimental	Simulated	Residual
2.66	7.72×10^{-9}	4.12×10^{-9}	3.60×10^{-9}	2.92×10^{-5}	5.00×10^{-5}	-2.08×10^{-5}
3.88	3.24×10^{-9}	8.92×10^{-9}	-5.68×10^{-9}	5.60×10^{-5}	7.24×10^{-5}	-1.64×10^{-5}
4.80	4.40×10^{-8}	1.37×10^{-8}	3.04×10^{-8}	1.07×10^{-4}	8.88×10^{-5}	1.82×10^{-5}
5.75	3.39×10^{-8}	1.93×10^{-8}	1.46×10^{-8}	9.13×10^{-5}	1.05×10^{-4}	-1.36×10^{-5}
6.80	2.64×10^{-7}	2.67×10^{-8}	2.37×10^{-7}	1.11×10^{-4}	1.22×10^{-4}	-1.13×10^{-5}
9.64	9.63×10^{-8}	5.11×10^{-8}	4.52×10^{-8}	1.57×10^{-4}	1.67×10^{-4}	-9.62×10^{-6}
11.65	1.85×10^{-7}	7.21×10^{-8}	1.12×10^{-7}	1.96×10^{-4}	1.96×10^{-4}	-3.80×10^{-9}
13.66	2.21×10^{-7}	9.58×10^{-8}	1.26×10^{-7}	2.15×10^{-4}	2.24×10^{-4}	-9.17×10^{-6}
16.69	2.84×10^{-7}	1.36×10^{-7}	1.48×10^{-7}	2.50×10^{-4}	2.64×10^{-4}	-1.42×10^{-5}
23.82	2.96×10^{-7}	2.47×10^{-7}	4.90×10^{-8}	3.53×10^{-4}	3.50×10^{-4}	2.79×10^{-6}
30.70	4.89×10^{-7}	3.71×10^{-7}	1.17×10^{-7}	4.18×10^{-4}	4.25×10^{-4}	-6.64×10^{-6}
40.64	7.00×10^{-7}	5.78×10^{-7}	1.22×10^{-7}	5.03×10^{-4}	5.22×10^{-4}	-1.90×10^{-5}
Time [day]	**Accumulated $CaSO_4$ at bottom reservoir**			**Accumulated Na_2SO_4 at bottom reservoir**		
	Experimental	**Simulated**	**Residual**	**Experimental**	**Simulated**	**Residual**
2.66	1.61×10^{-9}	4.43×10^{-9}	-2.82×10^{-9}	3.57×10^{-5}	5.17×10^{-5}	-1.60×10^{-5}
3.88	1.76×10^{-9}	9.58×10^{-9}	-7.82×10^{-9}	5.83×10^{-5}	7.49×10^{-5}	-1.66×10^{-5}
4.80	8.43×10^{-9}	1.47×10^{-8}	-6.22×10^{-9}	1.07×10^{-4}	9.19×10^{-5}	1.51×10^{-5}
5.75	7.08×10^{-9}	2.07×10^{-8}	-1.36×10^{-8}	9.90×10^{-5}	1.08×10^{-4}	-9.48×10^{-6}
6.80	1.03×10^{-7}	2.86×10^{-8}	7.44×10^{-8}	1.21×10^{-4}	1.26×10^{-4}	-5.44×10^{-6}
9.64	8.13×10^{-8}	5.48×10^{-8}	2.65×10^{-8}	1.73×10^{-4}	1.72×10^{-4}	8.67×10^{-7}
11.65	2.06×10^{-7}	7.73×10^{-8}	1.29×10^{-7}	2.16×10^{-4}	2.02×10^{-4}	1.35×10^{-5}
13.66	1.49×10^{-7}	1.03×10^{-7}	4.63×10^{-8}	2.37×10^{-4}	2.31×10^{-4}	5.50×10^{-6}
16.69	3.79×10^{-7}	1.45×10^{-7}	2.34×10^{-7}	2.72×10^{-4}	2.73×10^{-4}	-8.27×10^{-7}
23.82	2.12×10^{-7}	2.64×10^{-7}	-5.20×10^{-8}	3.85×10^{-4}	3.61×10^{-4}	2.36×10^{-5}
30.70	2.80×10^{-7}	3.98×10^{-7}	-1.18×10^{-7}	4.57×10^{-4}	4.38×10^{-4}	1.89×10^{-5}
40.64	2.80×10^{-7}	6.20×10^{-7}	-3.40×10^{-7}	5.45×10^{-4}	5.38×10^{-4}	6.74×10^{-6}
Correlation coefficient					0.998	
Estimated parameters				**Value**	**95% confidence limits**	
Effective porosity				8.93×10^{-2}	1.18×10^{-2} – 0.67	
Tortuosity				5.54×10^{-2}	5.85×10^{-3} – 0.523	
Calculated parameters						
D_e for Ca^{2+} in [m^2 s^{-1}]				3.91×10^{-12}		
D_e for Na^+ in [m^2 s^{-1}]				6.59×10^{-12}		
D_e for SO_4^{2-} in [m^2 s^{-1}]				5.26×10^{-12}		

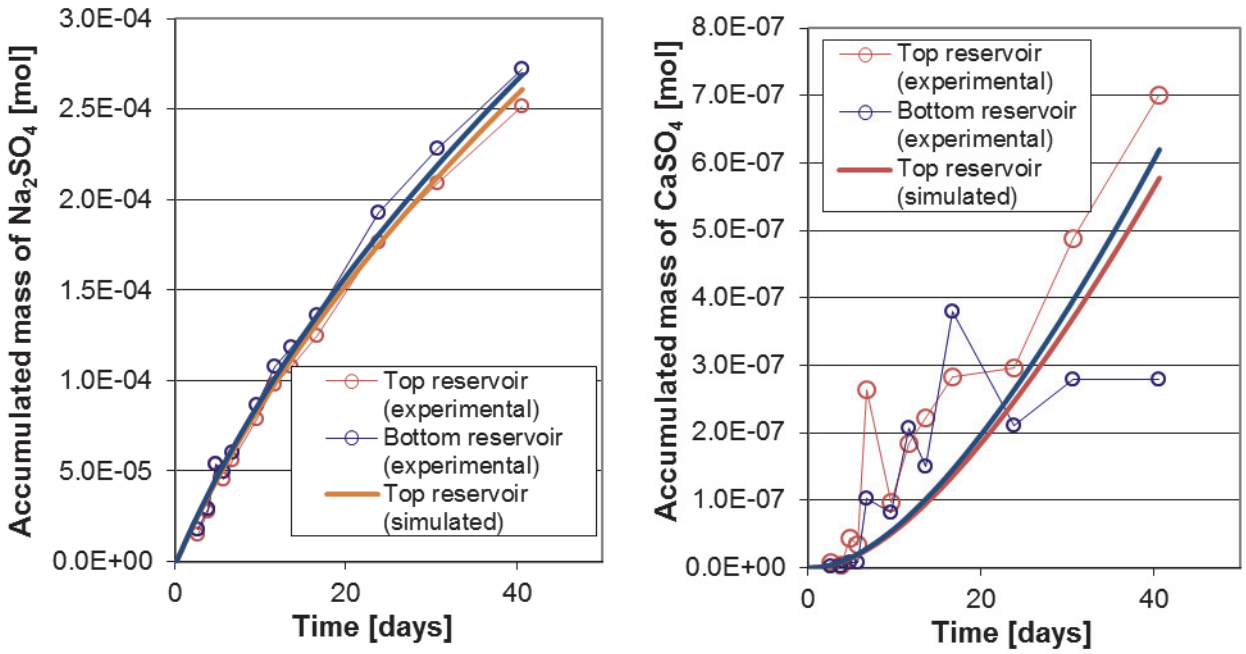

Figure 13: Comparison of Simulated and Experimental Accumulated Na_2SO_4 Mass (Left) and $CaSO_4$ Mass (Right) in the Top and Bottom Reservoirs

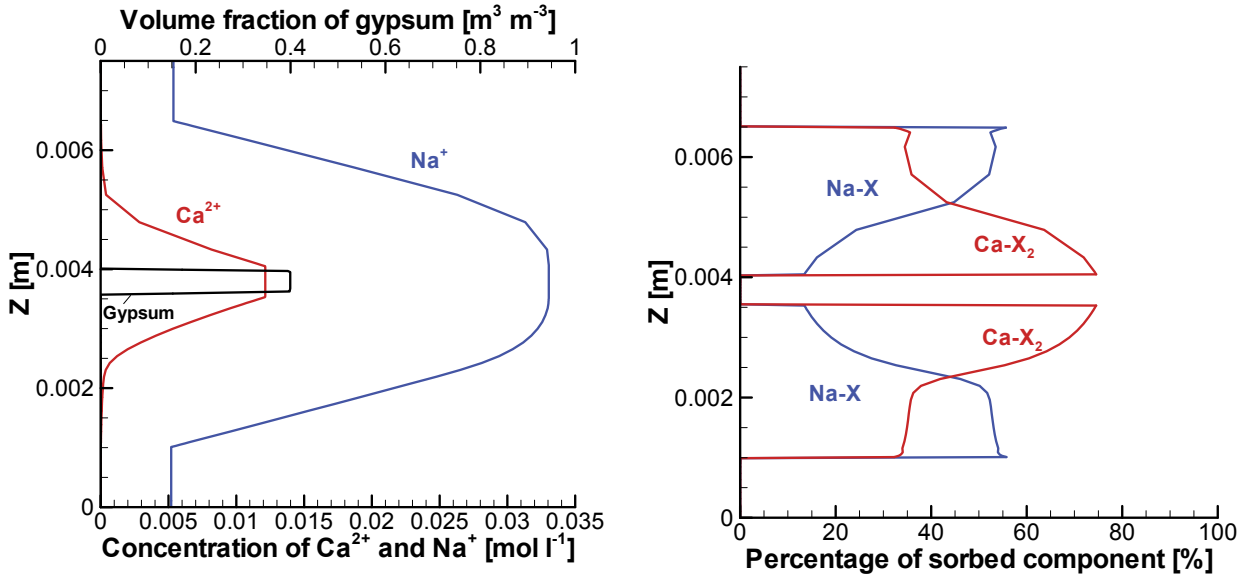

Figure 14: Numerical Simulation Results at 40.6 Days: Left – Profiles of Aqueous Ca^{2+} (Red) and Na^+ (Blue) Concentration and Gypsum Volume Fraction (Black); Right – Equivalent Fractions of Ion-exchanged Species Reported as Percentages

6.4 SUMMARY AND DISCUSSION

Simulation results obtained using MIN3P-THCm were compared to observational data from the Benchmark II experiments for the three experiments with increasing complexity. The calibrated diffusion parameters are summarized in Table 21. Although the geochemical processes of the three experiments are very different, the calibrated effective diffusion coefficients for Ca^{2+} or SO_4^{2-} of all experiments are fairly close, and decrease with increasing bulk density. Slight differences in the diffusion parameters are attributed to the different bentonite types, reflected in variations of calibrated effective porosity or tortuosity values. For the binary chemical system (e.g. B2.1 and B2.2a), the diffusive transport mechanisms controlling the fluxes of Ca^{2+} and SO_4^{2-} simulated by MIN3P-THCm using the MCD formulation are equal, even though their effective diffusion coefficients differ. This is due to the electrochemical coupling, which tightly links the transport of the anions and cations, and maintains local charge balance. Because the ions in the solution consist of only one cation (Ca^{2+}) and one anion (SO_4^{2-}), local charge balance can only be maintained when both ions move at the same rate. Theoretically, the apparent D_e for both ions should be equivalent to the averaged D_e of both ions as listed in Table 21. For a solution system including more than two ions (e.g. B2.2b), the situation will be more complicated depending on the type of ions and their concentrations. Nevertheless, the total flux of negative charge should be equal to the total flux of positive change.

Table 21: Summary of Calibrated Diffusion Parameters for Benchmark II

Case	B2.1	B2.2a	B2.2b
Soil type (initial)	Ca-Montmorillonite	Ca-Montmorillonite	Na-Montmorillonite
Processes	Diffusion	Dissolution, diffusion	Dissolution, diffusion and ion exchange
Dry bulk density [g cm^{-3}]	1.40	1.34	1.46
Diffusion parameters			
Effective porosity	0.0520	0.0600	0.0893
Effective tortuosity	0.104	0.0978	0.0554
D_e for Ca^{2+} [m^2 s^{-1}]	4.29×10^{-12}	4.65×10^{-12}	3.91×10^{-12}
D_e for SO_4^{2-} [m^2 s^{-1}]	5.77×10^{-12}	6.25×10^{-12}	5.26×10^{-12}
D_e for Na^+ [m^2 s^{-1}]	-	-	6.59×10^{-12}

Direct comparison with other modelling groups is not possible because there are no simulation results currently available using a similar modelling approach. The reported results by Birgersson et al. (2009) were calculated based on the experimental flux at steady state ($\boldsymbol{j_{s,s}}$) according to the following equation:

$$\boldsymbol{D_e = -\frac{j_{s,s}}{\nabla c}} \qquad \textbf{(6-5)}$$

The calculated D_e values for $CaSO_4$ are $2.9x10^{-12}$ m^2 s^{-1} for Case B2.1, $1.7x10^{-12}$ m^2 s^{-1} for Case B2.2a, and the D_e value for Na_2SO_4 is $7.2x10^{-12}$ m^2 s^{-1} for Case B2.2b. This method is a direct evaluation of the experimental results using a simple parameter (D_e) without taking into consideration the geochemical processes that are taking place in the experiment. Nevertheless, the diffusion coefficients obtained by Birgersson are fairly close to our optimized effective diffusion coefficients.

7. BENCHMARK III: ION EXCHANGE

Benchmark III includes a set of Na/Ca and Ca/Na ion exchange experiments using compacted (initially) homo-ionic Na- and Ca-montmorillonite at different dry densities (Birgersson 2011).

7.1 DESCRIPTION OF EXPERIMENT

Montmorillonite samples were compacted in a stainless steel cell (35 mm in diameter and 5 mm in thickness), to designed dry density, and placed in the apparatus shown in Figure 15 (Birgersson 2011). Water saturation of the samples was realized by circulating 0.1 L of de-ionized water through the titanium filters located on the top and bottom of the sample (Birgersson 2011). When the measured swelling pressure was stable, full saturation was assumed to have been reached and the ion exchange experiment was started by replacing the de-ionized water with a solution of a specified chemical composition. $CaCl_2$ solutions were used for all experiments using Na-montmorillonite (Case B3.1 – Case B3.3), while NaCl solutions were utilized for experiments using Ca-montmorillonite (Cases B3.4 – B3.6). An overview of the six test cases is presented in Table 22. For each experiment, three solutions of increasing concentration were successively replenished in three phases when exchange equilibrium was reached (Figure 16 and Figure 17). Phase I lasts from the beginning until 25.4 days, followed by Phase II continuing until 74.3 days, and completed by Phase III terminating at 109.9 days (see the red vertical dashed lines in Figure 16 and Figure 17). The design cation concentrations to be added to the solutions corresponded to approximately 25%, 50% and 100% of the total cation exchange capacity (CEC) in the test samples (Table 22). As the dry densities of the samples for Cases B3.1 to B3.3 and B3.4 to B3.6 increase, the cation concentrations to be added increased as well. Reference solutions with known cation concentrations were maintained parallel with the experiments. Regular measurements of the potentials in the reference solutions were conducted using ion selective electrodes for either Ca^{2+} or Na^{+}. These reference measurements were used to calculate the concentrations of both cations Ca^{2+} and Na^{+} based on potential measurements in the experiments, as shown in Figure 16 and Figure 17 (Birgersson et al. 2009; Birgersson 2011).

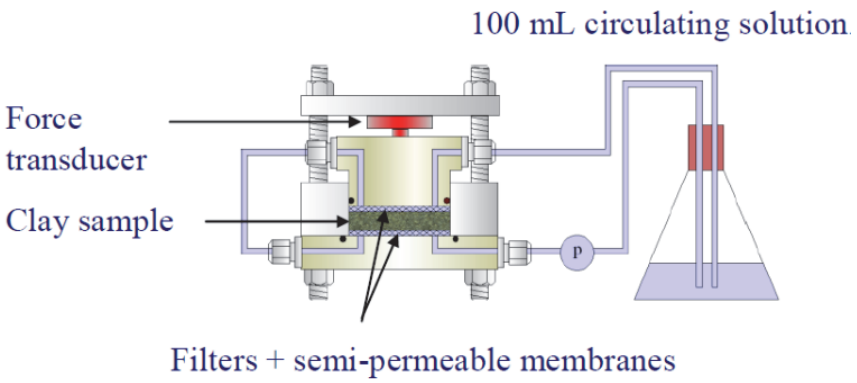

Figure 15: Schematic Design of the Experimental Setup for Benchmark III (Birgersson et al. 2009)

Table 22: Experimental Cases, Montmorillonite Sample Properties and the Design Amount of Added Cations in the Reservoir (Based on Birgersson 2011)

Case	Initial bentonite type	Dry density	Porosity	Added cation	Total mass of cations added in the reservoir		
		[g cm^{-3}]	[-]		Phase 1 [mmol]	Phase 2 [mmol]	Phase 3 [mmol]
B3.1	Na-montmorillonite	1.021	0.629	Ca^{2+}	0.57	1.13	2.26
B3.2	Na-montmorillonite	1.414	0.585	Ca^{2+}	0.78	1.56	3.13
B3.3	Na-montmorillonite	1.729	0.371	Ca^{2+}	0.96	1.91	3.83
B3.4	Ca-montmorillonite	1.021	0.629	Na^{+}	1.13	2.26	4.52
B3.5	Ca-montmorillonite	1.414	0.585	Na^{+}	1.56	3.13	6.26
B3.6	Ca-montmorillonite	1.729	0.371	Na^{+}	1.91	3.83	7.65

Figure 16 depicts the experimental results for Na-montmorillonite (Case B3.1-Case B3.3). It is important to note that in order to maintain mass balance of Ca^{2+}, the design concentrations for Ca^{2+} in the reservoir (Table 22) were used to redefine initial conditions at the time of solution exchange as depicted in Figure 16, following the suggestion by the experimental group (see Table 24 and Figure 16 top). The concentrations of Ca^{2+} in the reservoir for Cases B3.1 to B3.3 decrease after each solution exchange. At the same time, the Na^{+} concentrations increase gradually as the result of ion exchange. Comparison of the Ca^{2+} concentration evolutions for Cases B3.1 to B3.3 showed that there are sudden concentration increases at 24.27 days for Cases B3.1 and B3.2, but not for Case B3.3, which has been captured in the corresponding simulations.

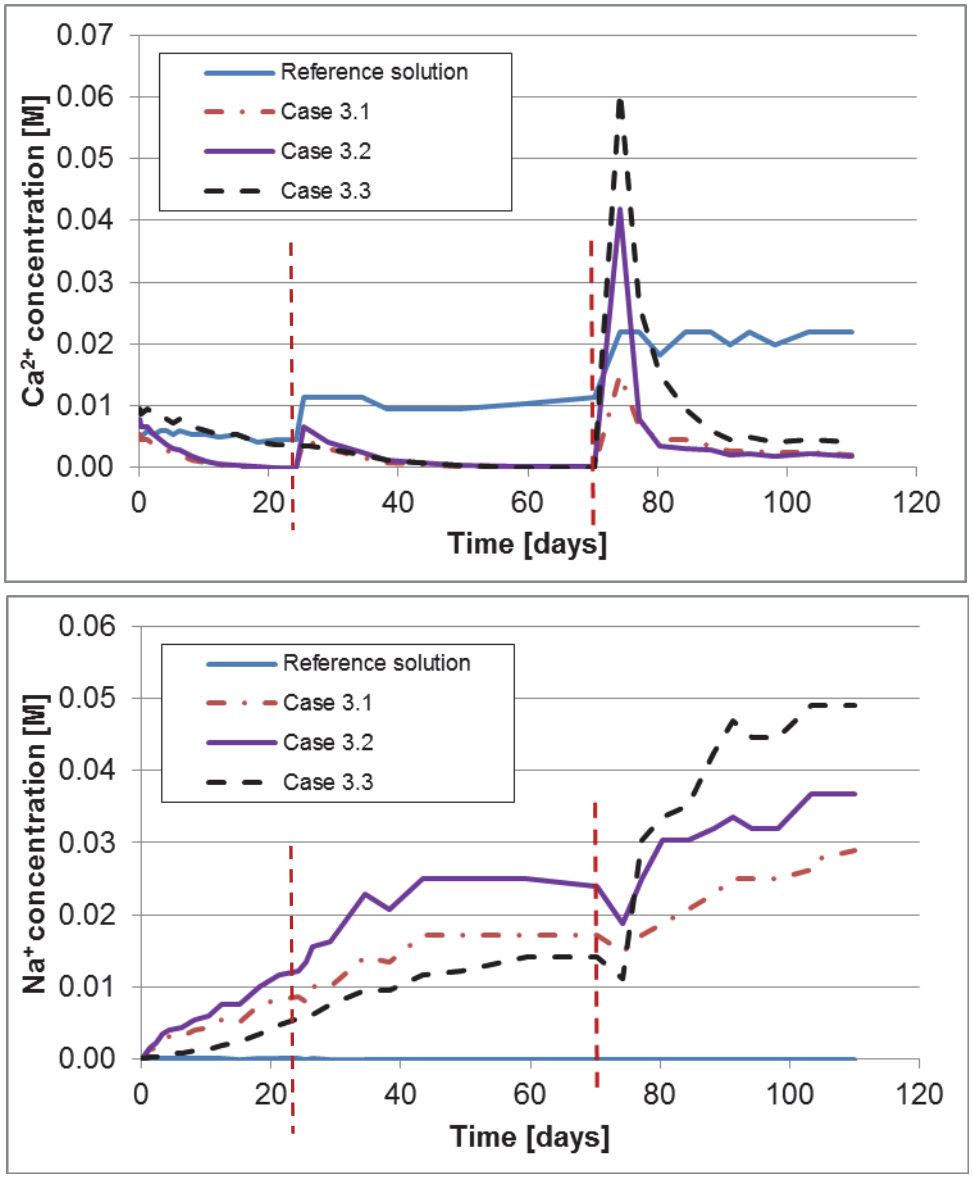

Figure 16: Experimental Concentrations of Ca^{2+} and Na^{+} in the Reservoir Calculated from Solution Potentials Measured by Ion Selective Electrodes for Benchmark III Case B3.1, Case B3.2, Case B3.3 and the Reference Solution (Based on Birgersson et al. 2009 and Birgersson 2011 with Modifications Described in Table 24) (the vertical Red Dashed Lines Depict the Time When the Experimental Phases Change)

Figure 17 depicts the results of the experiments on Ca-montmorillonite (Cases B3.4 to B3.6). In the reference solution, the concentration of Na^{+} did not show any decrease, while the concentration of Ca^{2+} remains very small (on the order of 10^{-6} mol L^{-1}). The concentrations of Na^{+} decrease after the first two solution exchanges (Cases B3.4 to B3.6), with a less obvious response after the third exchange. At the same time, the Ca^{2+} concentrations increase gradually as the result of ion exchange.

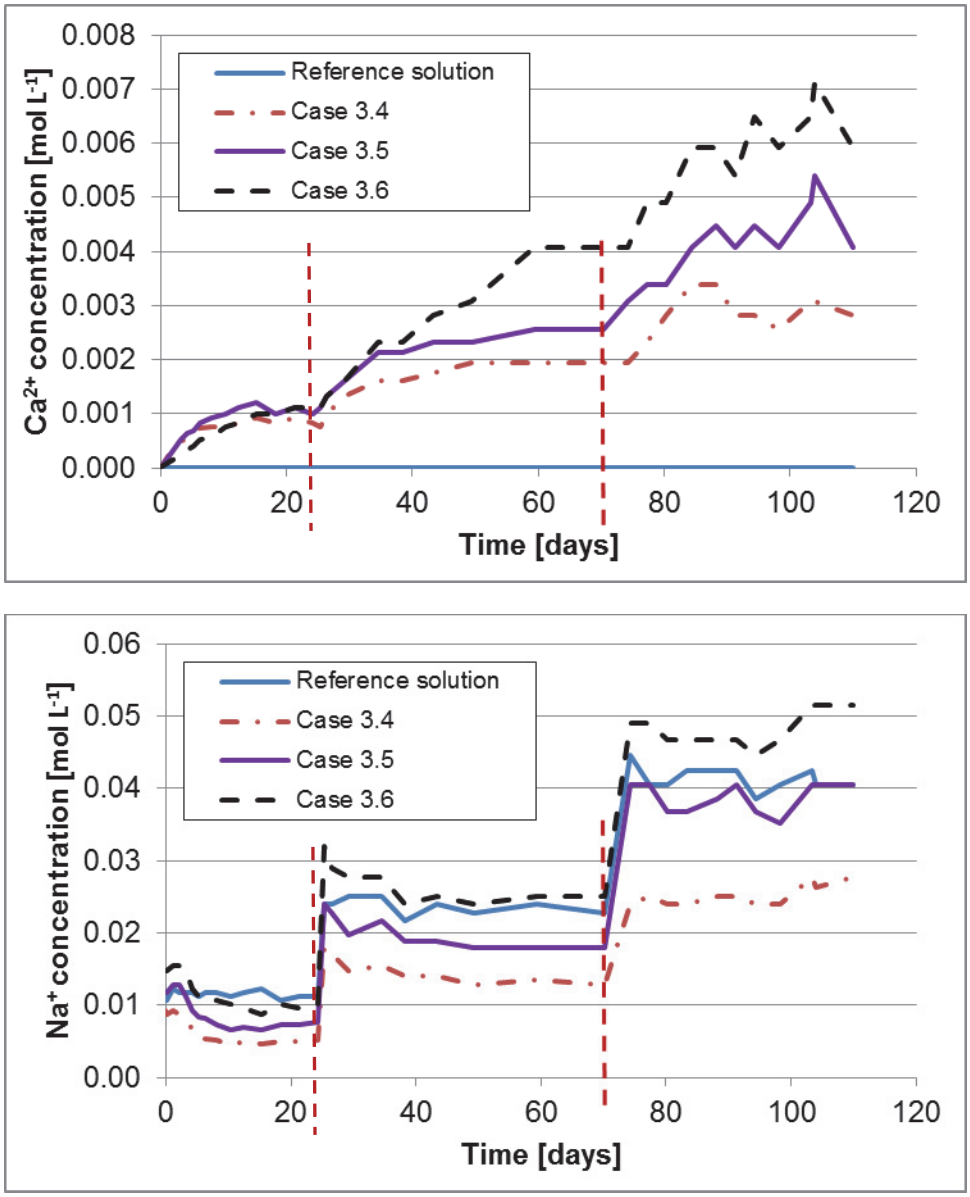

Figure 17: Experimental Concentrations of Ca^{2+} and Na^{+} in the Reservoir Calculated from Solution Potentials Measured by Ion Selective Electrodes for Benchmark III Case B3.4, Case B3.5, Case B3.6 and the Reference Solution (Based on Birgersson et al. 2009 and Birgersson 2011 with Modifications Described in Table 24) (the vertical Red Dashed Lines Depict the Time When the Experiment Phase Changes)

7.2 ANALYSIS OF EXPERIMENTAL DATA

The mass balance for Ca^{2+} and Na^{+} during the ion exchange experiments is analysed in this section based on the assumption that diffusion and Ca/Na ion exchange are the only relevant processes. In other words, the decrease of the added cations in the reservoir was assumed solely due to ion exchange reactions as defined in equation (6-4). The cumulative concentration decrease of added cations (i.e., Ca^{2+} in Cases B3.1-3.3, Na^{+} in Cases B3.4-3.6) in the 0.1 L reservoir corresponds to the integrated concentration change during each experimental phase and was calculated using the following equation:

$$\Delta C_{tot}^{aq} = \sum_{i=1}^{N} \left(C_{i,b}^{aq} - C_{i,end}^{aq} \right) \qquad N = 2 \text{ or } 3 \qquad \textbf{(7-1)}$$

in which, ΔC_{tot}^{aq} stands for the cumulative concentration decrease, N is the number of phases (equals to 2 for Case B3.3, 3 for other cases), $C_{i,b}^{aq}$ is the aqueous concentration at the beginning of each experimental phase, $C_{i,end}^{aq}$ is the aqueous concentration at the end of each experimental phase.

The cumulative concentration increase of cations on the exchanger (i.e. Na^+ in Cases B3.1-3.3, Ca^{2+} in Cases B3.4-3.6) was calculated by the difference between the final and initial concentrations of each experiment (i.e. in practice the final concentration was used because the concentrations of the cation of interest was negligible at the beginning of each experiment) (Table 23 and Table 25).

The maximum sorption potential of the montmorillonite samples was calculated based on the CEC value of 92 meq (100 g soil)$^{-1}$ multiplied by the mass of the sample.

The initial and final concentrations of Ca^{2+} and Na^+ in each phase together with the calculated values are listed in four tables: Table 23 and Table 24 for the benchmarks B3.1, B3.2, and B3.3 on Na-montmorillonite, Table 25 and Table 26 for the benchmarks B3.4, B3.5, and B3.6 on Ca-montmorillonite. Theoretically, Na^+ concentrations at the beginning of the experiments with Na-montmorillonite should be negligible. However, the measured potential obtained by the ion selective electrode for Na^+ showed a small value leading to the initial concentration as listed in Table 23 (Birgersson 2011). The same is also valid for the experiments with Ca-montmorillonite (Table 26).

Table 23: Mass Balance Calculations for Modified Composition: Mass Balance Calculations for Na^+ for Experiments with Na-montmorillonite (Birgersson 2011)

Phase	**Time**	**Concentration of Na^+ in the reservoir solution [mol L^{-1}]**			**Remarks**
	[days]	**B3.1**	**B3.2**	**B3.3**	
Phase I	0.00	1.42×10^{-4}	6.30×10^{-5}	4.29×10^{-5}	Initial solution*
	24.27	8.75×10^{-3}	1.22×10^{-2}	5.69×10^{-3}	
Phase II	25.38	7.95×10^{-3}	1.35×10^{-2}	6.26×10^{-3}	Modified solution composition
	70.27	1.71×10^{-2}	2.39×10^{-2}	1.41×10^{-2}	
Phase III	74.27	1.48×10^{-2}	1.88×10^{-2}	1.11×10^{-2}	Modified solution composition
	109.94	2.90×10^{-2}	3.68×10^{-2}	4.91×10^{-2}	
Total increase of Na^+ concentration in the 0.1 L reservoir [mol L^{-1}]		0.029	0.0368	0.0491	
Total desorbed mass of Na^+ (**A**) [meq]		2.90	3.68	4.91	
Maximum Na^+ sorbed in the montmorillonite sample (**B**) [meq]		4.52	6.26	7.65	
Percentage (**A/B**)		70.7%	64.9%	67.3%	

* calculated value based on the measured potential by ion selective electrode for Na^+

The analyzed results of the experiments Cases B3.1-B3.3 showed that about 60-70% of the Na^+ on the Na-montmorillonite was replaced and diffused into the reservoir (Table 23). At the same time, however, Ca^{2+} sorbed onto the Na-montmorillonite through ion exchange amounts up to 94.5% - which is significantly higher (about 30%) than the desorbed amount of Na^+ in meq. This may imply that other processes than exchange of Na^+ with Ca^{2+} are playing a role in the experiments.

Table 24: Mass Balance Calculations for Ca^{2+} for Experiments with Na-montmorillonite after Modifications Based on Suggestions by the Research Team in Charge of the Experimental Work

Phase	Time	Concentration of Ca^{2+} in the reservoir solution [mol L^{-1}]			Remarks
	[days]	B3.1	B3.2	B3.3	
Phase I	0.00	5.65×10^{-3}	7.82×10^{-3}	9.57×10^{-3}	Initial solution, 25% CEC#
	24.27	1.05×10^{-5}	1.15×10^{-5}	-	
Phase II	25.38	5.66×10^{-3}	7.83×10^{-3}	-	Modified solution composition, 50% CEC*
	70.27	8.93×10^{-5}	1.08×10^{-4}	1.26×10^{-5}	
Phase III	74.27	1.14×10^{-2}	1.58×10^{-2}	2.87×10^{-2}	Modified solution composition, 100% CEC
	109.94	1.93×10^{-3}	1.76×10^{-3}	4.08×10^{-3}	
Total decrease of Ca^{2+} concentration in the 0.1 L reservoir [mol L^{-1}]		0.0207	0.0296	0.0342	
Total sorbed mass of Ca^{2+} (**A**) [meq]		4.14	5.92	6.84	
Maximum Ca^{2+} sorption potential on the montmorillonite sample (**B**) [meq]		4.52	6.26	7.65	
Percentage (**A/B**)		91.5%	94.5%	89.3%	

the initial concentration of Ca^{2+} was designed such that the molar mass of Ca^{2+} in the 100 ml reservoir solution is equivalent to 25% of the maximum sorption capacity of the bentonite sample according to its CEC. * Modification of solution by adding $CaCl_2$ such that the accumulated Ca^{2+} amount in the solution is equivalent to 50% of the maximum sorption capacity of the bentonite sample according to its CEC.

Similar analyses were undertaken for the experiments using Ca-montmorillonite. Table 25 shows that the total sorbed molar mass of Na^+ amounts only to 12% of the maximum Na^+ sorption potential for Cases B3.4 and B3.6, and to 16% for Case B3.5. Table 26 shows the total desorbed molar mass of Ca^{2+} amounts to between 12% and 19% of the maximum Ca^{2+} sorption potential of the samples, which is fairly close to those values for Na^+ (compare Table 25 and Table 26).

Table 25: Mass Balance Calculations for Na^+ for Experiments on Ca-montmorillonite

Phase	Time	Concentration of Na^+ in the reservoir solution [mol L^{-1}]			Remarks
	[days]	B3.4	B3.5	B3.6	
Phase I	0.00	9.18×10^{-3}	1.17×10^{-2}	1.48×10^{-2}	Initial solution
	24.23	5.17×10^{-3}	7.58×10^{-3}	1.01×10^{-2}	
Phase II	25.31	1.79×10^{-2}	2.39×10^{-2}	3.19×10^{-2}	Modified solution composition
	70.27	1.28×10^{-2}	1.79×10^{-2}	2.51×10^{-2}	
Phase III	74.27	2.39×10^{-2}	4.05×10^{-2}	4.91×10^{-2}	Modified solution composition
	109.94	2.76×10^{-2}	4.05×10^{-2}	5.15×10^{-2}	
Total decrease of Na^+ concentration [mol L^{-1}]		0.0054	0.0101	0.0091	
Total sorbed mass of Na^+ (**A**) [mmol]		0.54	1.01	0.91	
Maximum Na^+ sorption potential in the sample (**B**) [mmol]		4.52	6.26	7.65	
Percentage (**A/B**)		12.0%	16.1%	11.9%	

Table 26: Mass Balance Calculations for Ca^{2+} for Experiments with Ca-montmorillonite

Phase	Time	Concentration of Ca^{2+} in the reservoir solution [mol L^{-1}]			Remarks
	[days]	B3.4	B3.5	B3.6	
Phase I	0.00	3.42×10^{-6}	2.59×10^{-6}	1.96×10^{-6}	Initial solution*
	24.23	8.36×10^{-4}	1.01×10^{-3}	1.11×10^{-3}	
Phase II	25.31	7.62×10^{-4}	1.11×10^{-3}	1.11×10^{-3}	Modified solution composition
	70.27	1.93×10^{-3}	2.56×10^{-3}	4.08×10^{-3}	
Phase III	74.27	1.93×10^{-3}	3.08×10^{-3}	4.08×10^{-3}	Modified solution composition
	109.94	2.81×10^{-3}	4.08×10^{-3}	5.92×10^{-3}	
Total desorbed Ca^{2+} concentration [mol L^{-1}]		2.81×10^{-3}	4.08×10^{-3}	5.92×10^{-3}	
Total desorbed mass of Ca^{2+} (**A**) [meq]		0.56	0.82	1.18	
Maximum Ca^{2+} sorbed on the montmorillonite sample (**B**) [meq]		4.52	6.26	7.65	
Percentage (**A/B**)		12.4%	17.2%	18.6%	

* calculated value based on the measured potential by ion selective electrode for Na^+

7.3 MODEL SETUP AND MONTMORILLONITE MATERIAL PROPERTIES

Owing to the symmetric experimental conditions, a 1D model including top and bottom reservoirs, each with a 50 mL solution volume, was used (Figure 18). The thickness of the compacted montmorillonite is 5 mm, both target reservoirs are represented as 1 mm tall cells in the model. To accurately represent the 50 mL solution, a porosity (reservoir capacity) of 52.0 (for a sample diameter 35 mm) was specified for both reservoirs. A high tortuosity of 100 was specified for the reservoirs to mimic turbulent mixing within the reservoir due to circulation of the source and target solutions. It was assumed that solute transport in the experiments is diffusion dominated. The cation exchange capacity (CEC) of Na-montmorillonite is 92 meq $(100g)^{-1}$, while CEC for Ca-montmorillonite is 94 meq $(100g)^{-1}$. These values are based on post-experiment analyses of the actual samples (Birgersson 2011). In the simulations, a CEC value of 92 meq $(100g)^{-1}$ was used for both materials. Considering the difference to the actual value for Ca-montmorillonite is very small (about 2%), this deviation is deemed acceptable.

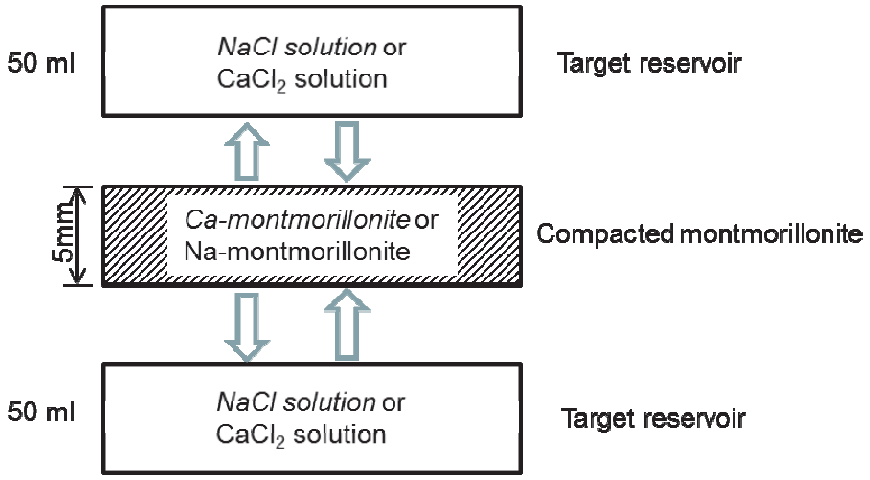

Figure 18: Model Setup for the Ion Exchange Experiments

Ion exchange reactions of $Na^+/Ca\text{-}X_2$ or $Ca^{2+}/Na\text{-}X$ were simulated based on equation (6-4). According to Karnland et al. (2011), the effective selectivity coefficients (Kc) for ion exchange reactions in compacted bentonite are different to those given in the literature (e.g. Appelo, 2005). The Kc values of each sample were determined using inductively coupled plasma atomic emission spectroscopy (ICP-AES) to determine the major ions in solution as well as on the solids after termination of each experiment (Table 27). The determined Kc values for Na-montmorillonite (Cases B3.1 – B3.3) are between 3.8 and 5.5, which are lower than the K value 6.25 as given in equation (6-4) according to the PHREEQC database (Appelo 2005); For experiments B3.4 to B3.6, the determined Kc values range between 6.7 and 7.8, and are higher than the PHREEQC database value (6.25). Nevertheless, all determined values are greater than 1.0, which means that Ca is preferred over Na to be sorbed onto montmorillonite. For the simulations in the following two subsections, the measured Kc coefficients were used.

Table 27: Measured Selectivity Coefficients (Kc) for Ca/Na According to the Gaines-Thomas Convention (Karnland et al. 2011)

Case	Sample	Kc [-]	Case	Sample	Kc [-]
B3.1	C WyNa 01	4.0	B3.4	C WyCa 04	6.7
B3.2	C WyNa 02	5.5	B3.5	C WyCa 05	7.8
B3.3	C WyNa 03	3.8	B3.6	C WyCa 06	7.0

MIN3P-THCm and PEST were applied to estimate the effective porosity and tortuosity. The 1D model was discretized into 89 control volumes. Both boundaries were set as no flux boundaries. The multicomponent diffusion model was adopted for all simulations. The D_0 values listed in Table 3 were applied (Lide 1994).

7.4 SIMULATION RESULTS FOR EXPERIMENTS ON NA-MONTMORILLONITE

7.4.1 Case B3.1

Simulations of Case B3.1 were undertaken in three phases corresponding to the sequential replacement of the solutions as shown in Table 22.

For Phase I, as Ca^{2+} in the reservoir solution diffuses into the Na-montmorillonite, part of the Ca^{2+} mass is adsorbed (Ca-X_2, Figure 19 left). Initially, Ca-X_2 is not present in the homo-ionic Na-montmorillonite. Consequently, the Na^+ concentration in the porewater increases as diffusion of Na^+ towards the reservoirs occurs. This causes the Ca^{2+} concentrations in the reservoir solution to decrease with time (Figure 20 left), while Na^+ concentrations increase (Figure 20 right). The best fit effective porosity and tortuosity for the first phase of the B3.1 experiment (Figure 20) were 0.13 and 0.08, respectively. The calculated effective diffusion coefficients for Ca^{2+}, Na^+ and Cl^- in the compacted Na-montmorillonite are listed in Table 28.

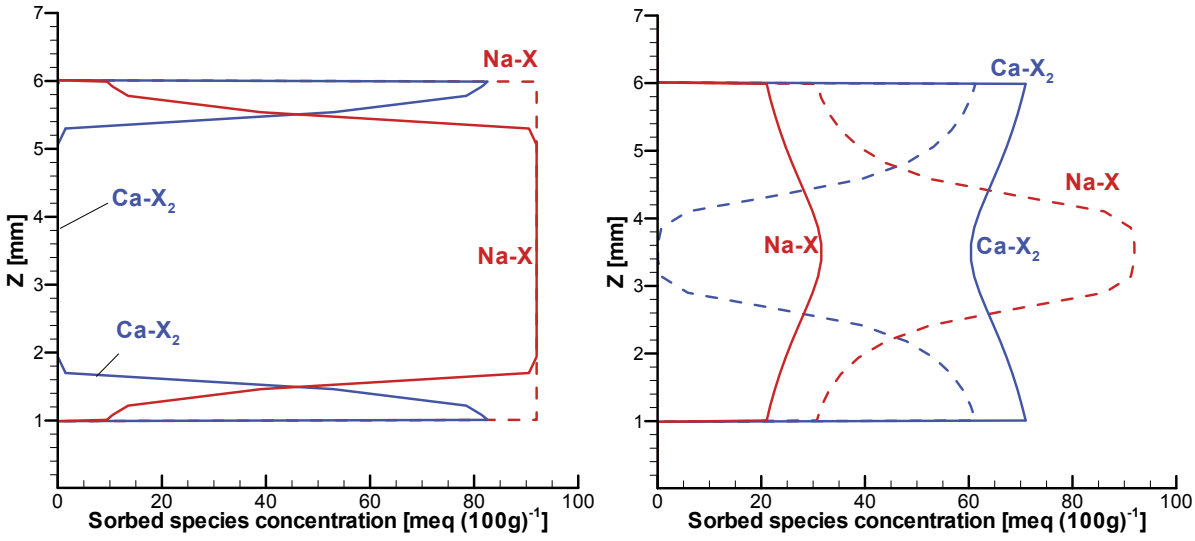

Figure 19: Simulated Concentrations of Sorbed Na-X (Red Lines) and Ca-X_2 (Blue Lines) at the Beginning (Dashed Lines) and the End (Solid Lines) of Phase I (Left) and Phase III (Right) for Benchmark III Case B3.1

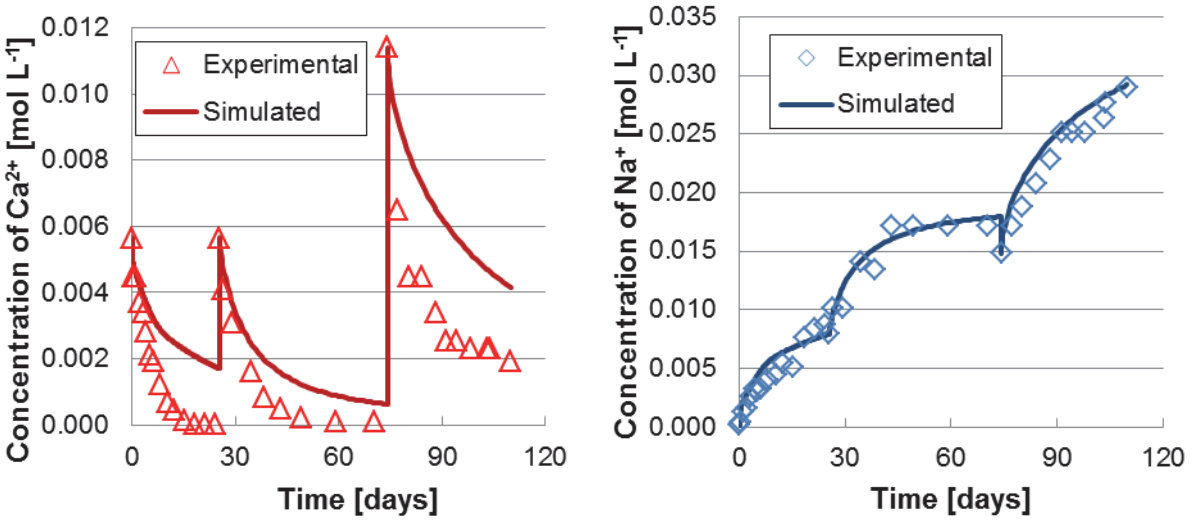

Figure 20: Comparison of Simulated and Experimental Concentrations for Ca^{2+} (Left) and Na^{+} (Right) in the Reservoir Solution for Benchmark III Experiment B3.1

Table 28: Estimated Diffusion Parameters in Na-Montmorillonite for Case B3.1

Phase	Effective porosity	Effective tortuosity	D_e [m^2 s^{-1}]		
			Ca^{2+}	Na^{+}	Cl^{-}
I	0.13	0.08	8.30×10^{-12}	1.40×10^{-11}	2.13×10^{-11}
II	0.15	0.37	4.45×10^{-11}	7.50×10^{-11}	1.14×10^{-10}
III	0.16	0.27	3.41×10^{-11}	5.75×10^{-11}	8.76×10^{-11}

Simulated Na^{+} concentrations in the reservoir agree well with the experimental data, but simulated Ca^{2+} concentrations in the reservoir generally exceed experimentally determined concentrations (Figure 20).

For Phase II (starting at 24.3 days, Figure 20), the $CaCl_2$ concentration in the reservoir solution was increased, and diffusion of Ca^{2+} into and Na^{+} out of the Na-montmorillonite sample continued. The best fit effective porosity and tortuosity for the second phase were 0.15 and 0.37, respectively (Table 28). These parameters differ substantially from those obtained in Phase I. The calculated effective diffusion coefficients (D_e) of each species are therefore different. D_e for Ca^{2+} for example is $4.45\text{x}10^{-11}$ m^2 s^{-1} (Phase II), higher than $D_e=8.30\text{x}10^{-12}$ m^2s^{-1} (Phase I). One possible explanation is that the material properties of Na-montmorillonite were affected by the ion exchange reactions, which was not considered in the simulation. The significant change is due to the increased tortuosity value during Phase II (Table 28). The evolution of the simulated and experimental Na^{+} and Ca^{2+} concentrations shows similar trends

as in Phase I. The simulated Na^+ concentrations agree with the experimental results quite well (Figure 20 right), but not as well for calcium (Figure 20 left).

For Phase III (beginning at 74.3 days, Figure 20), the concentration of $CaCl_2$ in the reservoir solution was again increased. The estimated effective porosity was 0.16, the tortuosity was 0.27, and the calculated D_e of Ca^{2+} was 3.41×10^{-11} m^2 s^{-1}. This D_e value is slightly lower than that obtained in Phase II (Table 28). The simulated Na^+ concentrations closely match the measured values, but simulated Ca^{2+} concentrations are again higher than the experimental data (Figure 20 left). The diffusion of Ca^{2+} into the reservoir is slower and the adsorbed Na-X near the center remained elevated (Figure 19 right).

During Phases I–III, the simulated concentrations for Ca^{2+} in the solution decreased consistently more slowly than for the experimental observations (Figure 20 left). The reason(s) for this behaviour may be related to the mass imbalance of the sorbed Ca^{2+} (4.14 meq) and desorbed Na^+ (2.90 meq) in the experimental data (Table 23 and Table 24 in section 7.2), a different exchange model than defined by equation 6-4, or different processes that result in the decrease of Ca^{2+} concentration, for example Ca^{2+} sequestration into a mineral precipitate.

7.4.2 Case B3.2

Similar to Case B3.1, the simulation of Case B3.2 was undertaken in three phases – corresponding to Phase I, II and III of the experiments. The diffusion and ion exchange processes are very similar to Case B3.1 because both experiments have the same experimental design, with the exception of the dry bulk densities (Table 22).

For Phase I, diffusion of Ca^{2+} takes place from the reservoir into the compacted Na-montmorillonite, and Ca/Na-X ion exchange occurs (Figure 21). Consequently, Ca^{2+} concentration in the reservoir decreases consistent with the observations (Figure 22). Simulated Na^+ concentrations in the reservoir show good agreement with the experimental results, but simulated Ca^{2+} concentrations overestimate the measured data (Figure 22). Estimated diffusion parameters are listed in Table 29. The effective porosity is 0.10, tortuosity is 0.30.

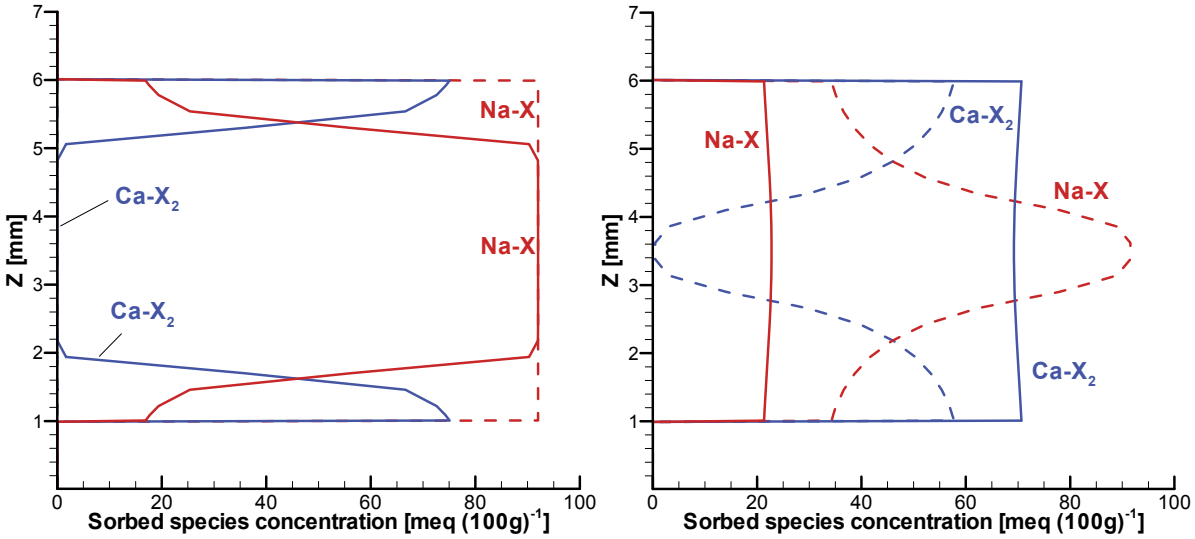

Figure 21: Simulated Concentrations of Sorbed Na-X (red lines) and Ca-X_2 (blue lines) at the Beginning (Dashed Lines) and the End (Solid Lines) of Phase I (left) and Phase III (Right) (Benchmark III Case 3.2)

For Phase II, simulated Na^+ concentration showed good agreement to the experimental results (Figure 22 right), but the simulated concentration of Ca^{2+} in the reservoir is higher than the experimental results (Figure 22 left). The estimated effective porosity is 0.15, and tortuosity is 0.37, which are higher than those calculated for the first phase. This change may be related to an actual, physical alteration of the bentonite induced by ion exchange processes (e.g. Na- to Ca/Na-montmorillonite) which was not considered in the MIN3P-THCm simulation.

For Phase III, after modification of the solution composition, elevated Ca^{2+} in the reservoir decreases rapidly, implying enhanced diffusion and ion exchange processes. Consequently, the concentration of Na^+ in the reservoir increases. By the end of the experiment, the sorbed Ca-X_2 and Na-X concentrations along the sample reached the highest and lowest values respectively, indicating that ion exchange equilibrium is almost reached (Figure 21). Simulated Na^+ concentrations in the reservoir agree well with the experimental observations (Figure 22 right), but the calculated Ca^{2+} concentrations are again substantially higher than the experimental results (Figure 22 left). This may be explained by the mass imbalance of the sorbed Ca^{2+} (5.92 meq) and desorbed Na^+ (3.68 meq) as discussed in section 7.2 (Table 23 and Table 24) or other potential reasons as described above. The corresponding estimated effective porosity of the sample is 0.18, with a tortuosity of 0.35. The effective diffusion coefficients derived for all species are listed in Table 29, which are slightly higher than those obtained for Phase II (Table 29).

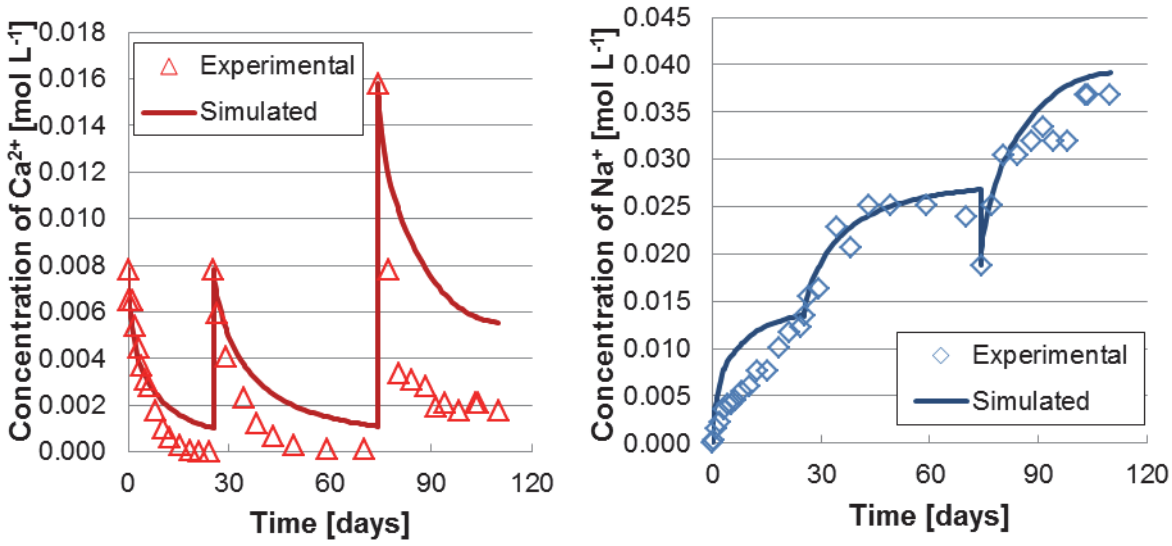

Figure 22: Comparison of Simulated and Experimental Concentrations for Ca^{2+} (Left) and Na^{+} (Right) in the Reservoir Solution for Benchmark III Experiment B3.2

Table 29: Estimated Diffusion Parameters in Na-Montmorillonite for Case B3.2

Phase	Effective porosity	Effective tortuosity	D_e [m^2 s^{-1}]		
			Ca^{2+}	Na^{+}	Cl^{-}
I	0.10	0.30	2.38×10^{-11}	4.01×10^{-11}	6.10×10^{-11}
II	0.15	0.37	4.46×10^{-11}	7.51×10^{-11}	1.14×10^{-10}
III	0.18	0.35	4.88×10^{-11}	8.23×10^{-11}	1.25×10^{-10}

7.4.3 Case B3.3

Based on the measured Ca^{2+} and Na^{+} concentration data, the simulation of this experiment can be divided into two phases (Figure 23). Phase I lasts up to 74 days and Phase II extends from 74 to 110 days. Correspondingly, the simulations were undertaken in two phases. Otherwise, diffusion and ion exchange processes remain identical to those described above in Cases B3.1 and B3.2.

During Phase I, there was initially no Ca-X_2 present in the Na-montmorillonite sample (Figure 24). When the Ca^{2+} rich solution was brought into contact with the sample, Ca^{2+} diffused into the sample, which triggered Ca^{2+}/Na-X ion exchange in the Na-montmorillonite, and diffusion of Na^{+} back into the reservoir solution. Simulated Na^{+} concentrations in the reservoir closely match the experimental data, while simulated Ca^{2+} concentrations in the reservoir differ substantially from the measured results. Estimated diffusion parameters are listed in Table 30.

For Phase II, simulated Na^{+} concentrations also show good agreement to the experimental results (Figure 23 right), while simulated Ca^{2+} concentrations exceed experimentally determined concentrations (Figure 23 left). By the end of the experiment, sorbed Ca-X_2 and Na-X species

concentrations adjacent to the reservoirs are different to those at the center of the sample, indicating ion exchange equilibrium has not been reached (Figure 24). Estimated diffusion parameters are listed in Table 30. In comparison to Phase I, both estimated effective porosity and effective tortuosity increase.

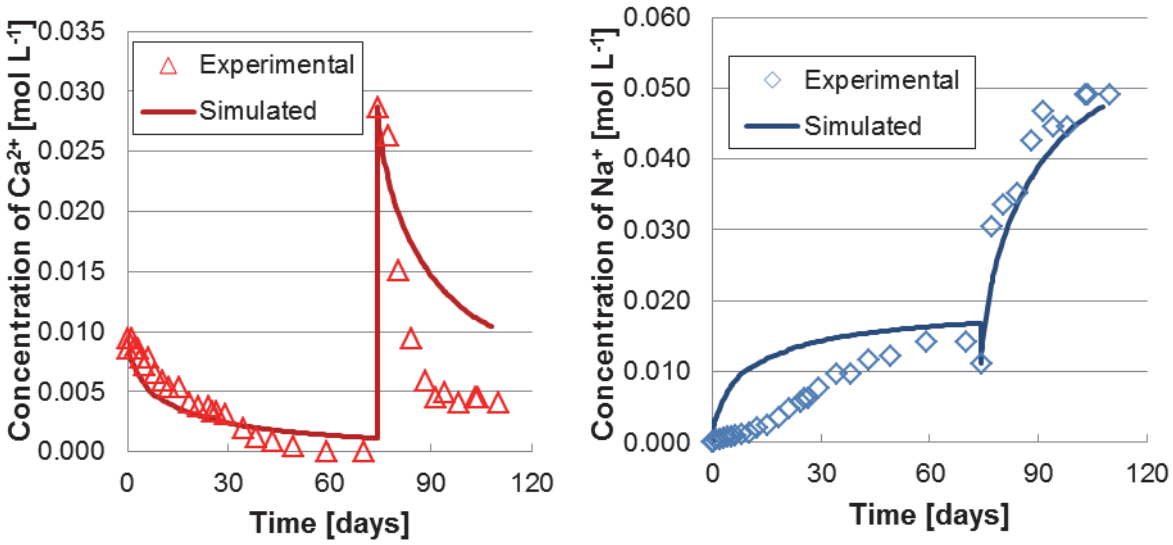

Figure 23: Comparison of Simulated and Experimental Concentrations for Ca^{2+} (Left) and Na^{+} (Right) in the Reservoir Solution for Experiment B3.3 (Benchmark III)

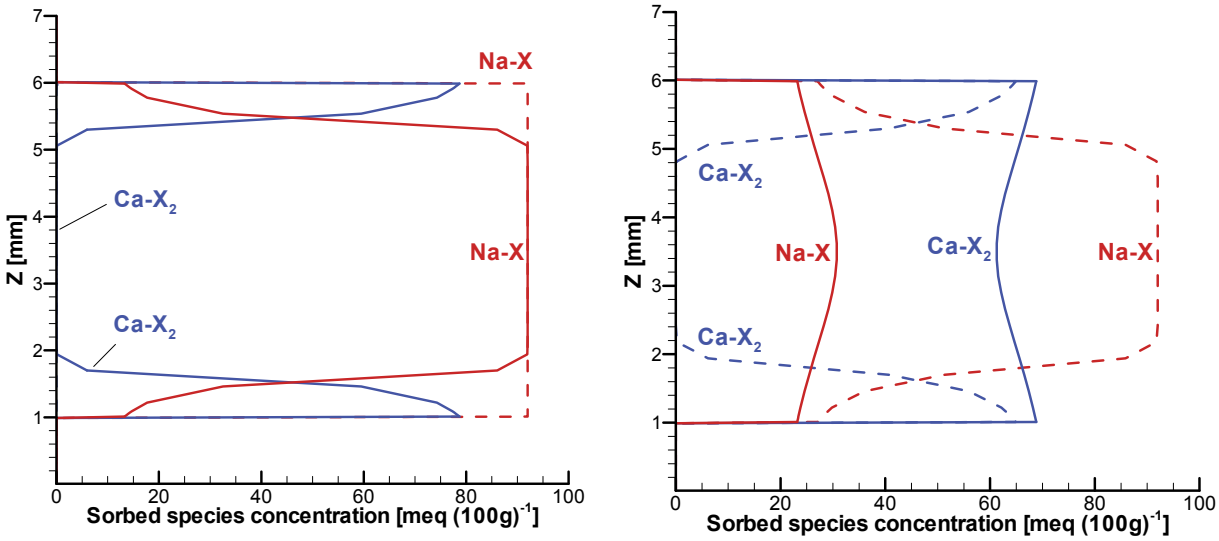

Figure 24: Simulated Concentrations of Sorbed Na-X (Red Lines) and Ca-X_2 (Blue Lines) at the Beginning (Dashed Lines) and the End (Solid Lines) of Phase I (Left) and Phase II (Right) (Benchmark III Case B3.3)

Table 30: Estimated Diffusion Parameters in Na-Montmorillonite for Case B3.3

Phase	Effective porosity	Effective tortuosity	D_e [m^2 s^{-1}]		
			Ca^{2+}	Na^+	Cl^-
I+II	0.06	0.21	9.83×10^{-12}	1.66×10^{-11}	2.52×10^{-11}
III	0.10	0.43	3.38×10^{-11}	5.69×10^{-11}	8.66×10^{-11}

7.5 SIMULATION RESULTS FOR EXPERIMENTS ON CA-MONTMORILLONITE

Simulations of the experiments on Ca-montmorillonite for Case B3.4 to Case B3.6 were undertaken in three phases corresponding to the sequential replacement of the solutions as shown in Table 22.

7.5.1 Case B3.4

Simulated results showed that during Phase I, there was initially no absorbed Na-X on the Ca-montmorillonite (Figure 25 left). When the Na^+ rich solution was brought into contact with the Ca-montmorillonite sample, Na^+ diffused into the sample, triggering $Na^+/Ca\text{-}X_2$ ion exchange, and diffusion of Ca^{2+} back into the reservoir solution. Simulated Na^+ concentrations in the reservoir decrease with time, reproducing the trend in the experimental data, but are slightly higher than the experimental data; while the simulated Ca^{2+} concentrations are substantially higher than the measured results. This may be related to the mass imbalance of the desorbed Ca^{2+} (8.36×10^{-4} mol L^{-1}) and sorbed Na^+ (4.01×10^{-3} mol L^{-1}) during Phase I (see Table 25 and Table 26 in section 7.2). Calibrated diffusion parameters are listed in Table 31. The best fit effective porosity is 0.24 and the best fit effective tortuosity is 0.35, which are much higher in comparison to the estimated diffusion parameters for the experiments in Na-montmorillonite. By the end of Phase I, the concentrations of sorbed Na-X and $Ca\text{-}X_2$ are almost uniformly distributed along the profile (Figure 25 left), indicating ion exchange equilibrium was nearly reached. Nevertheless, the fraction of Na-X remains small owing to the preference of Ca to adsorb onto montmorillonite.

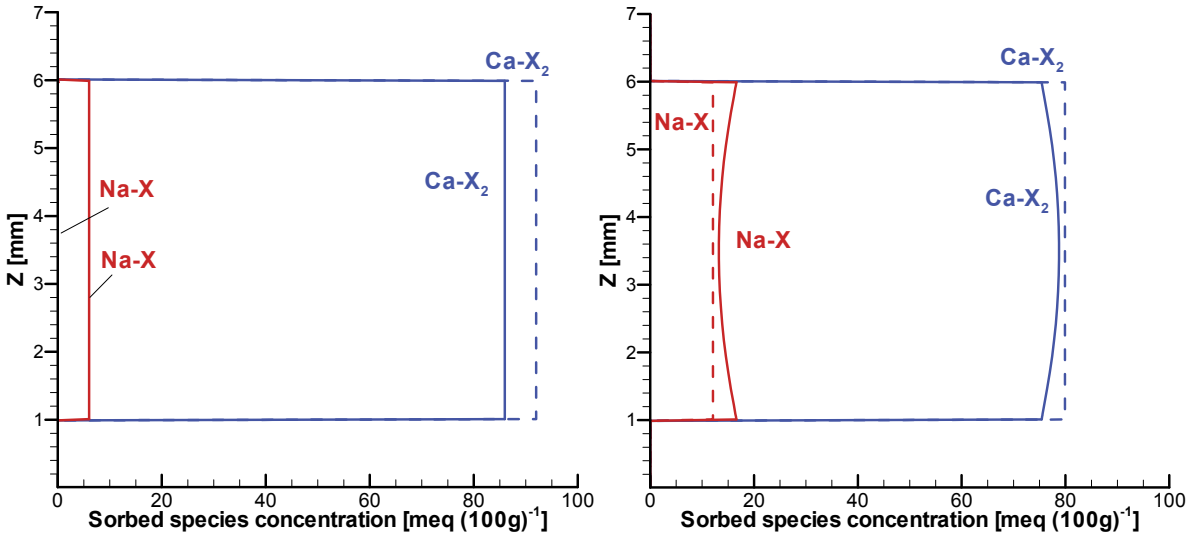

Figure 25: Simulated Concentrations of Sorbed Na-X (Red Lines) and Ca-X_2 (Blue Lines) at the Beginning (Dashed Lines) and the End (Solid Lines) of Phase I (Left) and Phase III (Right) (Benchmark III Case B3.4)

At the beginning of Phase II, the solution change results in a substantial increase of Na^+ concentrations in the reservoir (Figure 26 right). Na^+ diffuses into the sample, and Ca/Na ion exchange continues. Consequently, Ca^{2+} concentrations in the reservoir increase again. Simulated Na^+ concentrations slightly exceed observed concentrations, but still show good agreement to the experimental results. However, the simulated Ca^{2+} concentrations remain substantially higher than the experimental data. The corresponding diffusion parameters for Phase II are listed in Table 31, and are lower in comparison to those of Phase I.

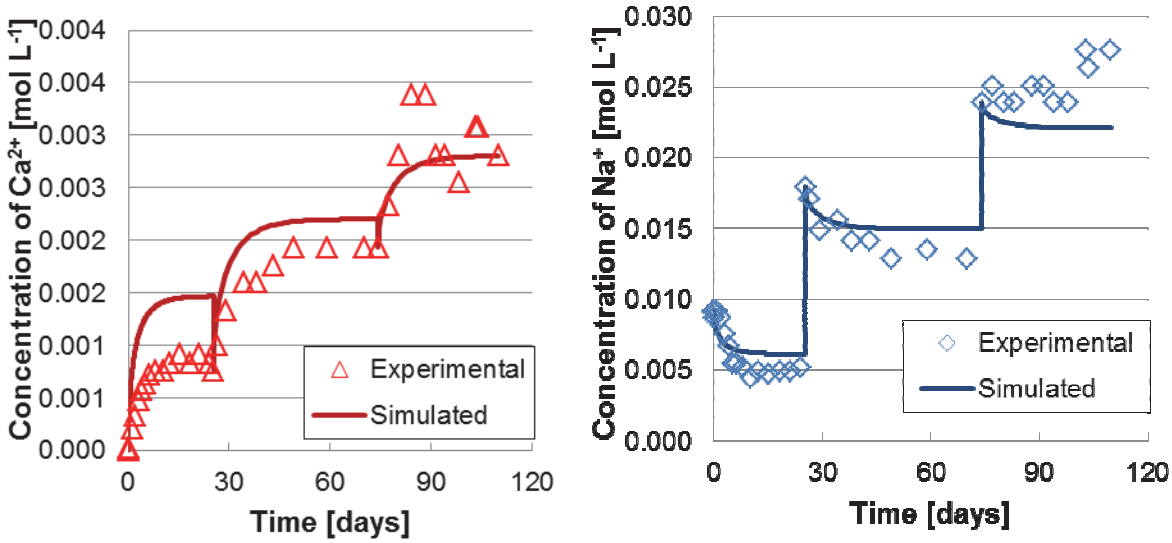

Figure 26: Comparison of Simulated and Experimental Concentrations for Ca^{2+} (Left) and Na^+ (Right) in the Reservoir Solution for Experiment B3.4 (Benchmark III)

An additional increase of Na^+ concentrations in the reservoir initiated Phase III of the experiment (Figure 26). The experimental results show an increase of Ca^{2+} concentrations in the reservoir with a more scattered distribution over time. Correspondingly, a decrease of Na^+ concentration in the reservoir would have been expected. However, the experimental Na^+ concentrations in the reservoir remain almost unchanged for the first 30 days, and then increase. These results are not intuitive and are inconsistent with an ion exchange mechanism. Nevertheless, a diffusion and ion exchange simulation was undertaken using the estimated diffusion parameters obtained from Phase II (Table 31). Simulated results show an increase of Ca^{2+} concentration in the reservoir, in-line with the experimental results; but a decrease of Na^+ concentrations is predicted, differing from the experimental results (Figure 26).

Table 31: Estimated Diffusion Parameters in Ca-Montmorillonite for Case B3.4 (Benchmark III)

Phase	Effective porosity	Effective tortuosity	D_e [m^2 s^{-1}]		
			Ca^{2+}	Na^+	Cl^-
I	0.24	0.35	6.69×10^{-11}	1.13×10^{-10}	1.72×10^{-10}
II	0.22	0.27	4.73×10^{-11}	7.96×10^{-11}	1.21×10^{-10}
III	0.22	0.27	4.73×10^{-11}	7.96×10^{-11}	1.21×10^{-10}

7.5.2 Case B3.5

The simulations of Case B3.5 were undertaken in a similar way as for Case B3.4. Initially, it was assumed that Ca-X_2 is the only ion-exchanged species on the Ca-montmorillonite sample (Figure 27 left). Phase I of the experiment began when the Na^+-rich solution was brought into contact with the test cell. Na^+ diffuses into the Ca-montmorillonite sample and results in Na/Ca-X_2 ion exchange reactions. The concentrations of Na^+ in the reservoir decrease, while Ca^{2+} concentrations increase (Figure 28). The simulated Na^+ concentration time curve shows good agreement with the experimental results, while the simulated Ca^{2+} concentrations are higher than the experimental results. By the end of Phase I, simulated adsorbed Na-X shows an almost even distribution with the concentration ranging from 5.2 to 6.2 meq $(100\ g)^{-1}$, which corresponds to the decreases of Ca-X_2 (Figure 27 left). The best fit diffusion parameters are listed in Table 32.

At the beginning of Phase II, the change in solution composition results in a substantial increase of Na^+ concentration in the reservoir. Simulated Na^+ concentrations in the reservoir decrease and show very good agreement to the experimental results (Figure 28). The simulated Ca^{2+} concentrations increase with time but are substantially higher than the experimental results.

Phase III began with another substantial increase of Na^+ concentrations in the reservoir (Figure 28). Similar to Case B3.4, the measured data shows a scattered distribution during this time interval. The Ca^{2+} concentrations in the reservoir show an increasing trend, while the Na^+ concentrations decrease at the beginning but then return to values similar to those at the beginning of Phase III. Simulated concentrations of both Na^+ and Ca^{2+} show reasonable agreement to the experimental results (Figure 28). The corresponding effective diffusion coefficients are one order of magnitude lower in comparison to those obtained for Phase II.

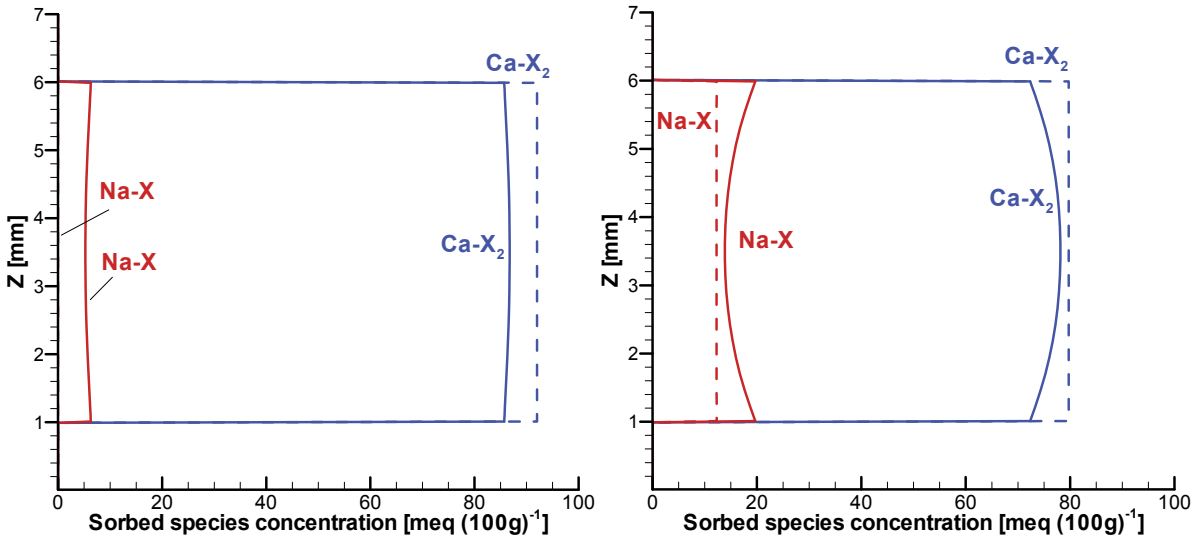

Figure 27: Simulated Concentrations of Sorbed Na-X (Red Lines) and Ca-X_2 (Blue Lines) at the Beginning (Dashed Lines) and the End (Solid Lines) of Phase I (left) and Phase III (Right) (Benchmark III Case B3.5)

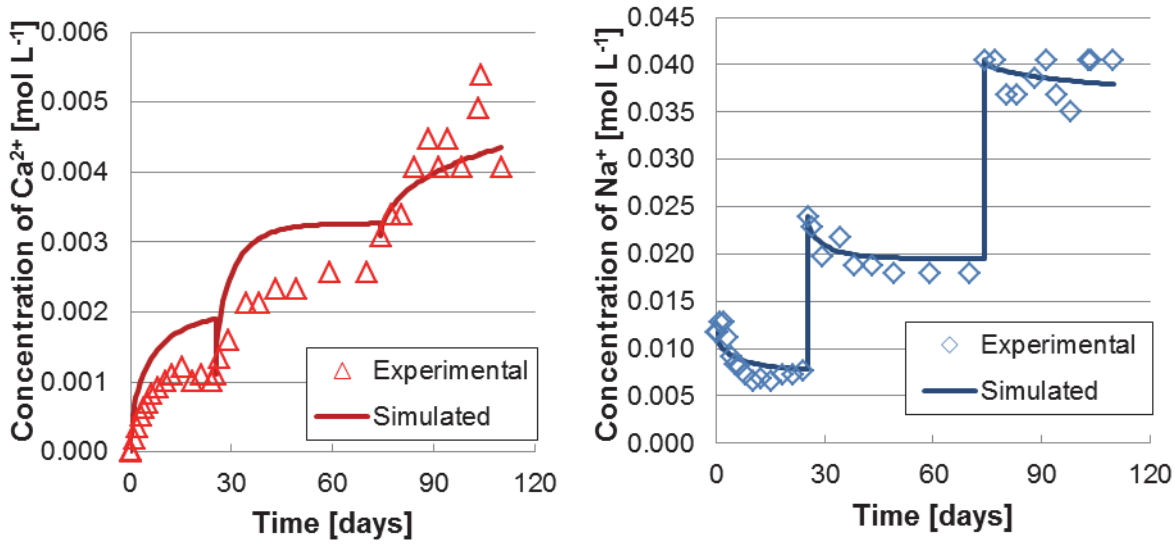

Figure 28: Comparison of Simulated and Experimental Concentrations for Ca^{2+} (Left) and Na^{+} (Right) in the Reservoir Solution for Benchmark III Experiment B3.5

Table 32: Estimated Diffusion Parameters in Ca-Montmorillonite for Case B3.5 (Benchmark III)

Phase	Effective porosity	Effective tortuosity	D_e [m^2 s^{-1}]		
			Ca^{2+}	Na^{+}	Cl^{-}
I	0.10	0.30	2.38×10^{-11}	4.00×10^{-11}	6.10×10^{-11}
II	0.16	0.33	4.09×10^{-11}	6.88×10^{-11}	1.05×10^{-10}
III	0.06	0.09	4.35×10^{-12}	7.33×10^{-12}	1.12×10^{-11}

7.5.3 Case B3.6

The simulations of Case B3.6 were undertaken in a similar way as for Cases B3.4 and B3.5. Initially, it was assumed that there was no Na-X on the Ca-montmorillonite sample (Figure 29 left). Phase I began when the Na^+ rich solution was introduced into the test cell. Subsequently, Na^+ diffuses into the Ca-montmorillonite sample and results in the Na/Ca-X_2 ion exchange reaction. The concentrations of Na^+ in the reservoir decrease, while Ca^{2+} concentrations increase (Figure 30). The simulated Na^+ concentration time curve shows good agreement with the experimental results, while the simulated Ca^{2+} concentrations are higher than the experimental results. By the end of Phase I, simulated adsorbed Na-X concentration shows an almost even distribution with concentrations ranging from 4.4 to 7.7 meq $(100\ g)^{-1}$, which corresponds to the decreases in Ca-X_2 equivalent fractions (Figure 29 left). The best fit diffusion parameters are listed in Table 33.

At the beginning of Phase II, the change in solution composition results in a substantial increase of Na^+ concentration in the reservoir. Subsequently simulated Na^+ concentrations in the reservoir decrease showing very good agreement to the experimental results (Figure 30 right). The simulated Ca^{2+} concentrations increase with time and substantially exceed the experimentally determined concentrations (Figure 30 left).

Phase III began with another substantial increase of Na^+ concentration in the reservoir (Figure 30 right). The Ca^{2+} concentrations in the reservoir show an increasing trend with some scatter, while the Na^+ concentrations decrease within the first 30 days of Phase III, but increase to concentrations exceeding those at the beginning of Phase III near the end of the experiment. Simulated concentrations of both Na^+ and Ca^{2+} show reasonable agreement to the experimental results (Figure 30). The corresponding effective diffusion coefficients are approximately 50% lower in comparison to those obtained in the second phase.

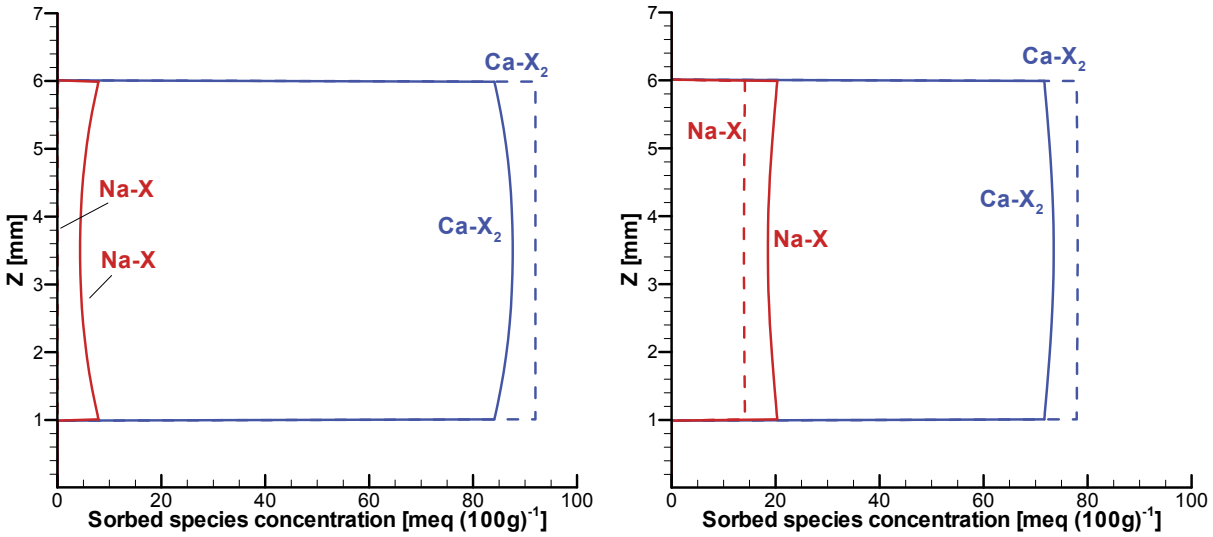

Figure 29: Simulated Concentrations of Sorbed Na-X (Red Lines) and Ca-X_2 (Blue Lines) at the Beginning (Dashed Lines) and the End (Solid Lines) of Phase I (Left) and Phase III (Right) (Benchmark III Case B3.6)

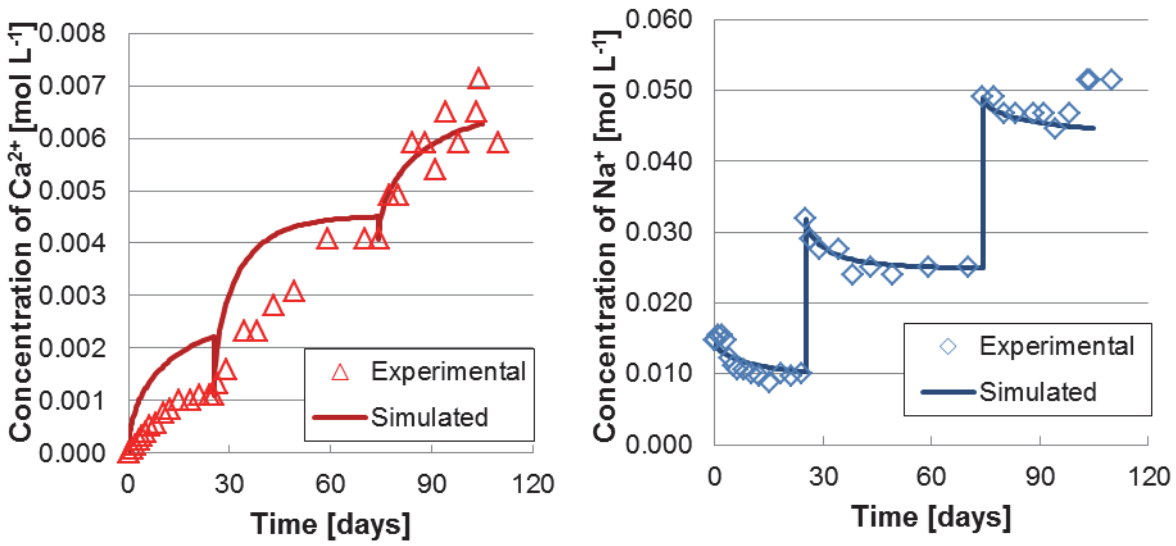

Figure 30: Comparison of Simulated and Experimental Concentrations for Ca^{2+} (Left) and Na^{+} (Right) in the Reservoir Solution for Benchmark III Experiment B3.6

Table 33: Estimated Diffusion Parameters in Ca-Montmorillonite for Benchmark III Case B3.6

Phase	Effective porosity	Effective tortuosity	D_e [m^2 s^{-1}]		
			Ca^{2+}	Na^{+}	Cl^{-}
I	0.16	0.10	1.24×10^{-11}	2.08×10^{-11}	3.17×10^{-11}
II	0.16	0.22	2.73×10^{-11}	4.60×10^{-11}	7.01×10^{-11}
III	0.06	0.30	1.41×10^{-11}	2.37×10^{-11}	3.61×10^{-11}

7.6 DISCUSSION

Based on the results of Benchmark III presented above, simulated and experimental results show overall good agreement with respect to the concentration trends. In most cases, the simulated Na^{+} concentration time curves in the reservoirs show very good agreement to the experimental results. However, good agreement of the simulated and experimental results of Ca^{2+} could not be fully achieved at the same time. The exact reason for this discrepancy remains unclear. One possible reason is the mass imbalance of the experimental results as discussed in section 7.2. Alternatively, a different ion exchange mechanism may be at work (such as the exchange of a complexed species such as $CaCl^{+}$ (Sposito et al. 1983) in lieu of Ca^{2+}). Alternatively, additional processes causing a Ca^{2+} sink (such as precipitation) that are currently not considered in the model may have affected the concentration evolution in the experiment.

Comparison of the simulated results to simulations from other teams is currently not possible. Birgersson presented simulations for Case B3.2 at EBS TF meetings in 2010 (Birgersson 2010) and 2011 (Birgersson 2011a), but only results of the first phase of Ca^{2+} evolution in the reservoir

were presented (results of Na^+ were not shown). The pore diffusion coefficient D_p was reported as $8.6x10^{-11}$ m^2 s^{-1}; with a porosity of 0.54, an effective diffusion coefficient $D_e = 4.64x10^{-11}$ m^2s^{-1} can be calculated. In addition, the simulations considered a filter of 2 mm thickness on both sides of the sample with D_p of $1.2x10^{-9}$ m^2 s^{-1} and a porosity of 0.3. Using these parameters, the rapid drop of Ca^{2+} in the reservoir can be well captured due to dilution in the filter. Based on this approach, a simulation of Case B3.1, Phase I was undertaken by including the filters (each of 2 mm in thickness) and using the same numerical methods (MIN3P-THCm and PEST). The main parameters of the filters were set to: porosity = 0.3, pore diffusion coefficient D_p of Ca^{2+} is $1.2x10^{-9}$ m^2 s^{-1}, tortuosity $=D_p/D_0=1.52$, following the parameters used by Birgersson. Simulated results are depicted in Figure 31. Notably, these results are very similar to the results obtained without filters (Figure 20). The simulated Na^+ concentration evolution showed good agreement to the experimental results, while the simulated Ca^{2+} results showed a less pronounced decrease than the experimental data. The calibrated effective porosity for the bentonite is now 0.33, and tortuosity is 0.048, resulting in slightly higher effective diffusion coefficients in comparison to the case without filters (compare to Table 28).

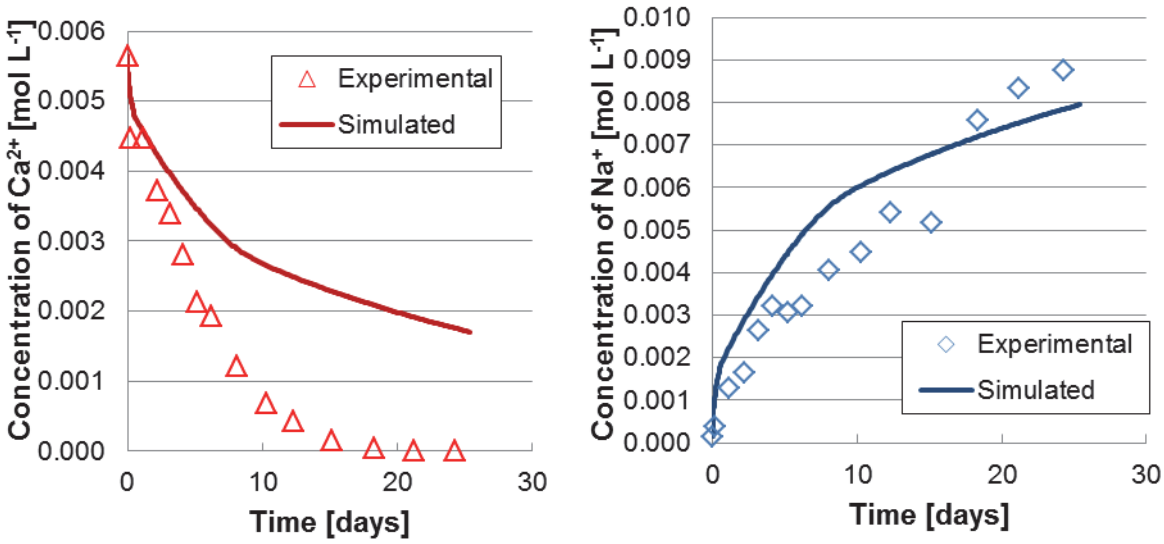

Figure 31: Comparison of Simulated and Experimental Concentrations for Ca^{2+} (Left) and Na^+ (Right) in the Reservoir Solution for Benchmark III Experiment B3.1 Phase I (Including Filters)

8. BENCHMARK IV: REACTIVE TRANSPORT IN BENTONITE

Compacted MX-80 bentonite, also known as Wyoming bentonite, is a potential buffer material to be used in radioactive waste repositories due to its favourable properties (e.g., low hydraulic conductivity, good swelling properties, plasticity, adsorption/retention of radionuclides, geochemical stability) and its abundance as a natural resource. Diffusion is the main transport mechanism in compacted and water-saturated bentonite. In a multicomponent system with charged species, electromigration may affect diffusive transport due to the electrostatic interaction of ions. Benchmark IV is based on an experiment designed to study the transport of aqueous species through compacted bentonite.

8.1 DESCRIPTION OF EXPERIMENT

A multicomponent transport experiment was performed on a compacted and saturated MX-80 bentonite sample of length 50 mm and diameter 50 mm using the core infiltration technique developed by Mäder (2002; 2004; 2005) and Mäder et al. (2004). The proposed benchmark problem is based on a flow-through experiment on a bentonite core carried out in the Rock-Water-Interaction Group at the University of Bern, Switzerland.

The flow-through experiment involved the injection of synthetic porewater similar in composition to the natural porewater of the field experiment in the host rock at Aspö. A tracer (deuterium) was added to monitor the breakthrough of the injected fluid and to assess the degree of mixing between the initial (natural) porewater and the injected fluid. The experimental period was 10 months, from March 2007 to January 2008, followed by analytical work.

8.2 MODEL SETUP AND MATERIAL PROPERTIES

The benchmark definition calls for the inclusion of electrostatic effects during transport. Sorption reactions combined with gypsum and calcite dissolution/precipitation reactions are included to explain cation concentrations in the effluent and on the exchanger as well as the distinct shape of the sulphate breakthrough curve.

Flow: The compacted bentonite column has a length of 0.05 m and was simulated in a one-dimensional mode (Figure 32). It was discretized into 25 cells. A unit cross-sectional area is assumed. The total duration of the experiment was 300 days. A constant influx of 2.3×10^{-9} $m^3\,m^{-2}\,s^{-1}$ was assigned to the left-hand boundary (Figure 32). The flow rate is fairly low such that diffusion remains the dominant transport mechanism. Material properties are assumed uniform throughout the column, and the total porosity is 0.4048 with an effective porosity for all species equal to 0.0714 (Alt-Epping et al. 2012; Fernandez et al. 2011).

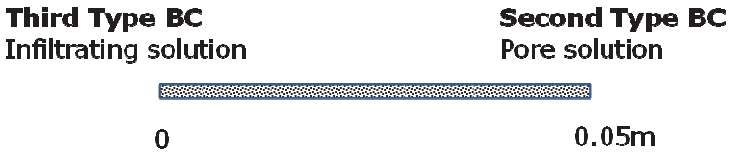

Figure 32: 1D Conceptual Model Setup for Multicomponent Reactive Transport Experiment in Bentonite

All benchmark problems included 2 scenarios, one using the same free phase diffusion coefficient in water of 1.87×10^{-9} $m^2\,s^{-1}$ for all species (Alt-Epping et al. 2014), and the other using species-dependent diffusion coefficients. For all species not explicitly assigned a diffusion coefficient (i.e. all secondary species), the same diffusion coefficient as for the tracer was used (Table 3). Dispersion was neglected.

The chemical reaction system includes primary and secondary species, gases and minerals as shown in Table 34. This resulted in a reactive transport problem with 21 primary unknowns (11 components, 1 gas, 5 minerals and 4 adsorbed species) (Table 34 and Table 37).

Table 34: Components (i.e., Primary Species), Secondary Species, Gases and Minerals Used in the Benchmark IV Simulations

Primary species	Primary species	Primary species
H^+	Na^+	SO_4^{2-}
Ca^{2+}	Cl^-	HCO_3^-
Mg^{2+}	$SiO_{2,aq}$	Tracer (deuterium)
K^+	Al^{3+}	

Secondary species		logK (25 °C)
OH^-	$\leftrightarrow H_2O - H^+$	13.9951
$Al(OH)_2^+$	$\leftrightarrow Al^{3+} + 2\ H_2O - 2\ H^+$	10.5945
AlO_2^-	$\leftrightarrow Al^{3+} + 2\ H_2O - 4\ H^+$	22.8833
$AlOH^{2+}$	$\leftrightarrow Al^{3+} + H_2O - H^+$	4.9571
$HAlO_{2(aq)}$	$\leftrightarrow Al^{3+} + 2\ H_2O - 3\ H^+$	16.4329
$CaCl^+$	$\leftrightarrow Ca^{2+} + Cl^-$	0.6956
$CaCl_{2(aq)}$	$\leftrightarrow Ca^{2+} + 2\ Cl^-$	0.6436
$CaSO_{4(aq)}$	$\leftrightarrow Ca^{2+} + SO_4^{2-}$	-2.1111
$CaCO_{3(aq)}$	$\leftrightarrow Ca^{2+} + HCO_3^- - H^+$	7.0017
$CaHCO_3^+$	$\leftrightarrow Ca^{2+} + HCO3^-$	-1.0467
$CaHSiO_3^+$	$\leftrightarrow Ca^{2+} + SiO_{2(aq)} + H_2O - H^+$	8.5760
$CaOH^+$	$\leftrightarrow Ca^{2+} + H_2O - H^+$	12.8330
CO_3^{2-}	$\leftrightarrow HCO_3^- - H^+$	10.3288
$CO_{2(aq)}$	$\leftrightarrow H^+ + HCO_3^- - H_2O$	-6.3447
$KCl_{(aq)}$	$\leftrightarrow K^+ + Cl^-$	1.4946
KSO_4^-	$\leftrightarrow K^+ + SO_4^{2-}$	-0.8796
$KOH_{(aq)}$	$\leftrightarrow H_2O + K^+ - H^+$	14.439
$MgCl^+$	$\leftrightarrow Mg^{2+} + Cl^-$	0.1349
$MgSO_{4(aq)}$	$\leftrightarrow Mg^{2+} + SO_4^{2-}$	-2.4117
$MgCO_{3(aq)}$	$\leftrightarrow Mg^{2+} + HCO_3^- - H^+$	7.3499
$MgHCO_3^+$	$\leftrightarrow Mg^{2+} + HCO_3^-$	-1.0357
$MgOH^+$	$\leftrightarrow Mg^{2+} + H_2O - H^+$	11.682
$NaCl_{(aq)}$	$\leftrightarrow Na^+ + Cl^-$	0.7770
$NaSO_4^-$	$\leftrightarrow Na^+ + SO_4^{2-}$	-0.7000
$NaHSiO_{3(aq)}$	$\leftrightarrow H_2O + Na^+ + SiO_{2(aq)} - H^+$	7.7550
$NaOH_{(aq)}$	$\leftrightarrow Na^+ + H_2O - H^+$	14.2050
$NaCO_3^-$	$\leftrightarrow Na^+ + HCO_3^- - H^+$	9.8144
$NaHCO_{3(aq)}$	$\leftrightarrow Na^+ + HCO_3^-$	-0.1541
$NaAlO_{2(aq)}$	$\leftrightarrow Al^{3+} + Na^+ + 2\ H_2O - 4\ H^+$	23.6266
$H_2SiO_4^{2-}$	$\leftrightarrow SiO_{2(aq)} + 2\ H_2O - 2\ H^+$	23.0000
$HSiO_3^-$	$\leftrightarrow H_2O + SiO_{2(aq)} - H^+$	9.9525
$HCl_{(aq)}$	$\leftrightarrow H^+ + Cl^-$	-0.6700

Gases		logK (25 °C)
$CO_{2(g)}$	$\leftrightarrow H^+ + HCO_3^- - H_2O$	-7.8136

Minerals		logK (25 °C)
Calcite	$CaCO_3 \leftrightarrow Ca^{2+} + HCO_3^- - H^+$	1.8487
Gypsum	$CaSO_4 \bullet 2H_2O \leftrightarrow Ca^{2+} + SO_4^{2-} + 2\ H_2O$	-4.4823
Quartz	$SiO_2 \leftrightarrow SiO_{2(aq)}$	-3.9993
K-feldspar	$KAlSi_3O_8 \leftrightarrow K^+ + Al^{3+} + 3\ SiO_{2(aq)} + 2\ H_2O - 4\ H^+$	-0.2753
MX-80	see below in the text	5.9941

The infiltrating solution composition shown in Table 35 (Fernández et al. 2011) was used to define the boundary condition for the inflow side of the column.

Table 35: Composition of the Infiltrating Fluid (Left-Hand Reactive Transport Boundary Condition) and the Initial Porewater Conditions (Fernández et al. 2011)

Species Name	Boundary Concentration (mol kg^{-1})	Initial Concentration (mol kg^{-1})	Constraint
pH	7.2	8.5	
Ca^{2+}	5.84×10^{-2}	3.5×10^{-2}	
Mg^{2+}	1.52×10^{-3}	2.5×10^{-2}	
K^{+}	2.5×10^{-4}	5.0×10^{-3}	
Na^{+}	9.2×10^{-2}	4.76×10^{-1}	Charge balance
Cl^{-}	2.08×10^{-1}	5.0×10^{-1}	
$SiO_{2,aq}$	1.0×10^{-5}	1.0×10^{-5}	
Al^{3+}	1.0×10^{-5}	1.0×10^{-5}	
SO_4^{2-}	2.02×10^{-3}	5.03×10^{-2}	Gypsum eq.
HCO_3^{-}	1.2×10^{-4}	7.70×10^{-5}	Calcite eq.
Tracer	2.0×10^{-1}	1.46×10^{-1}	

The initial porewater composition within the bentonite was constrained by the measured composition of the exchanger and by gypsum and calcite equilibrium (Table 35) (Fernández et al. 2011). The boundary condition on the outflow side of the column is a free exit boundary.

The bentonite is a mixture of minerals and their volume fractions are listed in Table 36. The dissolution-precipitation reactions were described as surface controlled kinetic reactions. A standard reversible rate expression is used and the reactive surface area is assumed constant which means that mineral reactivity remains constant during the course of a simulation. The kinetic parameters for the minerals are listed in Table 36.

Table 36: Mineralogy and Kinetic Parameters Based on Alt-Epping et al. (2014)

Mineral Name	Volume fraction[#]	logK [25 °C]	Log rate constant [mol m^{-2} s^{-1}]	Reactive surface area
Calcite	0.0036	1.8487	-6.19	100 (m^2 m^{-3} bulk)
Gypsum	0.0086	-4.4823	-3	100 (m^2 m^{-3} bulk)
Quartz	0.0521	-3.9993	-13.39	100 (m^2 m^{-3} bulk)
K-feldspar	0.0809	-0.2753	-13	100 (m^2 m^{-3} bulk)
MX-80	0.3786	5.9941	-13.58	788 (m^2 g^{-1} (mineral))

[#] bulk volume fraction, i.e. the volume of bulk aquifer occupied by a specific mineral phase divided by the bulk volume of the aquifer.

Bentonite is composed primarily of montmorillonite (MX-80), and its composition and dissociation reaction are as follows (Tournassat et al. 2003):

$$Na_{0.18}Ca_{0.1}(Al_{1.64}Mg_{0.36})(Si_{3.98}Al_{0.02})O_{10}(OH)_2 + 6.08\ H^+ \leftrightarrow 0.18\ Na^+ + 0.1\ Ca^{2+} + 1.66\ Al^{3+} + 0.36\ Mg^{2+} + 3.98\ SiO_{2(aq)} + 4.04\ H_2O \quad \log K = 5.9941 \quad \textbf{(8-1)}$$

Montmorillonite has a molar volume and weight of 134.88 $cm^3\ mol^{-1}$ and 368.44 $g\ mol^{-1}$ (Alt-Epping et al. 2012), respectively. Montmorillonite is not expected to dissolve in significant quantities and therefore it was assumed that the interactions with the porewater are limited to surface reactions. It constitutes the only exchanger in the system. The total exchange capacity of bentonite (CEC) was fixed at 73.66 meq 100 g^{-1} bulk. It is to note that this bentonite is a natural product. Its CEC value is much lower than that for the purified montmorillonite used in Benchmarks I to III. The bentonite has a dry bulk density of 1.4 kg L^{-1}, the specific surface area is 788 $m^2\ g^{-1}$ mineral (Alt-Epping et al. 2014; Fernandez et al. 2011).

Selectivity coefficients for the scenarios involving classic ion exchange (i.e. benchmark scenario 3) were taken from Bradbury and Baeyens (2003) (Table 37).

Table 37: Selectivity Coefficients for Ion Exchange Reactions (from Bradbury and Baeyens 2003)

Exchange reaction	K_s
Na-montmorillonite + $K^+ \leftrightarrow$ K-montmorillonite + Na^+	4.0
2 Na-montmorillonite + $Mg^{2+} \leftrightarrow$ Mg-montmorillonite + 2 Na^+	2.2
2 Na-montmorillonite + $Ca^{2+} \leftrightarrow$ Ca-montmorillonite + 2 Na^+	2.6

8.3 BENCHMARK SCENARIOS

The evolution of the effluent composition was simulated using CrunchFlow (Steefel et al. 2014) and MIN3P-THCm (this work). The problem complexity increased stepwise as defined in the following three scenarios:

Scenario 1: non-reactive transport involves transport of all components and complexes through the column without mineral reaction or ion exchange.

Scenario 2: this simulation involves the implementation of the entire reaction network as described in Table 34. However, surface reactions were not considered. A single porosity of 0.0714 was assumed.

Scenario 3: this simulation builds on the previous scenario 2 but also considers “conventional” ion exchange reactions. Selectivity coefficients are defined in Table 37.

For each of the above scenarios, two simulations were conducted using:

a) A single free-phase diffusion coefficient of $D = 1.87\times10^{-9}\ m^2\ s^{-1}$ for all species; and

b) Species-dependent free-phase diffusion coefficients as defined in Table 3. All species without assigned diffusion coefficients (i.e. those not listed in Table 3) were assigned the tracer diffusion coefficient of $D = 1.87\times10^{-9}\ m^2\ s^{-1}$.

8.4 SIMULATION RESULTS

Scenario 1: The results of the simulations and the experimental data for Scenario 1 are presented in Figure 33 (single diffusion coefficient) and Figure 34 (species-dependent diffusion coefficients). The agreement between MIN3P-THCm (hollow symbols) and CrunchFlow (lines) is excellent in both cases; however, there is a significant mismatch between the simulated results using both codes and the experimental data for Na^+. In addition, the early time simulation results for Ca^{2+}, SO_4^{2-} and Cl^- do not compare well to the experimental data. These differences may be due to neglecting reaction processes, such as mineral dissolution-precipitation and ion exchange, and/or additional transport processes.

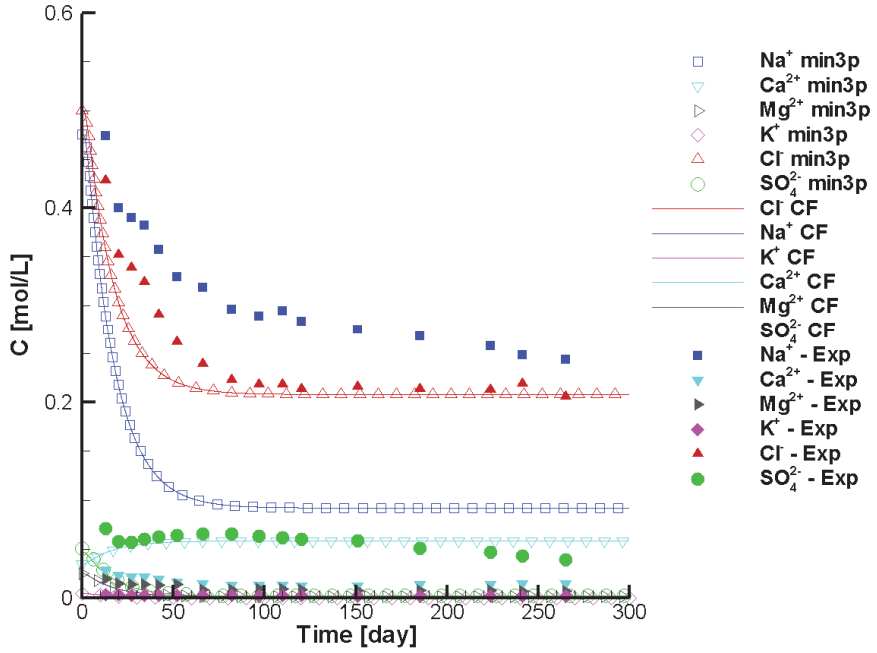

Figure 33: Scenario 1a: Time Series of the Simulated Effluent Composition and Measured Concentrations – Including Transport Only, Single Diffusion Coefficient (min3p Stands for MIN3P-THCm, CF Stands for CrunchFlow)

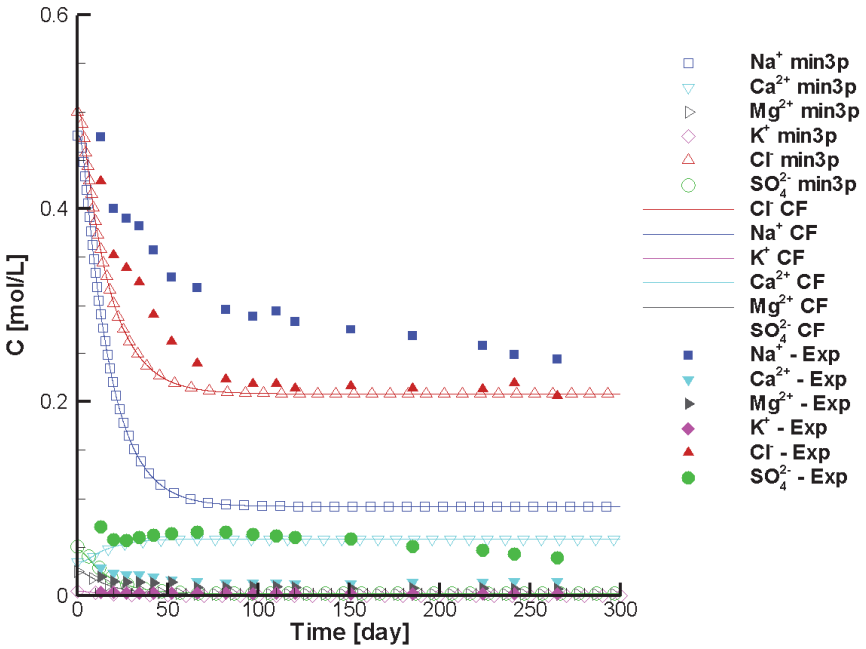

Figure 34: Scenario 1b: Time Series of the Simulated Effluent Concentrations and Measured Concentrations– Including Transport Only, Species-Dependent Diffusion Coefficients (min3p Stands for MIN3P-THCm, CF Stands for CrunchFlow)

Scenario 2: Results for the simulations and the experimental data are presented in Figure 35 and Figure 36 (species-dependent diffusion coefficients). Again, the agreement between MIN3P-THCm (hollow symbols) and CrunchFlow (lines) is excellent in both cases. The inclusion of mineral reactions does not significantly improve the agreement between the experimental and simulated results, suggesting that processes not accounted for in the model are affecting ion migration.

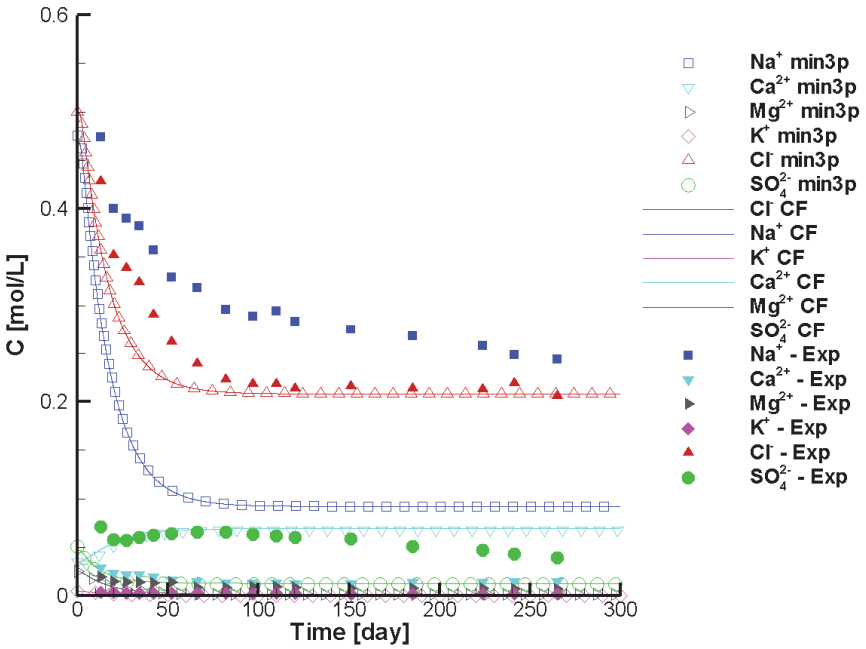

Figure 35: Scenario 2a: Time Series of the Simulated Effluent Composition and Measured Concentrations – Including Transport and Mineral Reactions, Single Diffusion Coefficient (min3p Stands for MIN3P-THCm, CF Stands for CrunchFlow)

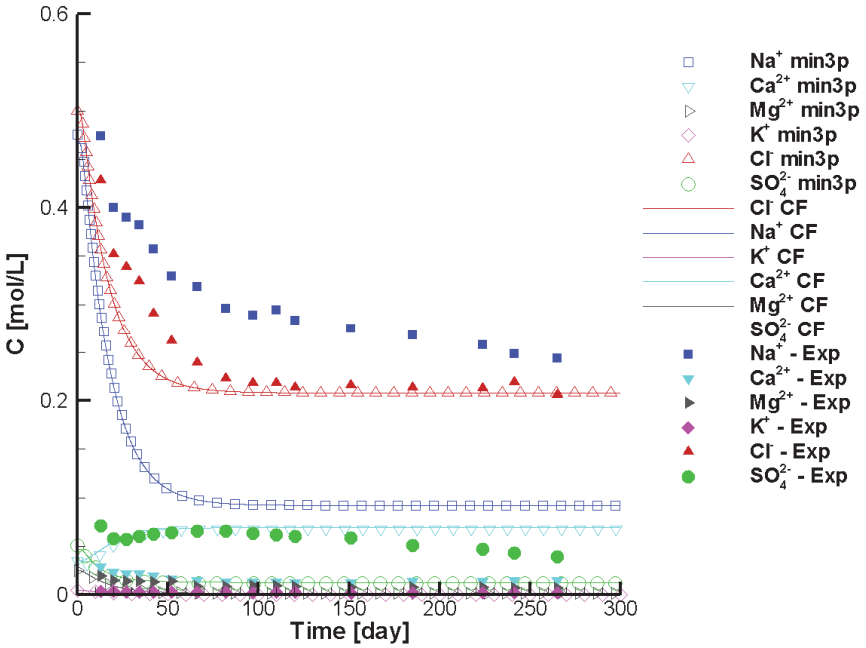

Figure 36: Scenario 2b: Time Series of the Simulated Effluent Composition and Measured Concentrations – Including Transport and Mineral Reactions, Species-Dependent Diffusion Coefficients (min3p Stands for MIN3P-THCm, CF Stands for CrunchFlow)

Scenario 3: The results of the Scenario 3 simulations and experimental data are presented in Figure 37 (single diffusion coefficient) and Figure 38 (species-dependent diffusion coefficients).

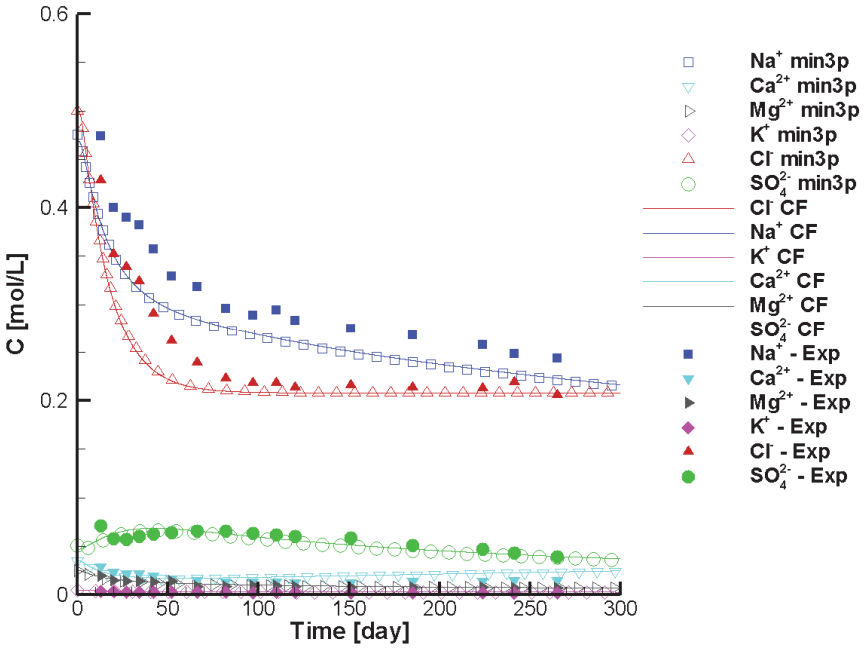

Figure 37: Scenario 3a: Time Series of the Simulated Effluent Composition and Measured Concentrations – Including Transport, Mineral Reactions and Ion Exchange, Single Diffusion Coefficient (min3p Stands for MIN3P-THCm, CF Stands for CrunchFlow)

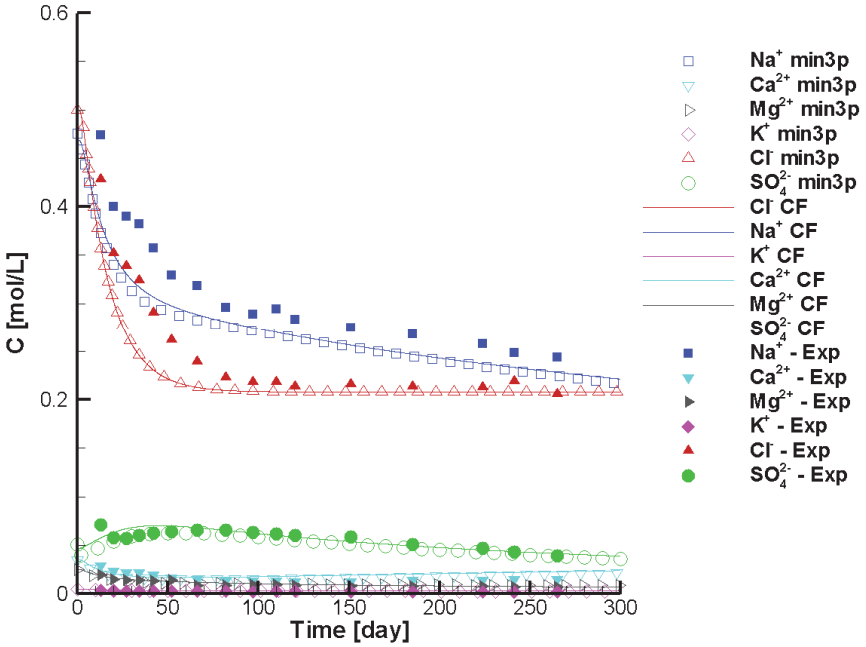

Figure 38: Scenario 3b: Time Series of the Simulated Effluent Composition and Measured Concentrations – Including Transport, Mineral Reactions and Ion Exchange, Species-Dependent Diffusion Coefficient (min3p Stands for MIN3P-THCm, CF Stands for CrunchFlow)

The agreement between MIN3P-THCm (hollow symbols) and CrunchFlow (lines) is very good for both cases. The inclusion of surface reactions also improves the agreement between the experimental and simulated concentration data. Gypsum dissolution increases SO_4^{2-} concentrations in the effluent and releases Ca^{2+}, which in turn is taken up by the exchanger. Therefore, Ca^{2+} and SO_4^{2-} concentrations agree quite well with the experimental data. Sorption reactions combined with gypsum and calcite dissolution/precipitation reactions reproduce the cations in the effluent as well as the distinct shape of the sulphate breakthrough curve. However, there are still differences between simulated and observed Na^+ concentration at early time. The concentrations of Na^+ and Mg^{2+} in the effluent are affected by the ion exchange reactions due to the substitution of Ca^{2+} for Na^+ and Mg^{2+} on the exchange sites.

In addition to comparing the simulation results amongst the codes and to the experimental data, the effect of including multispecies diffusion and electrochemical migration needs to be assessed. Differences in the effluent composition between the multi-species diffusion model (C_1) and the single-species diffusion model (C_2) can be expressed as percentages:

$$difference\,\% = \frac{\left|C_1 - C_2\right|}{0.5 \times \left(C_1 + C_2\right)} \times 100 \qquad \textbf{(8-2)}$$

In general, the differences decrease with time in scenario 1 and 2, whereas differences increase over time in scenario 3. Maximum differences in the case of Scenario 1 and 2 are about 8% for Mg^{2+}. In Scenario 3, maximum differences are less than 6% (Figure 39). This difference between MCD and conventional diffusion model is not very significant in comparison to the difference between the three scenarios.

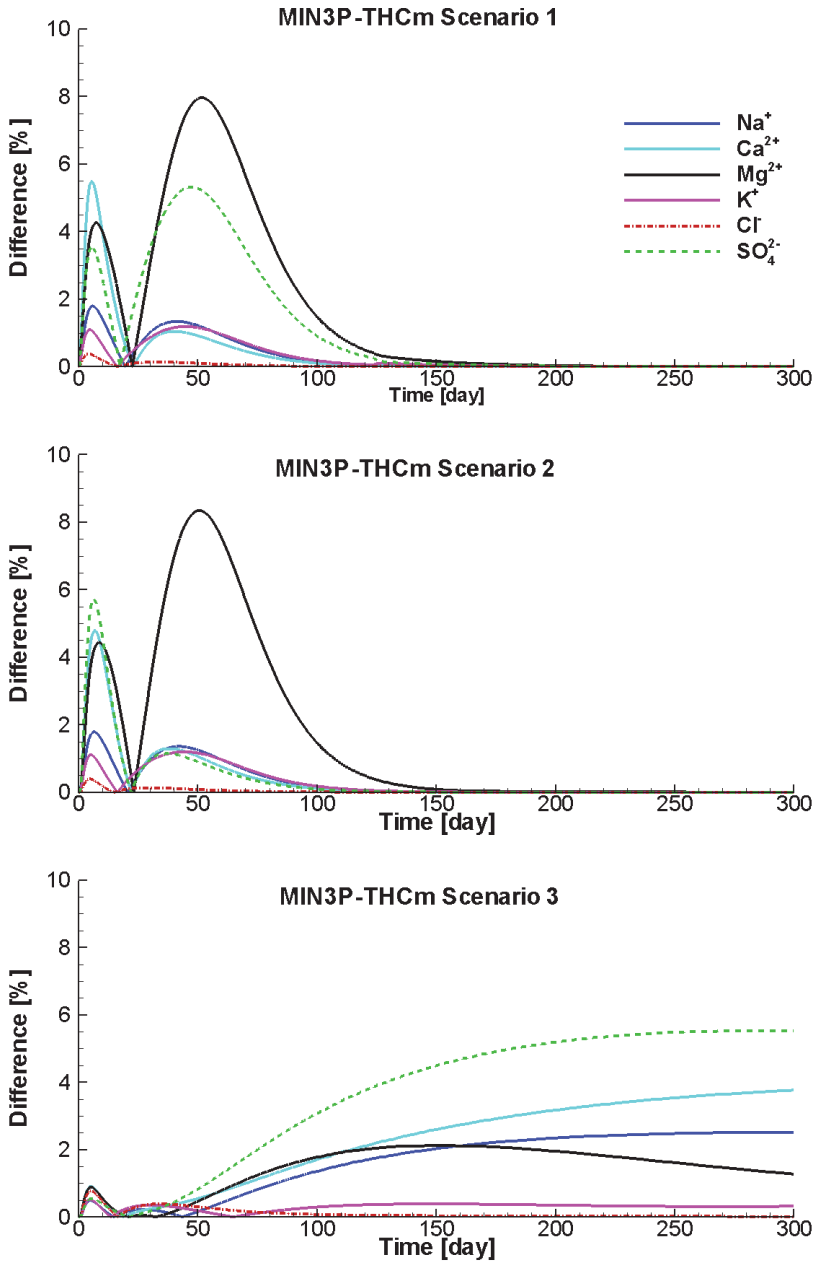

Figure 39: Effluent Composition Percent Differences between Simulation Option a (Single Diffusion Coefficient) and b (Species-dependent Diffusion Coefficients) for Scenarios 1, 2 and 3 Modelled by MIN3P-THCm

Examining the observed composition of the effluent and modelling results reveals that the multispecies diffusion model matches the experimental data slightly better, in particular for SO_4^{2-} and Na^+.

9. CONCLUSIONS AND OUTLOOK

A semi-empirical multicomponent diffusion (MCD) model has been implemented in MIN3P-THCm, which enables the code to simulate the diffusion of a mixture of ions through porous media by taking the species-dependent diffusion coefficients and electrostatic interactions in the solution into consideration. However, the current model does not include a full process-based description of mass transport in low permeability media and excludes ion migration in the diffusive double layer (e.g. Appelo and Wersin 2007; Appelo et al. 2010). The model accounts for this effect by inclusion of species-dependent empirical factors that modify effective diffusion coefficients for anions, cations and neutral species.

Combining the reactive transport code MIN3P-THCm and the parameter estimation software PEST provides a method for the estimation of effective porosity and effective tortuosity parameters from diffusion experiments. This method was applied in the analysis of the experiments of Benchmarks I to III. The results demonstrate that both parameters can be determined with a high level of confidence for a given set of experimental conditions if the experiments include a transient phase; however, if quasi-steady state diffusion conditions dominate throughout an experiment, it becomes more difficult to uniquely determine effective tortuosity and porosity separately, because these parameters are interdependent under these conditions. Nevertheless, the confidence in determining effective diffusion coefficients remains high for a given set of experimental conditions.

Numerical analyses of the through-diffusion experiments in compacted Na- and Ca-montmorillonite (Benchmark I) showed that with an increase of ionic strength of the solution, the diffusion parameters D_e, ϕ_e and τ_e generally increase as well. This may be explained by the thickness of the DDL (diffuse double layer), which is inversely proportional to the ionic strength of the solution (within the experimental range of 0.1 to 1.2 mol L^{-1} examined).

Benchmark II presented several diffusion-controlled experiments with increasing complexity by adding gypsum dissolution and ion exchange processes. Numerical analyses showed that the effective diffusion parameters obtained from simulating a through-diffusion experiment are very close to those obtained from a reactive diffusion experiment that included gypsum dissolution. A more in-depth analysis showed that small differences in thickness between the top and bottom bentonite layers explain the differences in ion concentrations in the top and bottom reservoirs.

Benchmark III is based on ion exchange experiments for highly compacted homo - ionic Na- and Ca-montmorillonite. Systematic numerical simulations of all six experiments were undertaken by considering diffusion and ion exchange reactions. The simulated results showed good agreement for the Na^+ concentration evolution in the reservoirs; but results tend to underestimate diffusion and ion exchange of Ca^{2+} when using the conventional ion exchange model of Na^+/Ca^{2+}. For this experiment, numerical analysis also suggests that increasing ionic strength can significantly affect effective diffusion coefficient (up to a factor of 5). Recalibration of the current model is required for each ionic strength condition, providing motivation for the implementation of a more process-based formulation.

The simulations of the most complex benchmarking experiment (Benchmark IV) also involved a code inter-comparison of MIN3P-THCm and CrunchFlow. Both codes produced almost identical results, providing confidence in their abilities. The simulations were executed for three scenarios with increasing geochemical complexity and showed better agreement with the experimental results for higher levels of complexity. Simulations including ion diffusion within the DDL and

Stern layer as defined in Alt-Epping et al. (2014) could not be included, because a suitable formulation is currently not available in MIN3P-THCm. Benchmark IV also illustrates that, for the conditions considered, differences between a standard diffusion model (based on Fick's law) and the multicomponent species-dependent diffusion approach are limited and dissipate over time. However, MIN3P-THCm does currently not include a formulation for surface diffusion (i.e. consideration of diffusion in the electric double layer and its dependence on ionic strength). With such a formulation, the agreement with experimental results could be further improved. The same formulation would also be useful for investigation of Benchmarks I-III.

A complete set of simulation results has been developed through this work, which can serve as a basis for discussion, comparison and further developments, in collaboration with other research teams. It would be beneficial to carry out additional code inter-comparisons for the other benchmarking tasks not only to verify the codes, but also to improve conceptual models to better capture experimental conditions.

ACKNOWLEDGEMENTS

This study was funded by NWMO, Canada. Valuable discussions with Tammy (Tianxiao) Yang (NWMO) and Monique Y. Hobbs (NWMO) helped to improve this report significantly.

REFERENCES

Alt-Epping, P., C. Tournassat, P. Rasouli, C.I. Steefel, K.U. Mayer, A. Jenni, U. Mäder, S. Sengor and R. Fernandez. 2014. Benchmark reactive transport simulations of a column experiment in compacted bentonite with multi-species diffusion and explicit treatment of electrostatic effects, *Computational Geosciences,* DOI:10.1007/s10596-014-9451-x

Appelo, C.A.J. and D. Postma. 2005. Geochemistry, Groundwater and Pollution,2nd ed. Amsterdam, the Netherlands.

Appelo, C.A.J. and P. Wersin. 2007. Multicomponent diffusion modeling in clay systems with application to the diffusion of tritium, iodide and sodium in Opalinus Clay. *Environmental Science & Technology,* **41**:5002-5007.

Appelo, C.A.J., L.R. Van Loon and P. Wersin. 2010. Multicomponent diffusion of a suite of tracers (HTO, Cl, Br, I, Na, Sr, Cs) in a single sample of Opalinus Clay. *Geochimica et Cosmochimica Acta*, **74**:1201-1219.

Bagotsky, V.S. 2006. Fundamentals of Electrochemistry (2nd Ed.). John Wiley and Sons, Pennington, New Jersey, 722 p.

Bard, A.J. and L.R. Faulkner. 1980. Electrochemical methods: fundamentals and applications. John Wiley and Sons, New York, xviii, 718 p.

Bea Jofré, S.A., K.U. Mayer and K.T.B. MacQuarrie. 2011. Modelling Reactive Transport in Sedimentary Rock Environments - Phase II MIN3P code enhancements and illustrative simulations for a glaciation scenario. Nuclear Waste Management Organization Technical report NWMO TR-2011-13, Toronto, Canada.

Bea, S.A., K.U. Mayer and K.T.B. MacQuarrie. 2012. Modeling of reactive transport in a hypothetical sedimentary basin affected by a glaciation/deglaciation event. 39th IAH Congress, Niagara Falls, Canada: September 16-21.

Benyaakov, S. 1981. Diffusion of seawater ions - significance and consequences of cross coupling effects, *American Journal of Science*, **281**:974-980.

Birgersson, M. 2009. Calculations of benchmarks 1-3, work in progress, EBS-Task Force Meeting Pori, 2-3 November 2009 (oral presentation).

Birgersson, M. and O. Karnland. 2009. Ion equilibrium between montmorillonite interlayer space and an external solution - Consequences for diffusional transport. *Geochimica et Cosmochimica Acta* **73**:1908–1923.

Birgersson, M. 2010. Benchmark calculations: continued work (benchmarks 3: Ca/Na exchange), EBS-Task Force Meeting Barcelona, 3-5 May 2010 (oral presentation).

Birgersson, M. 2011. EBS TFC: Experimental overview of benchmarks 1 – 4, Clay Technology AB, April 2011 (unpublished).

Birgersson, M. 2011a. Modelling of benchmarks 4 (and 3), EBS-Task Force Meeting, Toronto, Canada, November 22-24, 2011 (oral presentation).

Birgesson, M., L. Börgesson, M. Hedström, O. Karnland and U. Nilsson. 2009. Bentonite erosion – Final report. SKB Technical Report TR-09-34, SKB Stockholm.

Bradbury, M.H. and B. Baeyens. 2003. Porewater chemistry in compacted re-saturated MX-80 bentonite. *Journal of Contaminant Hydrology*, **61**(1-4):329-338.

de Soto, I., U. Maeder, R. Fernandez and A. Jenni. 2011. Benchmark 1 – Modelling with CrunchFlow, EBS Task Force meeting, Toronto, Canada, November 22-24, 2011, (oral presentation).

Doherty, J. 2010. PEST, Model-independent parameter estimation—User manual (5th ed.): Brisbane, Australia, Watermark Numerical Computing. (http://www.pesthomepage.org).

Fernández, R., U.K. Mäder and A. Jenni. 2011. Multi-component advectivediffusive transport experiment in MX-80 compacted bentonite: Method and results of 1st phase of experiment. Arbeitsbericht NAB 11-02, Hardstrasse 73, CH-5430 Wettingen.

Giambalvo, E.R., C.I. Steefel, A.T. Fisher, N.D. Rosenberg and C.G. Wheat. 2002. Effect of fluid-sediment reaction on hydrothermal fluxes of major elements, eastern flank of the Juan de Fuca Ridge. *Geochimica et Cosmochimica Acta*, **66** (10): 1739–1757.

Helfferich, F. 1962. Ion Exchange (2nd Ed.). McGraw-Hill, New York, 624 p.

Hirao, H., K. Yamada K. Koibuchi and N. Nito. 2012. Cement additive and cement composition, United States Patent: US 8,133,317 B2.

Holton, D. 2013. Modelling benchmark 1: Salt diffusion in Na and Ca montmorillonite, AMEC, EBS-Task Force meeting, London, UK (oral presentation).

Karnland, O., S. Olsson and U. Nilsson. 2006. Mineralogy and sealing properties of various bentonites and smectite-rich clay material. SKB Technical Report TR-06-30 (downloadable from www.skb.se)

Karnland, O., M. Birgersson and M. Hedström. 2011. Selectivity coefficient for Ca/Na ion exchange in highly compacted bentonite, *Physics and Chemistry of the Earth,* **36**:1554-1558.

Kozaki, T., J. Liu and S. Sato. 2008. Diffusion mechanism of sodium ions in compacted montmorillonite under different NaCl concentration, Physics and Chemistry of the Earth, 33:957–961

Lasaga, A.C. 1979. Treatment of multicomponent diffusion and ion-pairs in diagenetic fluxes, *American Journal of Science*, **279**:324-346.

Lasaga, A.C. 1998. Kinetic Theory in the Earth Sciences. Princeton Series in Geochemistry. 811 pp. Princeton, Chichester: Princeton University Press.

Lichtner, P.C. 1996. In: Lichtner, P.C., Steefel, C.I., Oelkers, E.H. (Eds.). Continuum formulation of multicomponent-multiphase reactive transport, Vol. 34. Mineralogical Society of America. Washington, DC, pp. 1–81 (Chapter 1).

Lide, D.R. 1994. CRC Handbook of chemistry and physics: a ready-reference book of chemical and physical data. 74th Edition, CRC Press/The chemical Rubber Co., Boca Raton, FL. U.S.A.

Mäder, U.K. 2002. GTS-HPF: Hyperalkaline fluid infiltration experiment through a drill core of a shear zone from the Grimsel Test Site. NAGRA Internal Report NIB 02-43. (Wettingen) 23 p.

Mäder, U.K. 2004. Porewater Chemistry (PC) Experiment: A new method of porewater extraction from Opalinus Clay with results for a sample from borehole BPC-A1. Mont Terri Technical Note TN 2002-25.

Mäder, U.K. 2005. Porewater chemistry, porosity and hydraulic conductivity of Callovo-Oxfordian claystone at the EST-322 deep drilling site sampled by the method of advective displacement (Laboratoire de Rechereche Souterrain de Meuse / Haute-Marne). Nagra Working Report NAB 05-04, Nagra, Wettingen, Switzerland.

Mäder, U.K., H.N. Waber and A. Gautschi. 2004. New method for porewater extraction from claystone and determination of transport properties with results for Opalinus Clay (Switzerland). In: R.B. Wanty & R.R. Seal II (eds) Proceedings of the 11th International Symposium on Water-Rock Interaction, WRI-11, 2004, Saratoga Springs (N.Y.) Balkema, 445-448.

Mayer, K.U. 1999. A numerical model for multicomponent reactive transport in variably-saturated porous media, PH.D. – thesis, Department of Earthe Sciences, University of Waterloo, Waterloo, Ontario, Canada.

Mayer, K.U., E.O. Frind and D.W. Blowes. 2002. Multicomponent reactive transport modeling in variably saturated porous media using a generalized formulation for kinetically controlled reactions. *Water Resources Research*, **38**:1174-1195. doi:10:1029/2001WR000862

Mayer, K.U. and K.T.B. MacQuarrie 2010. Solution of the MoMaS reactive transport benchmark with MIN3P - Model formulation and simulation results, *Computers & Geosciences.,* **14**:405-419, doi:10.1007/s10596-009-9158-6

McDuff, E. R. and A.R. Ellis. 1979. Determining diffusion-coefficients in marine-sediments - laboratory study of the validity of resistivity techniques. *American Journal of Science*, **279**:666-675.

Newman, J.S. 1973. Electrochemical Systems. Prentice-Hall, Englewood Cliff, New Jersey, 423 p.

Spiessl, S.M., K.T.B. MacQuarrie and K.U. Mayer 2008. Identification of key parameters controlling dissolved oxygen migration and attenuation in fractured crystalline rocks, *Journal of Contaminant Hydrology,* **95**:141–153.

Sposito, G., C. Jouany, K.M. Holtzclaw and C.S. LeVesque. 1983. Calcium-Magnesium exchange on Wyoming bentonite in the presence of adsorbed sodium. *Soil Science Society of America Journal,* **47**:1081–1085.

Steefel, C.I., C.A.J. Appelo, B. Arora, D. Jacques, T. Kalbacher, O. Kolditz, V. Lagneau, P.C. Lichtner, K.U. Mayer, J.C.L. Meeussen, S. Molins, D. Moulton, H. Shao, J. Šimůnek, N. Spycher, S.B. Yabusaki and G.T. Yeh. 2014. Reactive transport codes for subsurface environmental simulation, *Computational Geosciences*, DOI: 10.1007/s10596-014-9443-x.

Taylor, R. and R. Krishna. 1993. Multicomponent mass transfer. John Wiley and Sons, New York, 578 p.

Tournassat, C., A. Neaman, F. Villieras, D. Bosbach and L. Charlet. 2003. Nanomorphology of montmorillonite particles: Estimation of the clay edge sorption site density by low-pressure gas adsorption and AFM observations. *American Mineralogist*, **88**(11-12), 1989-1995.

Van Cappellen, P. and J.F. Gaillard. 1996. Biogeochemical dynamics in aquatic sediments. In *Reactive Transport In Porous Media: General Principles and Application to Geochemical Processes* (eds. P.C. Lichtner, C.I. Steefel and E.H. Oelkers). *Reviews in Mineralogy* **34**, 335-376, Mineralogical Society of America.

Wersin, P.E, E. Curti and C.A.J. Appelo. 2004. Modelling bentonite–water interactions at high solid/liquid ratios: swelling and diffuse double layer effects, *Applied Clay Science*, **26**(1–4), 249–257.

Xie, M., S.S. Agus, T. Schanz and O. Kolditz. 2004. An upscaling method and a numerical analysis of swelling/shrinking processes in a compacted bentonites and mixture *International Journal for Numerical and Analytical Methods in Geomechanics*, **28**(15):1479-1502.

Yeung, A.T. 1992. Diffuse double-layer equations in SI units, *Journal of Geotechnical Engineering*, **118**(12):2000-2005.